REPORT DOCUMENTATION PAGE

Form Approved OMB NO. 0704-0188

The public reporting burden for this collection of information is estimated to average 1 hour per response, including the time for reviewing instructions, searching existing data sources, gathering and maintaining the data needed, and completing and reviewing the collection of information. Send comments regarding this burden estimate or any other aspect of this collection of information, including suggesstions for reducing this burden, to Washington Headquarters Services, Directorate for Information Operations and Reports, 1215 Jefferson Davis Highway, Suite 1204, Arlington VA, 22202-4302. Respondents should be aware that notwithstanding any other provision of law, no person shall be subject to any oenalty for failing to comply with a collection of information if it does not display a currently valid OMB control number.
PLEASE DO NOT RETURN YOUR FORM TO THE ABOVE ADDRESS.

1. REPORT DATE (DD-MM-YYYY)	2. REPORT TYPE	3. DATES COVERED (From - To)
09-10-2013	Ph.D. Dissertation	-

4. TITLE AND SUBTITLE	5a. CONTRACT NUMBER
Polarity Control and Doping in Aluminum Gallium Nitride	
	5b. GRANT NUMBER
	W911NF-04-D-0003
	5c. PROGRAM ELEMENT NUMBER
	611102

6. AUTHORS	5d. PROJECT NUMBER
Marc Hoffmann	
	5e. TASK NUMBER
	5f. WORK UNIT NUMBER

7. PERFORMING ORGANIZATION NAMES AND ADDRESSES	8. PERFORMING ORGANIZATION REPORT NUMBER
North Carolina State University Research Administration 2701 Sullivan Drive, Suite 240 Raleigh, NC 27695 -7514	

9. SPONSORING/MONITORING AGENCY NAME(S) AND ADDRESS(ES)	10. SPONSOR/MONITOR'S ACRONYM(S)
U.S. Army Research Office P.O. Box 12211 Research Triangle Park, NC 27709-2211	ARO
	11. SPONSOR/MONITOR'S REPORT NUMBER(S)
	57365-EL-SR.4

12. DISTRIBUTION AVAILIBILITY STATEMENT

Approved for public release; distribution is unlimited.

13. SUPPLEMENTARY NOTES

The views, opinions and/or findings contained in this report are those of the author(s) and should not contrued as an official Department of the Army position, policy or decision, unless so designated by other documentation.

14. ABSTRACT

AlGaN can be used for the fabrication of lateral polar structures (LPS) by a periodic inversion of the c-axis as achieved by a polarity control scheme during its growth by metal organic chemical vapor deposition (MOCVD). These structures can be used for second harmonic generation in the ultraviolet spectral region, as well as for lateral p/n-junctions. The two major challenges addressed in this work exist in the general implementation of the AlGaN technology and in the fabrication of AlGaN LPS, and both prevent the realization of AlGaN UV-emitters. These

15. SUBJECT TERMS

AlGaN, lateral polar structures, metal organic chemical vapor deposition

16. SECURITY CLASSIFICATION OF:			17. LIMITATION OF ABSTRACT	15. NUMBER OF PAGES	19a. NAME OF RESPONSIBLE PERSON
a. REPORT	b. ABSTRACT	c. THIS PAGE			Michael Gerhold
UU	UU	UU	UU		19b. TELEPHONE NUMBER
					919-549-4357

Standard Form 298 (Rev 8/98)
Prescribed by ANSI Std. Z39.18

Report Title

Polarity Control and Doping in Aluminum Gallium Nitride

ABSTRACT

AlGaN can be used for the fabrication of lateral polar structures (LPS) by a periodic inversion of the c-axis as achieved by a polarity control scheme during its growth by metal organic chemical vapor deposition (MOCVD). These structures can be used for second harmonic generation in the ultraviolet spectral region, as well as for lateral p/n-junctions. The two major challenges addressed in this work exist in the general implementation of the AlGaN technology and in the fabrication of AlGaN LPS, and both prevent the realization of AlGaN UV-emitters. These challenges are: (1) the presence of a high concentrations of native defects and extrinsic impurities in AlGaN that can reduce the efficiency of optoelectronic devices, especially in the case of high doping with Mg or Si, and (2) as typically observed, a growth rate difference that exists during the simultaneous growth of III- and N-polar domains adjacent to each other in a LPS.

In this dissertation, solutions to these two challenges are based on two novel and original approaches involving (1) Fermi-level point defect control schemes, and (2) mass transport control between polar domains. In approach (1), the control of point defects and reduction of compensations, VN, H or O are identified as the cause of high resistivity and low mobility in AlGaN due to their low formation energies at high Mg or Si doping concentrations. To confirm and quantify the Fermi-level point defect control scheme, above bandgap illumination during the growth of GaN was demonstrated to control the incorporation of these defects. Significant reductions in the point defect were achieved as evidenced by changes in their corresponding luminescence, for example, the blue luminescence at 2.8 eV (VN-related). Additionally, reduced resistivity and atomic concentrations, such as an order of magnitude lower H concentration, were observed. These studies confirm that the point defect management scheme developed in this work can control compensation in n-type as well as in p-type semiconductors.

Polarity Control and Doping in Aluminum Gallium Nitride

Kontrolle der Polarität und Dotierung in Aluminium Gallium Nitrid

vorgelegt von
Diplom-Physiker
Marc Patrick Hoffmann
aus Berlin

von der Fakultät II – Mathematik und Naturwissenschaften
der Technische Universität Berlin
zur Erlangung des akademischen Grades

Doktor der Naturwissenschaften
– Dr. rer. nat. –

genehmigte Dissertation

Promotionsausschuss:

Vorsitzender: Prof. Dr. Michael Lehmann
Gutachter: Prof. Dr. Michael Kneissl
Gutachter: Prof. Dr. Zlatko Sitar

Tag der wissenschaftlichen Aussprache:

10. Juni 2013

Berlin 2013

D83

Abstract

AlGaN can be used for the fabrication of lateral polar structures (LPS) by a periodic inversion of the c-axis as achieved by a polarity control scheme during its growth by metal organic chemical vapor deposition (MOCVD). These structures can be used for second harmonic generation in the ultraviolet spectral region, as well as for lateral p/n-junctions. The two major challenges addressed in this work exist in the general implementation of the AlGaN technology and in the fabrication of AlGaN LPS, and both prevent the realization of AlGaN UV-emitters. These challenges are: (1) the presence of a high concentrations of native defects and extrinsic impurities in AlGaN that can reduce the efficiency of optoelectronic devices, especially in the case of high doping with Mg or Si, and (2) as typically observed, a growth rate difference that exists during the simultaneous growth of III- and N-polar domains adjacent to each other in a LPS.

In this dissertation, solutions to these two challenges are based on two novel and original approaches involving (1) Fermi-level point defect control schemes, and (2) mass transport control between polar domains. In approach (1), the control of point defects and reduction of compensations, V_N, H or O are identified as the cause of high resistivity and low mobility in AlGaN due to their low formation energies at high Mg or Si doping concentrations. To confirm and quantify the Fermi-level point defect control scheme, above bandgap illumination during the growth of GaN was demonstrated to control the incorporation of these defects. Significant reductions in the point defect were achieved as evidenced by changes in their corresponding luminescence, for example, the blue luminescence at 2.8 eV (V_N-related). Additionally, reduced resistivity and atomic concentrations, such as an order of magnitude lower H concentration, were observed. These studies confirm that the point defect management scheme developed in this work can control compensation in n-type as well as in p-type semiconductors.

In approach (2), mass transport control between polar domains, the surface mass transport between differently oriented domains was determined to be a function of the Ga supersaturation. Using Ga supersaturation as a control, a condition where identical growth rates for both polarities was obtained and high quality AlGaN LPS with domains in the micrometer scale could be fabricated. Furthermore, the first AlN LPS was grown and studied. Finally, the utility of these two new approaches was demonstrated by fabricating an AlGaN lateral p/n-junction that exhibited a marked decrease in compensation effects within each particular domain.

Both point defect control via above bandgap illumination, as well as the control of the growth rate difference of LPS, will have considerable impact on the field of III-V-nitrides as these novel approaches will potentially facilitate a new class of devices in the future.

Zusammenfassung

AlGaN basierte Laterale Polare Strukturen (LPS) können mit Hilfe der metallorganischen Gasphasenepitaxie gewachsen werden, indem man die c-Achse periodisch invertiert. Derartige Strukturen haben das Potential, um für Frequenzverdopplung von kohärentem Licht in das ultraviolette (UV) Spektralgebiet verwendet zu werden. Weitere Anwendungen liegen im Bereich lateraler p/n-Übergänge. Bezüglich ihrer Herstellung gibt es derzeit noch zwei wesentliche Herausforderungen, die gelöst werden müssen, um das volle Potential des Materialsystems für optoelektronische Bauelemente im UV ausnutzen zu können: (1) In AlGaN kann eine hohe Konzentration von intrinsischen und extrinsischen Störstellen zu einer reduzierten Quanteneffizienz von optischen Bauelementen führen. Dies ist besonders bei höheren Dotierungen der Fall, da es dort zur Selbstkompensation des Dotanden kommen kann. (2) Werden III- und N-polare Domänen nebeneinanderliegend in einer LPS gewachsen, so wird in der Regel ein Schichtdickenunterschied zwischen den Domänen beobachtet.

In der vorliegenden Arbeit wurden beide genannten Herausforderungen detailliert bearbeitet und gelöst. Im Fall von mit Si oder Mg dotiertem AlGaN führen hohe Störstellen-konzentrationen wie Stickstoffvakanzen, H oder O zu hohen Widerständen und einer niedrigen Beweglichkeit der freien Ladungsträger. Diese hohen Konzentrationen werden dadurch erklärt, dass im Bereich hoher Dotierungen die Formierungsenergien dieser Störstellen verringert werden, was zu einem erhöhten Einbau von Kompensatoren führt. Bestrahlt man AlGaN Filme während des Wachstums mit UV-Licht (entsprechend einer Anregungsenergie größer als die Bandlücke), führt dies zu einem verringertem Einbau von Störstellen. So kann z.B. in GaN:Mg eine stark reduzierte blaue Lumineszenz (2.8 eV) gemessen werden, was auf einen verringerten Einbau von Stickstoffvakanzen schließen lässt und zu einem geringerem elektrischen Widerstand führt. Des Weiteren wird im Rahmen dieser Arbeit gezeigt, dass das hier vorgestellte Modell zur Kontrolle des Einbaus von Defekten sowohl für n- als auch p-leitende Halbleiter verwendet werden kann.

Die zweite Herausforderung des Schichtdickenunterschiedes der N- und III-polaren Domänen in LPS (2) wird in dieser Arbeit durch einen Oberflächenmassentransport zwischen den polaren GaN Domänen erklärt. Abhängig von der Wachstumsbedingung führt dieser Massentransport zu einem bevorzugten Wachstum jeweils einer polaren Domäne. Folglich konnten aber auch Bedingungen gefunden werden, in denen die Wachstumsrate der Domänen identisch ist und hoch qualitative AlGaN LPS mit Mikrometer großen Domänen gewachsen werden. Abschließend wurden die Erkenntnisse aus (1) und (2) kombiniert und verbesserte elektrische und optische Eigenschaften lateraler p/n Übergänge nachgewiesen, wenn diese mit UV-Licht während des Wachstums bestrahlt wurden.

Beides, sowohl die Störstellenkontrolle mittels UV-Bestrahlung als auch die Kontrolle der N- und III-polaren Domänen in LPS, wurde nie zuvor demonstriert und eröffnen einzigartige neue Möglichkeiten.

Contents

1.   Introduction

Over the past 15 years, III-nitrides have filled an important void in optoelectronic and high-frequency electronics, becoming the essential material for high efficiency illumination and energy management applications. The major breakthrough for the nitrides came in 1989 by Amano *et al.* with the first report of p-type conductivity in GaN by using magnesium (Mg) as a dopant.[1] Still today, Mg is the only known dopant that can achieve efficient p-type conductivity in III-nitrides. A few years later, the first GaN-based blue light emitting diode was demonstrated by Nakamura *et al.*[2] Since the middle of the nineties until today a significant boom in publications and developments in the field of III-nitrides is observed.[3] Especially, the Ga(Al,In)N system enables a variety of technologically important electronic and optoelectronic devices. In the case of the applicability of AlGaN in power devices, the material is expected to be capable of high power, high temperature operation and faster switching in comparison to the commercialized arsenides.[4] Additionally in optoelectronics, the wide bandgap of AlGaN alloys can be used for the realization of light emitting diodes and lasers in the UV from 200–365 nm.[5, 6]

Unfortunately, AlGaN alloys, like other wide bandgap semiconductors, suffer from low achievable free carrier concentrations and high optical absorption due to defects, thus preventing the broad and straightforward utilization of AlGaN in practical devices. In general, as the bandgap of a semiconductor increases, it becomes difficult for efficient n-type and p-type doping.[7] This effect is due to two important properties of these materials: (1) the ionization energies of donors and acceptors in wide bandgap semiconductors like AlGaN are higher in comparison to classical semiconductors like Si and GaAs and (2) the compensation of n- and p-type dopants due to an enhanced incorporation of intrinsic and extrinsic point defects that strongly determine the electronic and optical properties of the semiconductors.[7] The first statement cannot be influenced by any kind of growth procedure and is expected to be an intrinsic property of the semiconductor and the dopant. The second statement is a direct consequence of the wide bandgap and the contribution of the Fermi energy to the formation energy of charged point defects, which becomes more significant as the bandgap increases.[7]

The larger the energy gap, the higher the concentration of compensating point defects in the case of n-type and p-type doping and consequently, the free carrier concentrations that can be reached by doping is lowered.

The relatively low free carrier concentrations that can be achieved with current technology available make it difficult to produce AlGaN-based semiconductor laser devices in the deep UV, especially for the necessary high carrier density injection. One way to circumvent this difficulty is the realization of AlGaN frequency doubling devices to convert coherent light into the UV range. Here, free carriers are not necessary as the material is solely used for its optical properties. AlGaN-based lateral polar structures are promising for the realization of light converters into the UV.[8-12] Nevertheless, another approach that could be used to control the formation energy of point defects is by the management of the Fermi-level[13] and therefore reducing the incorporation of compensators of the n- and p-type dopants.

1.1   Motivation and Approach

This thesis, "Polarity Control and Doping in Aluminum Gallium Nitride", consists of three major components presented in Chapters 3, 4, and 5. The goals of Chapter 3 and 4 are to overcome two major challenges encountered in AlGaN devices and AlGaN lateral polar structures. Overcoming these challenges is necessary to be able to produce highly efficient optoelectronic devices in the deep UV, like UV-lasers and LEDs, or high frequency field effect transistors. The two challenges that will be solved are: (1) incorporation of compensating charged point defects in p- and n-type AlGaN alloys which limit the free carrier concentrations and the mobility at high doping concentrations and (2) control of growth and quality of AlGaN lateral polar structures (LPS) for second harmonic generation and lateral p/n-junctions.

For challenge (1), as addressed in Chapter 3, it will be shown that above bandgap UV-illumination during growth can control the incorporation of compensators in highly doped GaN. GaN doped with Mg is used as a model system to show the feasibility of the point defect control scheme, which can influence the incorporation of the compensators. Chapter 3, "Point Defect Control in GaN", discusses the challenge of compensation and the solution by above bandgap illumination in three sections. In the first section, the compensation process

and the major intrinsic and extrinsic point defects that limit the conductivity of GaN:Mg as a function of the Mg doping concentration is investigated. The second section discusses the major theoretical background of the above bandgap UV-illumination during the growth of highly doped semiconductors, as an example of a Fermi-level point defect management scheme to control compensators. In the last section of Chapter 3, the control scheme will be applied to GaN:Mg to show the reduced incorporation of the typical point defects V_N, H and O. In conclusion, the feasibility of the scheme for p- and n-type material will be demonstrated.

For challenge (2), in Chapter 4, it will be shown that the growth conditions, more specifically the (Ga) supersaturation, strongly controls the quality of III- and N-polar AlGaN domains grown side-by-side in a lateral polar structure. The major challenge of the height difference of N- and III-polar domains that is typically observed, will be demonstrated to be due to mass transport between the domains, depending on the Ga supersaturation. Chapter 4 discusses the growth and the fabrication of AlGaN lateral polar structures in three sections. In the first section, the design of LPS for second harmonic generation will be discussed since it is one of the possible major applications of a LPS. The second section focuses on the growth and fabrication of a GaN LPS with investigating the influence of patterning of the templates by etching and the growth conditions on the simultaneous growth of Ga- and N-polar domains in proximity. The third section of Chapter 4, discusses how the Ga content in the AlGaN domains influences the mass transport of AlGaN material between the domains. In conclusion, high quality GaN and AlN LPSs will be presented as possible waveguides and conversion devices to achieve second harmonic generation of coherent light into the deep UV range.

Following the results and achievements of Chapters 3 and 4, it will be shown in Chapter 5 that the quality and efficiency of lateral p/n-junctions can be increased. Therefore, the optimized growth conditions of Chapter 4 and the applied point defect control scheme of Chapter 3 lead to the growth of high quality lateral p/n-junctions with reduction in compensating defects. This is the first demonstration of the applicability of the Fermi-level point defect control scheme on the fabrication of a practical device.

1.2   Properties of AlGaN: Crystal Structure, Polarity, and Bandgap

This work focuses on the growth and characterization of GaN and AlGaN based lateral polarity structures. In order to allow an in depth discussion of the results gained within this work, the basic properties of the binary systems AlN and GaN and the ternary system AlGaN are discussed in this chapter. The focus lies on the general crystallographic and optical properties as they are most important for the understanding the rest of the work. More detailed discussion will be provided as required throughout the other chapters.

The ternary compound AlGaN is an important semiconductor that can be used for optoelectronic and electronic devices such as UV-lasers and light emitting diodes[14] or heterostructure field effect transistors.[15, 16] The two major properties of AlGaN that are discussed within this thesis are its wide bandgap and its polarity. The polarity arises from crystal structure and lattice distortion of the material. As illustrated in FIG. 1, the atoms of AlGaN are arranged in the wurtzite structure. The III-atoms and the N-atoms are arranged in hexagonal sub-lattices. The unit cell is hexagonal and non-centrosymmetric. The polar axis is along the c-direction. The configuration in which the III-atoms bond with 3 bonds toward the surface is referred to as the N-polar (or -c orientation), while the 180° rotated configuration is referred to as III-polar (or +c orientation). The two possible polarities along the c-axis are true symmetry operations and, therefore, should not be mistaken with surface termination as either orientation can be terminated with either with III-metal or N atoms.
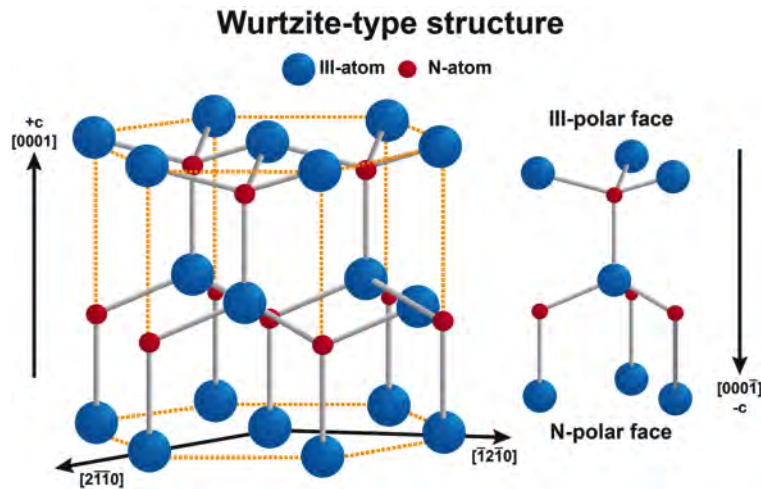

FIG. 1: Wurtzite structure of AlGaN with III-polar and N-polar orientation.

The nitrogen atoms feature a strong electronegativity in comparison to the III-metal atoms, which results in a dipole moment and ultimately in an internal electric field. Deviation of the real atomic charge distribution from the point charge model of the ideal wurtzite lattice (distortion of tetrahedral angles) results in a macroscopic spontaneous polarization, P, in the c-direction of the crystal. Any deformation of the unit cell by external or internal stress leads to a piezoelectric polarization[17] that can overlap with the spontaneous polarization.[18] The origin of such stress can be, for example, lattice mismatch between an epitaxial layer (AlGaN) and a substrate. The combined internal electrical field can have strength in the order of a few MV/cm and is offset by charge accumulation at the surface or interface of the semiconductor on the order of 10^{13} cm^{-2}. As a result of these internal fields, a spatial separation between holes and electrons may occur in quantum structures due to the quantum-confined Stark effect, leading to a limitation of the radiative recombination efficiency of optoelectronic devices.[19] One particular solution to overcome those large internal electric fields is the growth of AlGaN on the m- or a-plane substrates (non-polar growth), where there is no polarization-related electrical field.[20] However, typical non-polar substrates are expansive[21] and growth seems to be more difficult and not yet fully understood, leading to some preferences for the growth on cheap, c-plane sapphire substrates. The polarization effects can be used beneficially for two major applications: (1) to achieve two-dimensional electron gases (2DEG) for field effect transistor applications and (2) for lateral polar structures (LPS) for lateral p/n junctions[22] and for frequency doubling structures to tune light into the UV.[8] In case of (1), the polar c-axis can be used to grow pseudomorphic AlGaN and GaN layers in c-direction and achieve high-frequency transistors based on AlGaN/GaN with high electron drift velocities. Since any discontinuity in polarity generates at the interface compensating charge, a 2DEG can be created at AlGaN/GaN or AlGaN/GaN/AlGaN interfaces.[23] In case of (2) a LPS can be grown with AlGaN using layers with different polarity side-by-side in a lateral structure. As discussed above and illustrated in FIG. 1, the polarity of AlGaN is not given by the surface termination of the crystal.

Nevertheless, the surface activities are different for the two polarities, strongly influencing the growth mode. It has to be mentioned, that the surface polarity has a significant influence on the incorporation of native and extrinsic defects, e.g., N-polar GaN exhibits two orders of magnitude higher incorporation of oxygen during the growth, leading to strong n-type

conductivity. Similar results are found for example in ZnO or InN and explained by a polarity-dependent formation energy of these defects.[24, 25] One example for an application of the polarity dependent defect incorporation is a lateral p/n junction based on LPS. Such lateral polarity p/n junctions are formed by the growth of Mg doped N-polar and Ga-polar GaN side-by-side since Ga-polar GaN domains show p-type conductivity, while N-polar domains remain n-type because Mg is over compensated by the native oxygen donor. In addition, the change of polarization along the c-axis in a lateral polar structure can be used to change the sign of the non-linear coefficient. The non-linear coefficient of AlGaN is big enough to use it for frequency doubling and the transparency of the material makes it perfect for conversion into the UV range. These LPS can be applied for quasi phase matching with AlGaN to achieve constructive interference of the second harmonic waves in the crystal. A detailed description in growth and fabrication and use of LPS, especially for second harmonic generation, will later be presented in Chapter 4. The difference in the incorporation of defects depending on the Ga-polarity will be discussed in Chapter 3.

However, the second important property of AlGaN as part of the III-nitrides lies in the wide bandgap of the material, which can be used for UV and deep UV applications. Depending on the Al composition of the AlGaN alloy, the room temperature bandgap can be between 3.4 eV–6.2 eV. This range is much wider in contrast to other III-nitrides, like InGaN alloys (0.7 eV–3.4 eV), which are used for infrared to near UV spectral range. As a consequence, AlGaInN alloys could be used from IR to deep UV spectral range. The bandgap is a direct result of the covalent radius and the bonding strength between the N atom and the group III-metal atom. Since III-atoms have different ionic radii and different bond energy with nitrogen, different III-nitrides have different lattice constants and bandgaps. AlGaN alloys are observed to be fully miscible in contrast to InGaN alloys that suffer from phase separation. Lattice parameters, bandgaps and transparencies of different III-nitrides are compared in Table 1. The values for AlN and GaN displayed in Table 1 were measured from layers grown within this work and are comparable to those available in the literature.[18, 19, 26]

Table 1: Material Properties of III-Nitrides

Material Property	AlN	GaN	InN
a_0 (nm)[a]	0.3111	0.3188	0.3537
c_0 (nm)[b]	0.4981	0.5185	0.5703
Bandgap (eV)[c]	6.1[d]	3.4	0.7

[a] Reference [18, 19, 23], [b] Reference[18, 23], [c] Reference [18], [d] Reference [27-30]

The wide bandgap of AlGaN results in a transparency between 200 nm–365 nm, which makes it a perfect candidate for UV-based opto-electronic devices. Thus, many AlGaN-based devices, especially LED's, have been proposed and demonstrated by various groups. These emitters had an emission range between 210–350 nm[5] and an external quantum efficiency (EQE) of up to 6%.[6, 31-41] However, the main obstacles in the fabrication of AlGaN-based LEDs are the relatively deep acceptor and donor levels, the high growth temperature of AlN and Al-rich AlGaN, and the low EQE especially at shorter wavelength. The main applications for UV-LEDs will be for solid state lighting, biological and chemical markers and UV-disinfection. In addition, there is some interest in the fabrication of semiconductor-based UV injection lasers to substitute existing gas lasers or for new applications such as field spectrometers/detection systems. However, at this point, only a few optically pumped AlGaN-based UV-lasers have been made with demonstrated emission below 336 nm.[42] Although, the short UV emission of devices is a direct consequence of the wide bandgap of the alloy, point defects can influence the device efficiency. The influence on point defects on the quality of GaN films will be discussed in Chapter 3.1.
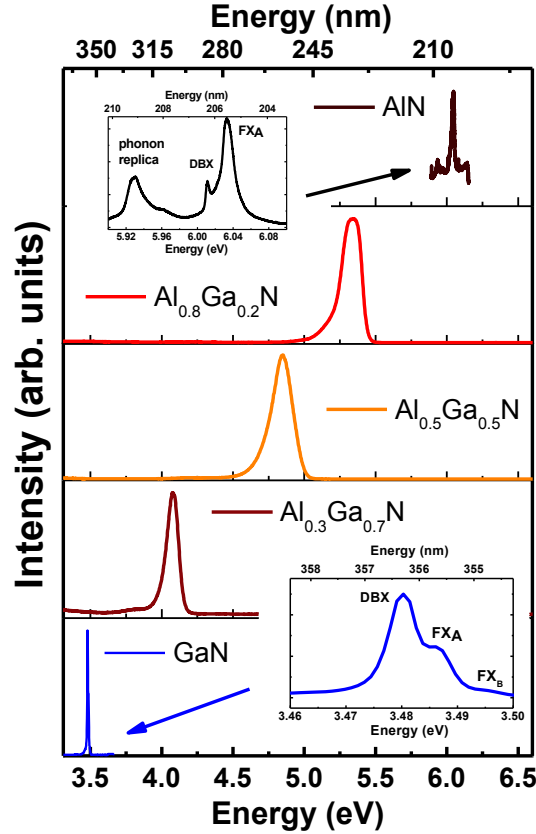
FIG. 2: Low temperature (4 K) Photoluminescence of the band edge signal of AlGaN over the whole compositional range for a few selected samples. All AlGaN films have been grown on LT-AlN and HT-AlN nucleation layers (excluding the GaN film) on c-plane sapphire substrates by MOCVD, leading to III-polar films. The films have a thickness of 700 nm.

Both bandgap and point defects in AlGaN can be measured and investigated by photoluminescence. To visualize the importance of AlGaN for optoelectronics in the UV, the excitonic near bandgap luminescence of this alloy is presented over the whole compositional range in FIG. 2. The AlGaN films have been deposited on low temperature (LT) and high temperature (HT) nucleation layers leading to III-polar AlGaN films. More details can be found in chapter 2.5.3. By analyzing the optical transitions, point defects like donors and acceptors as well as the bandgap, can be determined. Typically, the most intense near-bandgap transitions that can be observed are the transitions of free excitons or bound excitons. A free exciton is a bound electron hole pair drifting freely through the lattice. Due to the Coloumb interaction between the electron and hole the energy of the free exciton is reduced in comparison to the bandgap. The free exciton forms hydrogen-like states ($n = 0,1,2...$) in the band of the semiconductor. The largest energy difference is the binding energy of the exciton.

In AlGaN, these binding energies are in the range of several tens of meV and they increase strongly with the bandgap. For GaN, typical free exciton (FX_A) binding energies of ~25 meV[43-46] and for AlN binding energies of ~50 meV[27-29, 47] can be found. Due to the band structure of the valence band (heavy holes, light holes and split-off holes), three different free excitons, called FX_A, FX_B and FX_C, can be observed, typically with decreasing intensity due to the occupation probability. It should be mentioned that strain and accordingly electric fields (piezoelectricity) in the crystal can shift the free exciton positions. Thus, in order to allow an unambiguous determination of the exciton binding energy, strain and electric fields need to be measured (e.g. by High Resolution X-ray Diffraction or Raman) or controlled (e.g by doping during the growth).

If impurities are present in the crystal, free excitons can bind to neutral donors and acceptors, called donor bound exciton (DBX) and acceptor bound exciton (ABX). Due to the additional binding energy between the free exciton and the impurity, ABX and DBX are typically observed red shifted compared to the free exciton position (localization energy). Bound excitons are typically observed at very low temperatures in the PL spectra, since their binding energy to the impurity is usually smaller than the thermal energy at room temperature. Therefore, an increase of temperature towards room temperature leads to the dissociation of bound excitons and free exciton transitions gaining in intensity; this effect is used to distinguish between the bound and free excitons in PL.[48, 49] The binding energy of DBX are mostly smaller than the ABX binding energy because of the deep levels of acceptors in the wide bandgap of AlGaN. The major DBX that can be found in (Ga-rich) AlGaN PL spectra is due to oxygen or silicon, while when doped with Mg several ABX transitions are present.

Apart from the near band edge luminescence, deep luminescence may be observed. This includes emission from deeply bound defects, as well as transitions of a donor level to an acceptor level. The latter are called donor acceptor pair (DAP) transitions and will be of major concern within this work.

An identification of all of these transitions can be used as a tool to determine the presence of native and extrinsic point defects, as well as to help understand activation and compensation in doped crystals. The Mg doping of GaN is discussed in Chapter 3.1, where a detailed description of all mentioned transitions and their relation to the crystal quality is discussed.

2.   Experimental Details

In this chapter, the growth and measurement techniques that have been used within this thesis are discussed. Most of these techniques are, in general, standard techniques in the field of applied physics and material science and will not be discussed in detail. Nevertheless, some experimental details need a deeper discussion as they are important for a complete understanding of the following chapters. This includes, for example, calibration of luminescence spectra, Hall investigation of p-type GaN, and modifications of the metal organic chemical vapor deposition (MOCVD) setup.

The main aspect of this work is the growth of AlGaN and fabrication of AlGaN-based devices using MOCVD. For a basic understanding of MOCVD, vacuum technology and growth, the reader is referred to the book of Dhanaraj *et al*. (Handbook of Crystal Growth)[50] and for better understanding of the growth process to Burton *et al*.[51] on the growth of crystals and the equilibrium structure of the surface. Since MOCVD was used for the growth of all investigated samples in this work (Chapters 3, 4, and 5), the MOCVD reactor design and its modifications are presented first (Chapter 2.1). The most important modification, a UV-illumination setup on top of the reactor, will be discussed in reference to its illumination capability (power density and wavelength). As demonstrated in this thesis, this UV setup is capable to affect the incorporation of extrinsic and intrinsic defects in doped of AlGaN films and other wide bandgap semiconductors by exploiting the so called Fermi-level effect (Chapter 3.2).

In addition, two photoluminescence (PL) and photoluminescence excitation (PLE) setups will be described (Chapter 2.2) that were used to measure doped GaN layers grown with the previously mentioned MOCVD reactor. The first setup was established as a part of this work at the Materials Science and Engineering Department at the North Carolina State University (NCSU). It was intended to use it for the investigation of point defects in AlGaN. Most optical spectra on GaN presented in Chapters 3.1 and 3.3 were taken with this setup. In addition, PL and PLE setups located at the Technical University (TU)-Berlin were used as part of the collaboration between NCSU and TU-Berlin for the investigation of excitation

channels of defects and transfer processes in Mg-doped GaN. The PLE results can be found in Chapters 3.1.1 and 3.3.3 where an investigation of GaN:Mg is presented.

For the electrical characterization, a Hall effect measurement system was used. In Chapter 3, a comprehensive discussion of the compensation of GaN:Mg is presented and a detailed description of the approach to the Hall effect measurements is essential and, therefore, part of Chapter 2.3.

Other used characterizations and techniques explained in this chapter were mostly performed other group members or collaborators. Most other characterization techniques were used within their standard limitations and no detailed discussion is necessary. However, the description of the secondary ion mass spectroscopy (SIMS) setup will be an exception. Details of the quantitative measurement of atomic defect concentrations will be explained in Chapter 2.4 as they are crucial for the understanding of achieved results.

2.1   MOCVD Reactor and the Attached UV-Illumination System

A low pressure (20-100 Torr) vertical showerhead MOCVD reactor was used for the growth of all samples and structures discussed in this thesis. In MOCVD, films are deposited onto a substrate by diffusion, decomposition, and reaction process of precursors that are either in metalorganic or hydride form. The MOCVD system is specifically designed for AlGaN alloy growth, including pure GaN and AlN. Both H_2 and N_2 can be used as carrier gas. For metal sources, it is equipped with trimethylgallium (TEG) as a source for gallium, trimethylaluminium (TMA) as a source for aluminum, and ammonia as a source for nitrogen (N). For doping purposes, silane as a source for silicon and bis-(cyclopentadienyl)magnesium (Cp_2Mg) as a source for magnesium were used. A schematic of the reactor is shown in FIG. 3 (a). The reactor contains a 13 cm diameter water cooled quartz tube and a radio frequency (RF-)induction heated SiC coated graphite susceptor. Growth temperatures of 500–1250°C can be attained. The susceptor is rotating at a distance of 5 cm to the gas inlet and the cracking of the precursors occurs straight at the hot zone above the substrate. Since the reactor chamber is open to the atmosphere when loading the substrates, a rotary pump and a turbo-molecular pump are attached to reach a necessary base pressure of low 10^{-6} to high 10^{-7} Torr before the start of the growth.
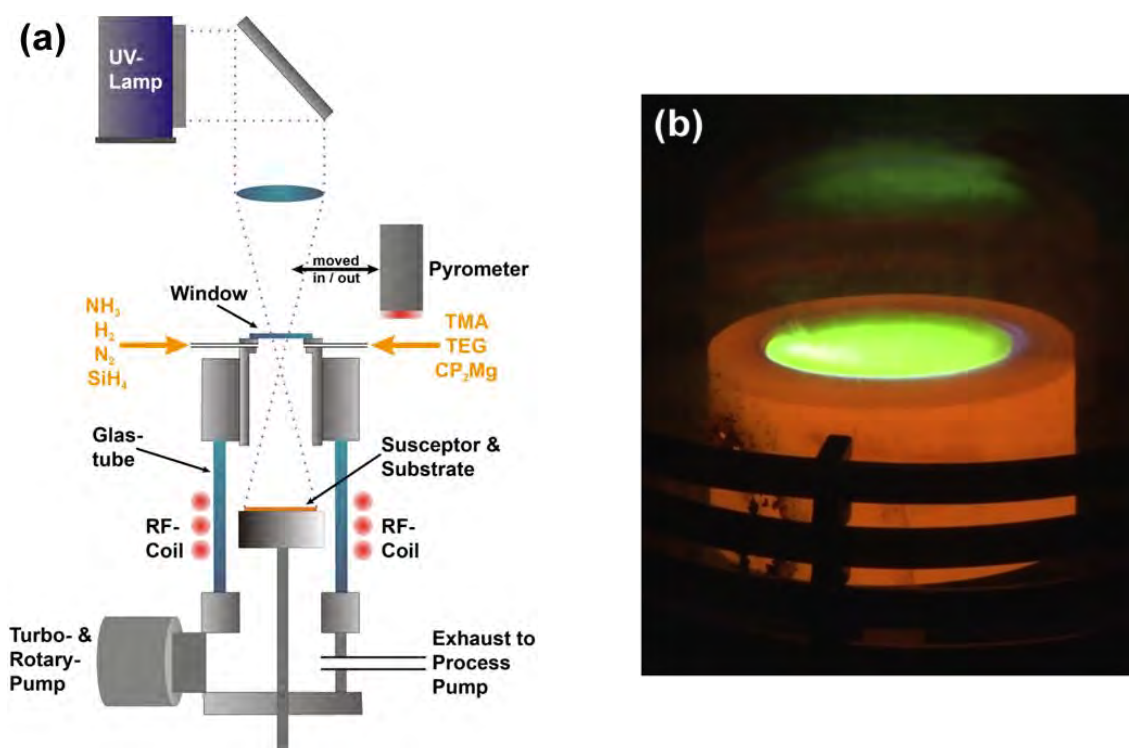
FIG. 3: (a) Systematic diagram of MOCVD reactor (b) Photo of an illuminated sapphire surface during the growth of a doped GaN layer. The yellow/greenish photoluminescence arises from the UV excitation of point defects in the sapphire substrate.

One of the special features of this reactor is a UV-transparent window (sapphire MDC 9722205) on top of the gas inlet. Under normal operation conditions of the reactor, the wafer temperature can be monitored by a pyrometer above the window. When a stable growth temperature is established, the pyrometer can easily be removed and substituted by a UV illumination system: a Mercury arc lamp (Oriel 6287), 45° mirror and a UV lens, which disperses the light of the lamp uniformly onto the entire substrate surface. This system is installed on top of the reactor to illuminate the surface of the film during the growth. FIG. 3 (b) shows the illuminated wafer surface during the growth of GaN. For light with energies larger than the bandgap of GaN (~2.9 eV at 1040°C), a power density of ~1 W/cm^2 can be reached on the surface. This power density was measured using a photodetector (Ophir PD 3000) positioned in the reactor chamber at the same distance from the window as substrates. To determine the above bandgap power, first the total power density was measured followed by the measurement of below bandgap power density using a 1.4 μm thick undoped GaN

layer grown on c-sapphire as an absorption filter. Following this measurement, the above bandgap power density on the wafer surface was calculated as the difference between the total and below bandgap power density. Details on the determination of the power density and implementation of the UV-illumination system have been published as a part of the investigation of the influence of above bandgap illumination on the activation of Mg-doped GaN[52] and will be discussed in detail in Chapter 4.

2.2 Photoluminescence and Photoluminescence Excitation

Photoluminescence and Photoluminescence excitation were used to investigate the extrinsic and intrinsic point defects of GaN, since they determine the crystal quality and influence conductivity and optical transitions. The measured optical transitions may give hint to the species of these defects. Therefore, MOCVD-grown GaN and AlGaN films have been consequently investigated with PL and PLE after growth. In order to assure timely measurements and fast feedback to the growth, a new setup was established as a part of this work at the NCSU. The assembled setup is displayed in FIG. 4.
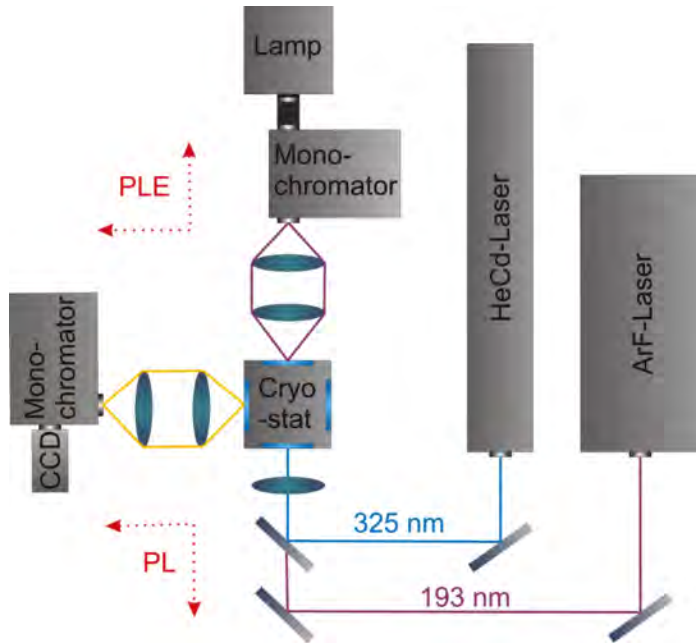

FIG. 4: PL and PLE setup with choice between HeCd- or ArF-laser for PL and tunable excitation with lamp and monochromator.

The PL setup uses a 56 mW (cw) HeCd-laser with a wavelength of 325 nm or an 8 mJ (FWHM 5 ns pulse) ArF-laser (Coherent Xantos) at 193 nm for the excitation of the samples. Above bandgap excitation can therefore be guaranteed for AlGaN over the whole compositional range. Samples are mounted on a cold finger into a closed cycle helium cryostat from Janis (SHI-RDK-415D) allowing temperature dependent measurements in the range from 3-300 K. Thus, bound exciton transitions from AlN, GaN and AlGaN can be measured. Temperature dependent PL was mainly applied to determine binding energies of bound excitons. The luminescence spectra of the samples were recorded by using a Princeton Instruments SP2750 3/4 m spectrometer attached to PIXIS 2K charge-coupled device (CCD) camera, which was calibrated before each measurement by using a He- or Ne-lamp. The setup resolution of 0.01 nm was adequate to measure any excitonic transition in AlGaN. In addition, PLE spectra were measured by using a 1000 W Hg-lamp attached to a monochromator (220–650 nm) by exciting the sample through the second window at the opposite side of the cryostat. The windows of the cryostat were made of UV grade fused silica (SiO_2) to be transparent for the high power 193 nm excitation. Power dependent PL on GaN samples was realized by using neutral density filters varying the HeCd-laser excitation power between 56 mW–100 μW. In addition to the PL and PLE measurements at the NCSU, high-resolution PLE measurements were performed at the TU-Berlin as part of a collaboration program. This PLE setup uses a dye laser (Coherent FL 3001) and a XeCL-Excimer laser (Coherent, 308 nm, 100 Hz) for pumping the dye laser. The applied dyes were pure LC3400 (p-Terphenyl), LC3570 (BMQ), LC3590 (DMQ) and LC3690 (QUI) allowing excitation in the spectral range from 3.2 to 3.6 eV with 5 μJ (FWHM 20 ns) pulse energy. The dye mixtures were chosen to fit the necessary excitation range for PLE on GaN:Mg or to shift the wavelength of the background dye luminescence out of the spectral detection window. For the detection of the luminescence, a double-monochromator (Spex 1701) with a spectral resolution of 50 μeV was used. All PLE spectra have been corrected for the wavelength dependent individual dye efficiency.

2.3   Hall Effect Measurements and Contacts

Electrical characterization of the grown samples was one of the keys to investigate the crystal for extrinsic and intrinsic point defects and, more importantly, the incorporation and activation of Mg. Hall effect measurements were performed on an Ecopia HMS-3000 Hall effect measurement system using the four-contact van der Pauw method. In general, this system is designed to measure at room and liquid nitrogen temperature. In order to allow temperature dependent Hall effect measurements, a heater was mounted on the back-side of the sample holder and a thermo-couple was positioned on the front of the sample. Hence, the determination of the temperature dependence of the resistivity, mobility and free carrier concentration of as-grown and annealed films at in the range from 77–500 K was possible. In general, this information can give deep insight in the activation or compensation stage of a sample, but good ohmic contacts are needed since the measurement relies on ohmic behavior of the contacts. For the annealed GaN:Mg samples, Ni/Au-contacts were used.[53-55] Subsequently, these contacts were annealed in a furnace in the ambient atmosphere for 10 min at 650°C. The metallization for the contacts was made by electron-beam evaporation of 30 nm/70 nm Ni/Au metal layers. Nevertheless, as-grown samples (especially GaN:Mg samples with UV-illumination during the growth) had to be measured with indium contacts, since the Ni/Au-contact annealing is expected to activate samples at least partially or change defect concentration. It should be mentioned that the contact resistance of indium is expected to be slightly higher than that of the Ni/Au contacts. Extensive studies of activation of p-type GaN were concluded with post growth annealing at 650°C in N_2 for 2 hours; after this annealing step, the samples were considered "fully activated" and were used as a reference for In contact resistance.[56] In contrast, n-type samples had much higher free carrier concentrations in comparison to p-type GaN and indium contacts are usually sufficient.

2.4   Other Techniques and Measurements: SIMS, XRD, AFM & SEM

In addition to the investigation of samples with PL, PLE and Hall effect measurements, a few standard techniques were used to gain deeper insight into the materials properties:

- Annealing of samples was performed in a furnace. Typical annealing temperatures that were used varied between 500–750°C. Nitrogen was used as ambient gas although any gas could be hooked up to the system. The gas flow in the furnace was varied between 10–1000 sccm. The less common feature of this furnace was an UV-lamp that could be used for illumination during annealing. This UV lamp was a 1000 W mercury arc lamp.

- Secondary ion mass spectroscopy (SIMS) on AlGaN was performed to investigate the atomic concentrations of dopants and extrinsic defects incorporated into the crystal during growth. SIMS measurements were performed using a CAMECA IMS-6f with a magnetic sector analyzer. During the investigation of the samples, especially the incorporation of H, O and C was monitored; these elements are the main compensators and unintentional point defects in doped and undoped GaN (Chapter 3). Specially prepared standards were used for the calibration of quantitative analyses. In the case of H concentrations, analysis for H was achieved using Cs+ primary beam and detection of negative secondary ions. The 15 nA primary sputtering beam was typically rastered over a 120 μm x 120 μm area with ions detected from a 30 μm diameter region at the center of the crater. In the case of Mg, an $O2^{+}$ primary beam with 50 nA current rastered over a 180 μm x 180 μm area and positive secondary ions detected from a 60 μm diameter area at the center of the crater were used. Quantification was achieved for H and Mg by analysis of ion implanted GaN samples with a known implantation dose. The implanted dose in reference samples was confirmed by the analysis of pieces of silicon implanted at the same time as the GaN samples. The results from silicon were compared with other well-characterized implants into silicon from a standards library. The implanted GaN sample was analyzed every time simultaneously with the samples of interest.
  The SIMS measurements were performed by Dr. Fred Steve and his co-workers at the Analytical Instrumentation Facility at NCSU.

- High-resolution X-ray diffraction (XRD) spectra were acquired to study the crystalline quality and alloy composition of AlGaN epilayers. All HRXRD measurements were

performed using a Phillips X'Pert Materials Research Diffractometer using Cu Kα1 radiation of λ = 1.54056 Å. The dislocation density was determined from omega rocking curves recorded in double-axis configuration. Taking the full-width-at-half-maximum (FWHM) of the (00.2) and (30.2) rocking curves, the total number of edge and screw-type dislocations was estimated.[57] The composition of AlGaN films was assessed from relative lattice parameters measurements taking the separation of the AlGaN film and substrate Bragg peaks in a symmetric (00.2) omega-2theta scan.[58] The XRD measurements were performed by Milena Bobea of the Wide Bandgaps Group at NCSU.

- Atomic force microscopy (AFM) images were taken on various samples to investigate the influence of different processes (e.g. etching and cleaning) on the surfaces or determine the roughness of grown films. An Asylum Research MFP-3D with a silicon tip in AC air topography (non-contact) mode was used. Most measurements were done in collaboration with Anthony Rice and Isaac Bryan of the Wide Bandgaps Group at NCSU.

- Scanning electron microscope (SEM) images of LPS were taken using a JEOL JSM-6400F Field Emission SEM with a 5 kV accelerating voltage. The measurements were performed at the Analytical Instrumentation Facility at NCSU by Wei Guo and Joseph Rajan of the Wide Bandgaps Group at NCSU.

- Raman spectra were measured at the Technical University of Berlin by using a Dilor XY-800 with an attached Ar-ion laser. Raman measurements were done in collaboration with Ronny Kirste of the Wide Bandgaps Group at NCSU and previous member of the Institut für Festkörperphysik at the Technical University of Berlin.

- Transmission electron microscopy (TEM) cross-section samples were prepared using a FEI 3D Quanta FEG Focused Ion Beam system. Transmission electron microscopy (TEM) was performed with a JEOL 2000FX operating at 200 kV. TEM was measured by Lindsay Hussey of the Wide Bandgaps Group at NCSU.

2.5 Experimental Details on the Grown Samples

2.5.1 Growth of Samples for the Investigation of Point Defects in GaN:Mg

All GaN:Mg samples for Chapter 3 were heteroepitaxially grown under mass-transport-limited conditions on (0001) c-plane sapphire. Films consisted of 700 nm GaN:Mg layers deposited on 1.3 μm undoped GaN. The p-type films were deposited at a temperature of 1040°C under a V/III ratio of 200 and a reactor pressure of 20 Torr. This V/III ratio was attained by flowing 67 μmol/min of TEG and 0.3 slm of NH_3, under a total flow rate of 7.4 slm using nitrogen as an inert gas, which is used as a common diluent gas in MOCVD growth for low supersaturation values.[59] Bis-(cyclopentadienyl)magnesium (Cp_2Mg) was used as Mg precursor. The doping level ranged from $5x10^{17}\,cm^{-3}$ to $5x10^{19}\,cm^{-3}$. A 20 nm low temperature (650°C) AlN nucleation layer was deposited on sapphire prior to GaN growth, thus providing for a Ga-polar films. A pre-growth H_2 annealing was needed to remove unwanted contaminants and to create a suitable sapphire surface and an NH_3 annealing was performed to nitridize the AlN surface to provide for the Ga-polar GaN growth.[27, 28] If needed, activation of the Mg-acceptors was achieved by annealing in a furnace in N_2 atmosphere for 2 hrs. In order to find the ideal annealing temperature, experiments using temperatures between 450°C and 700°C were performed. At 550–650°C the samples were fully activated and the lowest resistivity was observed using Hall effect measurements.

### 2.5.2 Growth and Fabrication of GaN Lateral Polar Structures

The fabrication and growth of GaN-based lateral polar structures for Chapter 4 will be discussed in the following. Lateral polar structures used in Chapter 4 for second harmonic generation were patterned into microns-wide stripes while the lateral polar p/n-junctions used circular structure. Depending on the purpose, the lateral polar structure design will be discussed in detail in Section 4.1.

GaN was periodically poled by a three-step fabrication process presented in FIG. 5. A similar fabrication method can be found in literature.[22, 60] The first step consisted of the growth of a 20 nm thick low temperature-(LT-) AlN film at 650°C on c-sapphire. The nucleation layer was used to assure the Ga-polarity for GaN and was also used for the GaN:Mg growth. Prior to the growth of nucleation layer, the sapphire substrate was exposed to H_2-etching for 7 min,
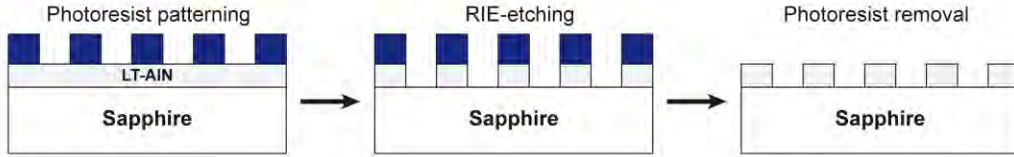
followed by NH$_3$-annealing for 4 min. The H$_2$-etching is needed to remove unwanted contaminants (e.g. fluorine)[61] and create a suitable step-and-terrace sapphire surface morphology. The NH$_3$-annealing is used to modify the sapphire surface and form a thin AlN layer to control the polarity. A detailed discussion on these treatments can be found in the literature.[59, 60, 62]
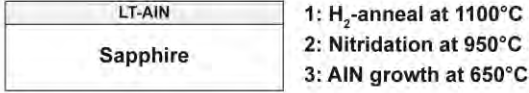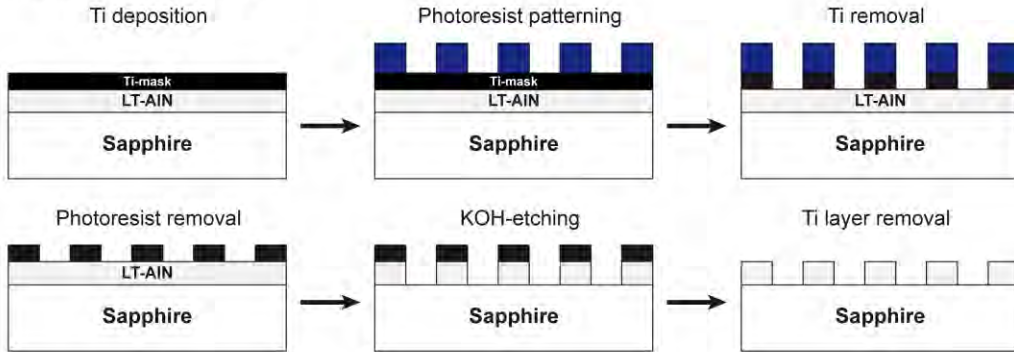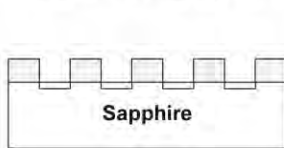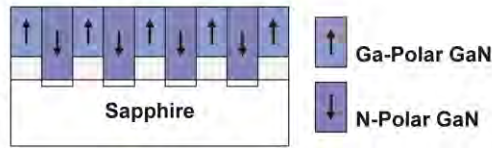
FIG. 5: 3-step Fabrication process of a GaN based lateral polar structure. (a) Growth of a 20 nm AlN buffer layer. (b) Fabrication of the template including photoresist patterning and etching with KOH and RIE. (c) GaN overgrowth of the patterned template with MOCVD results in lateral polar structures.

The second step included the patterning of the AlN nucleation layer into periodic stripes or circles by lithography and etching techniques as displayed in FIG. 5 (b). Two different

etching techniques were used: wet etching in potassium hydroxide (KOH) or reactive ion etching (RIE). The pros and cons of the two etching methods will be presented in Chapter 4.2.1. The lateral p/n-junctions of Chapter 4 were mostly fabricated using RIE etching. The patterning used a lithography mask consisting of stripe widths of 5000 μm, 50 μm, 20 μm, and 5 μm that were oriented in two directions: parallel and perpendicular to the a-plane of sapphire. The two different etching methods required slightly different patterning. In case of the KOH etching, a thin Ti layer (~30 nm) was required as a mask and was deposited by e-beam evaporation. The Ti layer was patterned using standard optical lithography and 5% HF. The exposed AlN stripes were etched for 1 min using a 6M KOH solution at 50°C. Subsequently, the remaining Ti mask was removed using 5% HF. This procedure on the LT-AlN layer resulted in a template with periodic LT-AlN and bare sapphire stripes side-by-side. Alternatively, in the case of RIE etching, the fabrication involved a similar patterning process but without the use of the Ti layer; here, photoresist served as a mask. After patterning, the RIE etching was done for 2 min at a pressure of 75 mTorr and a BCl_3/Cl_2-ratio of 25/25. A RIE power of 100 W resulted in an AlN etch rate of 10 nm/min. The removal of the photoresist after etching resulted in a periodic structure similar to the one produced with KOH etching. After etching, all patterned samples were rinsed in deionized water and blown dry with nitrogen before reintroduction into the MOCVD chamber.

In the third fabrication step, the templates were overgrown with GaN using the MOCVD reactor displayed in FIG. 5 (c). The GaN growth conditions were critical for simultaneous growth of both polarities of GaN as it will be discussed in Section 4.2. For the growth, the total pressure was 60 Torr and the V/III-ratio was varied from 100-800. The growth temperature was constant for all samples and was 1040°C. As an example, the V/III ratio of 200 was reached by flowing 134 μmol/min of Trimethylgallium and 0.6 slm of ammonia, under a total flow rate of 7.7 slm using nitrogen as diluent gas. The V/III-ratio could be varied by changing the ammonia flow rate or adjusting the total flow rate. Before the growth of Ga-polar and N-polar GaN, the patterned template was cleaned of surface contaminants using process conditions by H_2-etching for 20 min at 1100°C, flowing 2 slm of hydrogen at 20 Torr and NH_3-nitridation.[60] The NH_3-annealing was performed for 10 min at 1040°C, flowing 0.82 slm nitrogen and 1.1 slm ammonia at 20 Torr.

This etching and nitridation process was essential for the growth of N-polar GaN domains.[59, 60] This three-step fabrication process resulted in a periodically poled GaN structure with a periodicity of the stripes down to 5 μm and a thickness of around 1.3 μm.

2.5.3 Growth of AlGaN and AlN Lateral Polar Structures

In the case of AlGaN LPS, the same patterning was applied to the 20 nm thick LT-AlN nucleation layers, as discussed in the previous chapter. For the growth of AlGaN LPS, the RIE patterning was used since it results in sharp interfaces between the domains of opposite polarity (discussed in Chapter 4.2.1). The only other change in the process was the addition of a HT-AlN nucleation layer to avoid cracking.[63-65] The fabrication process for AlGaN and AlN LPS is presented in FIG. 6.
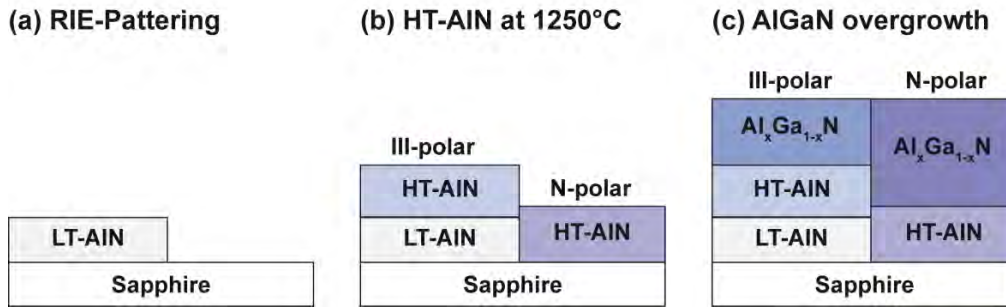
FIG. 6: Growth process of AlGaN based Lateral Polar Structures. (a) RIE patterning. (b) Growth of HT-AlN. (c) Overgrowth of HT-AlN with AlGaN.

The RIE pattering led to stripes of a LT-AlN nucleation layer and (0001) c-plane sapphire presented in FIG. 6 (a). The template was subsequently overgrown by MOCVD with high temperature (1250°C) AlN, resulting in Al-polar domains in areas with an underlying LT-AlN layer and N-polar AlN where the LT-buffer layer was removed (See FIG. 6 (b)). The HT-AlN was deposited at 80 Torr in a hydrogen atmosphere with an NH_3 and trimethylaluminium (TMA) mass flows of 4.46 mmol/min and 21 μmol/min, respectively. In the case AlN LPS, a ~600 nm thick AlN film was deposited. For AlGaN LPS, a 50 nm thick HT-AlN was used as a nucleation layer to prevent cracking of the 600 nm thick AlGaN layer deposited at 1250°C. The AlGaN grown on the Al polar AlN was III-metal polar while the AlGaN grown on the N-polar AlN was N-polar.

3.   Point Defect Control in GaN:Mg

Point defects can strongly influence the electronic and optical properties of semiconductors. In doped AlGaN layers the incorporation of extrinsic and intrinsic point defects can lead to compensation of dopants and reduction of the electrical conductivity. The formation energy of these compensating point defects is a function of the Fermi energy. An increased doping concentration leads to a decrease in the formation energies of charged defects and, therefore, to compensation of dopants in the film. A typical example for this mechanism is GaN:Mg where for doping concentrations above 2×10^{19} cm^{-3}, the formation energy of nitrogen vacancies (V_N) is reduced drastically which leads to highly compensated layers. As a consequence of the large bandgap of AlGaN alloys, ionization energies of dopants are high and doping efficacy is low. Furthermore, point defects lead in high Al content AlGaN alloys to extremely low electrical conductivity in both n- and p-type material. Any compensation can, therefore, be critical and a point defect control scheme would be desirable which allows for high conductivity.

In this chapter using GaN doped with Mg as model system, a scheme to control point defects and compensation will be presented. It will be shown, that the concentration of V_N and H can be decreased by above bandgap UV-illumination during the growth. In order to be able to prove the changes by the UV-illumination, first a detailed analysis of point defects and their optical fingerprint in GaN:Mg will be presented. New lines that appeared in acceptor bound region of GaN:Mg were identified as ABX1, ABX2, and ABX3 transitions using PL, PLE and temperature dependent PL. Following this identification of three acceptor bound excitons the DAP luminescence is investigated very thoroughly and three separated DAP transitions are found. The according donors and acceptors of the newly found DAP transitions were identified using PLE measurements. The results were then used to investigate the passivation and compensation of Mg by H and V_N. It is well known that for doping below 2×10^{19} cm^{-3} passivation of Mg by Mg-H complexes and for doping above 2×10^{19} cm^{-3} compensation of Mg acceptors by nitrogen vacancies determines the electrical properties GaN:Mg. Results

will, therefore, be presented separately for H-passivation of Mg in 3.1.2 and for self-compensation of Mg by V_N-related defects in 3.1.3.

Having a better understanding of point defects in GaN:Mg, the theoretical background of a Fermi-level management by above bandgap illumination will be discussed in Section 3.2. The scheme uses UV-illumination during the growth of semiconductors to control point defect incorporation. It will be demonstrated that UV-illumination during the growth is capable of a reduction of the number of compensating point defects of any doping species. Thus, it can be used for n-type, as well as for p-type doping.

The results of defect analysis in GaN:Mg and the theoretical background of the Fermi-level management by above bang gap illumination will then be used to investigate the influence of UV light on compensating defects in GaN:Mg. Again, it will be distinguished between control of H-passivation in Sections 3.3.1/3.3.2 and self-compensation by V_N-related defects in Section 3.3.3. The UV-growth leads to a change in the optical properties as well as in the Hall resistivity. The reduction of H-passivation can be observed by a strong ABX transition in PL and low resistivity without post growth annealing. The reduction of V_N is accompanied with disappearance of the blue defect luminescence in PL. A significantly reduced incorporation of donors leading to a decrease of the resistivity in GaN:Mg films will prove the feasibility of the concept.

Finally, the applicability of the concept will be presented on low Mg-doped GaN in Section 3.3.4. In this case, the electrical properties are dominated by intrinsic and extrinsic donors. As expected from theoretical considerations, the use of UV illumination leads to a reduced amount of Mg and a n-type conductivity. The reason for this observation is that in low Mg-doped GaN:Mg films, Mg is the compensating point defect (as the host material is n-type) and UV-illumination controls its incorporation. This shows the feasibility of the concept for n-type material.

3.1   Compensation in Highly Doped p-type GaN:Mg

While high n-type carrier concentrations up to 1×10^{20} cm^{-3} can be achieved in GaN using Si as a dopant,[66] high p-type carrier concentrations are much more challenging. Historically, the breakthrough came with the growth of magnesium-doped GaN and subsequent activation via low energy electron beam irradiation (LEEBI) leading to p-type conductivity with hole concentrations around 2×10^{16} cm^{-3}.[1] Currently, magnesium is still the only known dopant that can achieve p-conductivity in GaN.[67] Still, the free hole concentrations are limited to the low 10^{17} cm^{-3} range due to compensation and passivation effects in GaN films grown with MOCVD.[68] Origin of the compensation and passivation of GaN:Mg is the incorporation of point defects or complexes which act often as donors and are incorporated during the growth. In order to understand and overcome the compensation and passivation of the Mg acceptor in highly doped GaN, many efforts were made from many groups over the last decades. Unfortunately, a lot of details of the compensation process by the unintentional dopants and structural defects[69-71] have not been fully understood.

Recent publications by Monemar *et al*.[72] and Lany *et al*.[73] reported about the dual nature of the Mg acceptor and lead to novel insights and enforced interest in acceptors in GaN in the nitride community. A better understanding of the compensation in GaN:Mg can be used as an effective tool to improve growth procedures and come up with new ideas for a better control of compensation of dopants in general.

One of the most prominent extrinsic impurity incorporated into GaN:Mg is hydrogen. Hydrogen arises through the reactions of the precursors like triethylgallium (TEG) and ammonia (NH3) used in the MOCVD process and leads to a high resistivity of unannealed GaN:Mg films after growth. The origin of this high resistivity is the formation of a magnesium hydrogen complex (Mg-H)[74, 75] which passivates the Mg acceptor. The use of post growth thermal annealing[76, 77] is needed to activate the p-GaN through the dissociation of the Mg-H complex.[78, 79] After annealing, free hole concentrations around mid $\sim 10^{17}$ cm^{-3} can be reached[80] using a Mg doping concentration of around 2×10^{19} cm^{-3}. The low carrier concentration at relative high Mg doping is due to the high ionization energy of Mg in GaN[81], which leads to low activation rates of Mg even if all passivation by hydrogen has been removed. Increasing the doping concentration to values higher than Mg:2×10^{19} cm^{-3}, does not

increase the p-type conductivity since the GaN:Mg starts to be self-compensated.[68] In general, self-compensation is understood as compensation of an acceptor (here Mg) or donor by intrinsic or extrinsic impurities. Those impurities are incorporated into the crystal since the Fermi-level moves towards the bands as the doping concentration increases (Fermi-level effect).[82] Thus, the formation energy of impurities changes and high concentrations of unwanted compensating defects are introduced into the crystal. In case of Mg-doped GaN, the free carrier concentration decreases significantly for doping concentrations above 2×10^{19} cm^{-3}. Increased doping concentrations lead to high concentrations of donor-like unintentional point defects, which compensate the free holes originating from Mg. The most prominent self-compensating defect in GaN:Mg is expected to be the nitrogen vacancy (V_N).[71, 83, 84] O has also been suspected to be a part of the self-compensation of GaN:Mg in the high Mg doping regime since O can cause high resistivity values as well as n-conductivity in ~10^{20} cm^{-3} Mg doping regime (which is probably related to inversion domain incorporation induced by metallic Mg).[85] In addition to the self-compensation of Mg-acceptor states by donor-like impurities, interstitial Mg or Mg_N (both would act as donors) may decrease the free hole concentration in the high doping regime.[82]

Parts of the work presented in this chapter are published as part of a collaboration on p-type GaN with TU-Berlin.[86]

3.1.1 Optical Transitions in GaN:Mg

For interpretation of the film quality and influence of the growth conditions on the incorporation of defects into the crystal, an excellent understanding of the optical properties and defect species of the GaN films can be very helpful. Since the investigation of a point defect control scheme in Chapter 3.3 GaN:Mg is used as a model system, an identification of the extrinsic and intrinsic defects introduced into the crystal by Mg doping has to be discussed first. In FIG. 7 the PL spectra of GaN:Mg samples with varying Mg doping concentrations are displayed. The samples have been activated in a furnace at 550°C in N_2 for 2 hours to remove hydrogen passivation of Mg (described in detail in Section 3.1.2) and to be able to investigate the ABE transitions caused by Mg. In order to visualize the influence of the Mg doping on the optical traces in the lower doping regime the luminescence of the doped samples is compared to that of an undoped GaN sample. In unintentionally-doped (NID) GaN, as well as in the low

Mg-doped samples (8×10^{17} and 1×10^{18} cm^{-3}), free A- and free B-exciton transitions can be observed. The energetic positions at 3.487 eV (FXA) and 3.495 eV (FXB) in the doped samples suggest a compressive strain in the layers due to the heteroepitaxial growth on c-sapphire (thermal and lattice mismatch). For comparison, the relaxed positions of the free exciton transitions in nominally undoped GaN samples grown by hydride vapor phase epitaxy (HVPE) were found at 3.478 eV (FXA) and 3.484 eV (FXB)[87] which highlights an energetic difference of 9 meV (FXA) and 11 meV (FXB) in the investigated samples. Raman measurements showed the strain sensitive E_2(high) mode at 567.3 cm^{-1} for our GaN films grown on sapphire, which if compared to the relaxed position at 567.0 cm^{-1}, confirms the observation of a slight compressive strain.
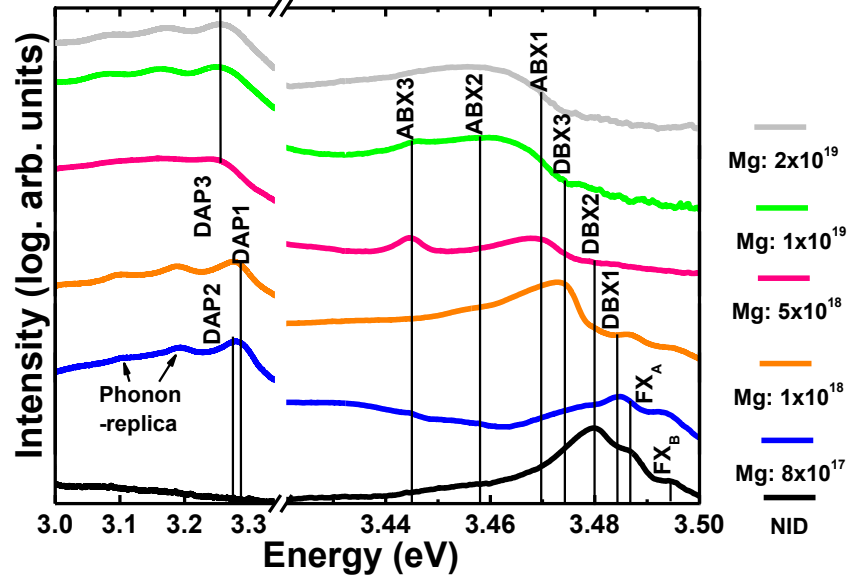
FIG. 7: Low temperature (2K) PL spectra of Mg-doped GaN samples with a doping concentration between 8×10^{17} - 2×10^{19}cm^{-3}. For comparison a spectrum of an undoped GaN samples is displayed. Mg doping leads to three different DAP and many BE transitions.

In addition to the free excitons, three different DBX transitions can be found in the spectra presented in FIG. 7: DBX1 at 3.483 eV, DBX2 at 3.480 eV and DBX3 at 3.474 eV. It has to be mentioned that the DBX3 transition is not very well pronounced in the PL spectra presented in FIG. 7. However, it can be identified using its appearance in the PLE spectra as presented in FIG. 8. The increase of Mg doping leads to the appearance of ABX transitions. Three ABX are identified in the spectra of FIG. 7: ABX1 at 3.469 eV, ABX2 at 3.457 eV and

ABX3 at 3.445 eV. The labeling of the acceptor bound excitons and donor bound excitons is based on two facts: (1) ABXs in GaN are expected to have higher binding energies then DBXs because of the depth in the gap[81, 88] and (2) the measured positions of the bound excitons under consideration of the strain state of the crystal fit well with observations of other groups in the literature.[72, 73, 89, 90] While the assignment of the observed transitions seems to be well established for the donor bound exciton region throughout literature, the acceptor bound excitons are more controversial and will need more argumentation. As part of this work, for the first time, three emission lines were observed in the acceptor bound exciton region as described above. In the following, the assignment of these three lines to excitons bound to neutral acceptors, as well as the identification of the according donor acceptor pairs as indicated in FIG. 7, will be discussed.

Low Mg doping leads to the appearance of an ABX1 and ABX2. For higher doping with concentrations above 1×10^{18} cm^{-3}, an increase of the ABX3 transition intensity is observed. Samples with even higher doping concentrations of 1×10^{19} cm^{-3} and 2×10^{19} cm^{-3} show an intense ABX2 transition, so that ABX1, 2 and 3 make up a broad ABX transition. In the low energy region of the spectra, DAP luminescence can be observed. A DAP transition is typical for Mg doped GaN and seems to be due to the compensation of the Mg acceptor, whereby its properties and exact assignments are not fully understood. The energetic position of the DAP has been reported in many publications at around 3.27 eV.[72, 79, 87, 91-93] Three different DAP transitions with according phonon replica (shifted ~92 meV from the zero phonon line) can be found in all spectra in FIG. 7. The observed transitions are identified as DAP1 at 3.287 eV, DAP2 at 3.275 eV and DAP3 at 3.256 eV. DAP1 and 2 are more prominent at low doping concentrations and DAP3 is more intense at higher doping above 5×10^{18} cm^{-3}. In chapter 3.1.2, it will be shown that annealing of GaN:Mg samples significantly changes the shape of the luminescence in the DAP transition region. The intensity of the DAP2 is, for example, strongly depending on the activation grade of the sample. The change in the DAP transition to an intense DAP3 is accompanied with an increase of ABX3 transition as it can be seen for Mg:1×10^{19} cm^{-3} to 2×10^{19} cm^{-3} and suggests a charge transfer from a shallow bound exciton like ABX1 to a deeply localized exciton like ABX3 with increasing doping.

For deeper analysis and understanding of the DAP- and BE-transitions, PLE measurements were performed on a sample doped with 8×10^{17} cm^{-3} Mg. This measurements will help to clarify the relation between the single BE transitions and the DAP luminescence as, well as identify the excitation channels of the DAP and binding energies of the BE. FIG. 8 (a) displays the PLE spectra from the DAP1 and DAP2 transition of the 8×10^{17} cm^{-3} Mg-doped GaN. For comparison and to support the identification of the excitation channels, a PL spectrum of a 8×10^{17} cm^{-3} Mg doped GaN sample is presented in FIG. 8 (b). Samples were selected due to the sharpest observable peaks and appearance of all relevant transitions in the spectra.
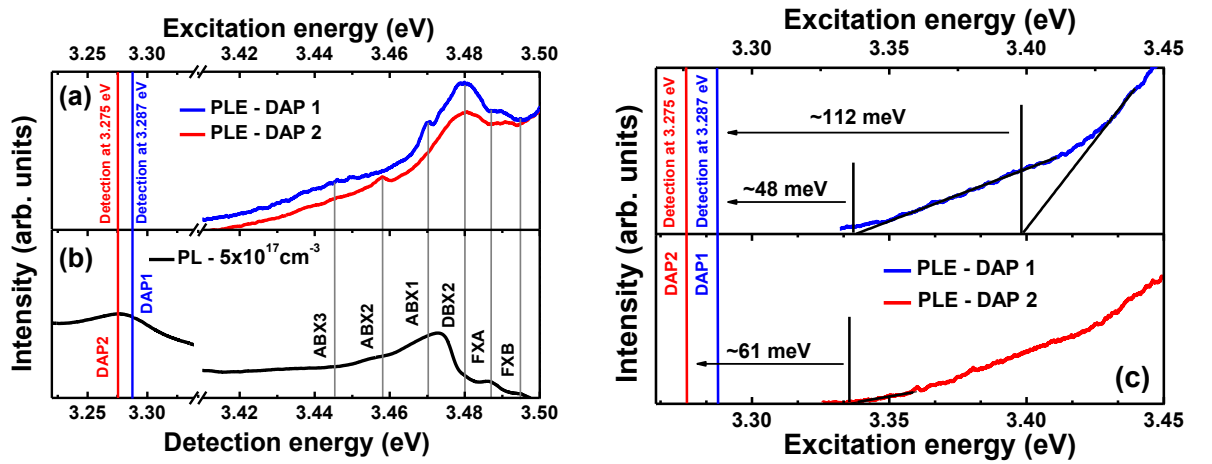
FIG. 8: [a] **(a) Low temperature (2 K) PLE of DAP1 at 3.287 eV and DAP2 at 3.275 eV of Mg-doped GaN with 8×10^{17}cm^{-3}. DAP1 has an excitation channel at the energy of the ABX3, while DAP2 has excitation channel at the energy of ABX2. (b) PL of Mg-doped GaN 5×10^{17}cm^{-3} for comparison with PLE. (c) PLE of DAP1 and DAP2 (zoom). Three different donors can be identified with binding energies 48±5, 61±5 and 118±5 meV**

FIG. 8 (a) shows the excitation spectra of the DAP1 at 3.287 eV and DAP2 at 3.275 eV. In the PL in FIG. 7 the two DAP transitions at ~3.27-3.28 eV and its replica are overlapping in most of the PL measurements so that no single lines could be identified. However, PLE allows resolving the two DAP transitions as there are clearly two different excitation spectra observable for the DAP1 and DAP2 transition. This overlapping and the lack of the possibility to identify the DAP1 and DAP2 in PL spectra may explain why slightly different positions are

---

[a] This PLE measurements were performed by Gordon Callsen at the TU-Berlin as part of a collaboration on GaN:Mg.

reported for the DAP transition in literature, as well as why some PL measurements do not clearly show the expected ~92 meV LO-phonon energy shift for the DAP phonon replica in GaN:Mg.[94, 95] Nevertheless, in samples with very low doping concentrations, Fisher *et al.* observed a phonon replica related peak with a separation of ~82 meV in PL which would indicate the existence of another peak shifting the position of the replica to a higher value as well.[90]

One of the most interesting results of the analysis of FIG. 8 (a) and (b) is the possibility to assign and identify different excitation channels of the DAP transitions. While the DAP1 transition clearly indicates a strong channel with ABX1, DAP2 indicates a strong channel with ABX2. In the region of the donor bound excitons both DAPs have a strong and intense excitation channel with DBX2. In addition, a very slight excitation channel with DBX3 can be found for both DAPs. These observations suggest that the DAPs have different excitation channels on the acceptor side (ABX1 or ABX2) while the dominant donor for all DAP transitions is the same (DBX2).

Using the PLE in FIG. 8 (c) and knowledge of the doping concentration of the sample (here Mg:8×10^{17} cm^{-3}), the donor (E_{bin}^D) and acceptor (E_{bin}^A) binding energies can be determined. The determination of binding energies is described by (1):[96, 97]

$$E_{DAP}(N_m) = E_{gap} - E_{bin}^D - E_{bin}^A + \alpha \sqrt[3]{N_m} \tag{1}$$

Thereby, the DAP position (E_{DAP}) is known from PL spectra and the bandgap energy can be determined from the free exciton positions of the FXA and the exciton binding energy of 25 ± 0.9meV for GaN.[43] At 2K the bandgap may be calculated to $E_{gap} = 3.512$ eV. The term $\alpha \sqrt[3]{N_m}$ in equation (1) describes the coulomb interaction, were α is a constant that was determined experimentally to $\alpha = 2.1 \pm 0.1 \times 10^{-8}$ eVcm[97, 98] and N_m is the majority carrier concentration in the crystal. Since at a doping level of Mg:8×10^{17} cm^{-3} the Mg is fully compensated by intrinsic donors, the value of N_m can be considered to be very small. In fact, because of the high contact resistance, the sample is considered having a free carrier concentration below the detection limit of Hall effect measurements at 1×10^{15} cm^{-3}. However, the value of 1×10^{15} cm^{-3}would result in a coulomb term much smaller than 5meV which is in

the range of the error of the determination of the exciton binding energies. Therefore, the coulomb term can be neglected in Equation (1) and the donor binding energies are determined from FIG. 8 (c) by extrapolation of the PLE signal of DAP1 and DAP2 to the baseline at zero luminescence intensity. Then, the binding energy of a donor is given by the difference of the interception of the PLE with the base line and the DAP position in the PL spectra. Three different interceptions with the base line are found in FIG. 8 (c). This leads to the identification of three different binding energies for the different involved donor bound excitons with E_{bin}^{DBX1} = 48 meV, E_{bin}^{DBX2} = 61 meV, and E_{bin}^{DBX3} = 118 meV. In addition to the determination of donor binding energies from PLE, temperature dependent photoluminescence measurements (TDPL) can be made to verify the findings. In FIG. 9 a TDPL measurement in the range from 5 - 125 K of a GaN:Mg sample with doping concentration around 8×10^{17} cm^{-3} is shown.
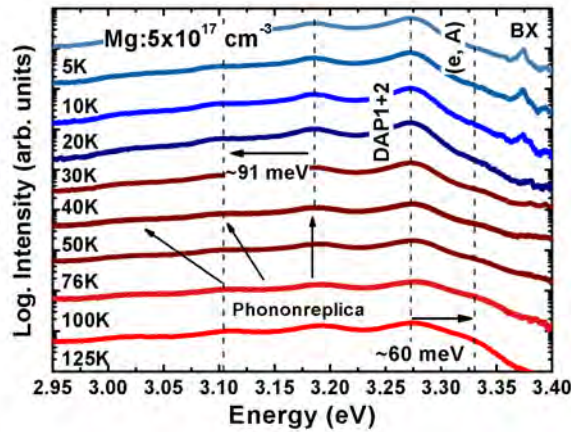
FIG. 9: Temperature dependent PL in the range from 5 – 125 K of the Mg:8x10^{17} cm^{-3} GaN sample. The DAP1 and DAP2 can been seen as well as their according phonon replica. At around 40K a band to acceptor transition (e, A) at 3.34 eV can be observed. This transition is 60 meV blue shifted to the DAP and in agreement with the observation of DBX2 in FIG. 8.

At 5 K the DAP1 and DAP2 as well as its according BX transitions are observed. The increase of the temperature from 5 K to 40 K leads to a slight decrease of the DAP intensity, the disappearance of the BX transitions as well as the appearance of a band to acceptor transition (e, A) at 3.335 eV.[97] The (e, A) transition is due to the thermalization of the corresponding donor bound exciton to the DAP transition, here DBX2. Therefore, a shift of ~60 meV to the DAP position can be observed. This proofs the feasibility of the

determination of DBX2 from PLE as the most prominent donor bound exciton involved in the DAP transitions.

After the determination of the binding energies of the donor bound excitons Equation (1) can be used to calculate the acceptor binding energies. The binding energy of ABX1 is determined as $E_{bin}^{ABX1} = 164$ meV and the binding energy of ABX2 is determined as $E_{bin}^{ABX2} = 176$ meV from equation (1) under consideration of the corresponding DAP1 and DAP2 peak positions. The binding energy of ABX3 can be determined from DAP3 resulting in a binding energy of $E_{bin}^{ABX3} = 195$ meV. The corresponding localization energies are found in the PL and PLE spectra by subtracting the ABX or DBX peak position from the free exciton position. Haynes rule describes a linear proportionality between the binding and localization energy of the bound excitons.[99] Thus, knowing the binding and localization energies of the donor and acceptor bound excitons, Haynes rule can be tested and the acceptor or donor behavior of the BX can be verified. The linear proportionality for the BX is presented in FIG. 10.
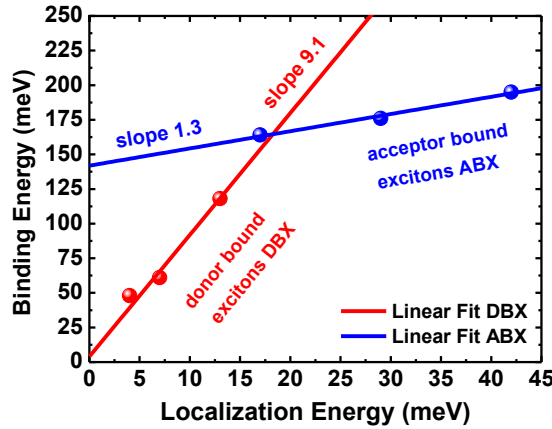
FIG. 10: Haynes rule: Plot of the binding energy and the localization energy for the ABX and DBX transition in GaN:Mg. A linear relation between the binding and localization energy can be found for the donor and acceptor bound excitons. By taking the slope from the linear fit, a proportionality constant for the donor bound excitons of 0.11 and 0.77 for the acceptor bound excitons can be determined.

For the donors and acceptors, a linear dependence of the binding energy as function of the localization energy is observed. Haynes rule is therefore suitable for the ABXs and DBXs and the slope of the linear fit can be used to calculate the proportionality constants. For the DBX the constant is 0.11 in FIG. 10. Compared with Meyer *et al.*[100] who determined a value of 0.2

by using TDPL for the Si and O donor bound excitons, this is a fair agreement. In the original work of Haynes *et al.*[99] a value of 0.12 was determined for donor bound excitons in silicon. This is in good agreement with the slope of the DBXs in FIG. 10, which is very interesting since the original work in silicon is considered to be representative for ideal effective mass like donors. This would indicate that DBX1, DBX2 and DBX3 are behaving like ideal effective mass like donors in GaN. Nevertheless, for the ABX we get a proportionality constant of 0.77. The two different slopes confirm the interpretation of the assignment of the bound excitons as ABX and DBX. Meyer *et al.*[100] have shown that the proportionality constant for donors and acceptors are supposed to be different.

The determined binding energies, localization energies and energetic positions of all optical features observed in FIG. 7 are listed in Table 2. The error for the binding energies in Table 2 is equal to the spectral line widths of ~ 5 meV in the PL ad PLE spectra and the error for the localization energies arises from the fitting of the peaks in the PL spectra.

Table 2: Bound exciton transitions and donor acceptor pair (DAP) transitions in GaN:Mg [a]

Name	E_{pos}(eV)	E_{loc}(meV)	E_{bin}(meV)	Origin / Description
FXB	3.495			Free B exciton
FXA	3.487			Free A exciton
DBX1	3.483	4±2	48±5	Neutral donor BX, V_N-related[54, 84, 85]
DBX2	3.480	7±2	61±5	Neutral donor BX, O[71, 101]
DBX3	3.474	13±2	118±5	Overlay of ionized (DBX2) & neutral DBX
ABX1	3.470	17±2	164±5	Neutral shallow Mg transient state[73]
ABX2	3.458	29±2	176±5	Transitional Mg BX[101-103] or unknown
ABX3	3.445	42±2	195±5	Neutral Mg deep ground state[73]
DAP1	3.287			DBX2 + ABX1 & ABX3
DAP2	3.275			DBX2 + ABX2 & ABX3
DAP3	3.256			DBX2 + ABX3

[a] Table published as part of collaborated work on p-type GaN with the TU-Berlin in Callsen et. al.[86]

Comparing the findings presented in Table 2 with values reported in literature for the binding energies of ABX1 and ABX3 a good agreement to the idea of an effective mass like shallow transient state (STS) of Mg_{Ga} ($E_{bin}^{STS} = 150 meV$) and a noneffective mass like neutral deep ground state (DGS) of Mg_{Ga} ($E_{bin}^{DGS} = 180 meV$), as theoretically predicted by Lany *et al.*[73], is found. This dual nature of the Mg acceptor in GaN was also suggested by Monemar *et al.*[72] and can be affirmed by our work.

It should be noted it is unlikely that an Mg-H complex is related to the ABX transitions, as proposed by other works.[79, 104, 105] This will be discussed in more detail in the next section (3.1.2). ABX2 in contrast to ABX1 and ABX3 cannot be clearly identified. It could be a transitional and partially lattice relaxed state of Mg_{Ga} between ABX1 and ABX3[101-103] or another unknown impurity. However, ABX2 is directly connected to the incorporation of Mg and there are not many other acceptors that are expected to be increasingly incorporated for increasing Mg concentration (see Chapter 3.1.3).

Results from PLE and TDPL analysis for the binding energy of the DBX2 with 60 meV suggest oxygen as the origin.[71, 101] This is a very interesting finding since all DAP transitions have shown an intense excitation channel with DBX2. The major donor connected to the DAP transitions, therefore, seems to be oxygen. This is a reasonable result since all Ga-polar samples grown with our MOCVD system have a $2–5 \times 10^{17}$ cm^{-3} background concentration of oxygen (SIMS in Sections 3.1.2 and 3.1.3). DBX1 may be identified as a V_N-related donor [71, 106, 107] and is a well-known as a native point defect incorporated into GaN along with Mg.[82] Finally, DBX3 is identified as an overlay of an ionized DBX2 transition and a neutral DBX.[86] Nevertheless, the connection of the Mg acceptor and O or V_N as donor to the DAP transitions is highly important for a better understanding of point defects in Mg doped GaN and will be relevant, especially when a point defect control scheme to reduce the number of donor type compensators of the Mg acceptors in GaN is applied (Chapter 3.3).

3.1.2 Activation of GaN:Mg: The hydrogen passivation

GaN:Mg samples grown with MOCVD show high resistivity values after the growth and need to be activated by a post growth annealing.[76, 80] Origin of the high resistivity is the formation of Mg-H complexes passivating the Mg acceptor.[74, 78, 79] The optical transitions of annealed and as-grown samples are not fully understood. Thus, using PL results presented in the previous Section (3.1.1), in combination with SIMS results of annealed and as-grown samples may help improve the understanding of point defects in GaN:Mg and their optical spectra.

In FIG. 11 PL spectra of a GaN:Mg sample with Mg concentrations of 2×10^{19} cm^{-3} are presented. It is demonstrated that the activation by dissociation of the Mg-H complex as a function of the annealing temperature can be monitored by the change of the according PL spectra. The sample pieces used for this annealing experiment originate from the same wafer.

Samples have a 700 nm thick Mg:2×10^{19} cm^{-3} doped GaN film to provide for low resistivity and high free carrier concentration when fully activated. This doping concentration is considered to deliver the highest available free hole concentration as it is not yet self-compensated (self-compensation limit). Further discussions about self-compensation will be discussed in Chapter 3.1.3.
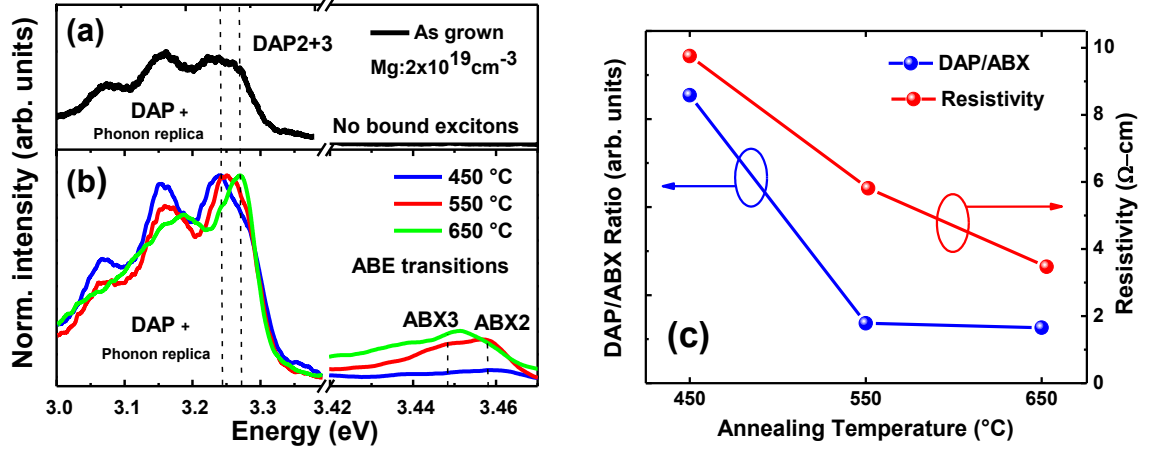
FIG. 11: Activation of Mg-doped GaN (2×10^{19}cm^{-3}) monitored by low temperature (3K) PL spectra. (a) PL of the as-grown sample with an intense and broad DAP and no bound exciton transitions. (b) PL of samples that have been annealed at different temperatures. An increase of the ABX intensity as function of annealing temperature can be observed. (c) Intensity ratio of DAP/ABX for samples annealed under different temperatures and the according resistivity of the samples.

In FIG. 11 (a) the PL spectrum of an as-grown sample piece is shown. The resistivity of the sample cannot be determined by Hall effect measurements since the contact resistance of as grown samples is too high. Nevertheless, the PL spectra reveal an intense DAP luminescence with two overlapping DAP maxima at 3.275 eV (DAP2) and 3.256 eV (DAP3). No near band edge luminescence, like bound exciton transitions, can be observed in that sample. After a post growth annealing the luminescence is changed as displayed in FIG. 11 (b). The presented samples have been annealed for 2 hours in a N$_2$ atmosphere at 450ºC, 550ºC and 650ºC. The 450ºC sample shows a spectrum similar to the as-grown sample with an overlay of the DAP2 and DAP3 luminescence. In addition, a weak ABX transition can be observed, which is a combination of the ABX2 and ABX3 transition. An increase of the annealing temperature lead to a slight shift of the overlapped DAP which originates from a decrease of the DAP3

intensity and a simultaneous increase of the DAP2 intensity. In addition, the intensity of the ABX transitions increases. For the sample annealed at 650ºC, the DAP is dominated by the DAP2 and a very intense ABX2 and ABX3 luminescence can be observed. The spectra in FIG. 11 are normalized to the most intense DAP for comparison of the DAP transitions to the ABX transitions, but in general a decrease of the DAP luminescence can be observed as function of annealing temperature; the DAP/ABX ratio decreases.

In order to visualize the temperature dependent electrical activation of the samples the Hall resistivity of the samples in comparison with the DAP/ABX, intensity ratio is plotted in FIG. 11 (c). The increase of the annealing temperature leads to a decrease of the Hall resistivity from 10 Ωcm at 450ºC to 3.5 Ωcm at 650ºC. At the same time a decrease of the DAP/ABX intensity ratio can be observed. This ratio is determined from PL as presented in FIG. 11 (b), using absolute intensity values of the DAP luminescence and the ABX luminescence. Thus, a decrease of the DAP/ABX ratio seems to go hand in hand with a decrease in resistivity. In other words, a more activated sample shows a more intense ABX transition as well as a decrease of the DAP3 transition intensity and a dominating DAP2 transition. It should be noted that from comprehensive annealing studies performed as a part of this work, samples annealed at 650ºC for 2 hours in N_2 can be considered as fully activated. The lowest resistivity values were measured only at this annealing condition. The increase of annealing temperature or time did not decrease the resistivity. Moreover, an increase of the resistivity was observed for higher annealing temperatures and times. The slightly higher resistivity values in FIG. 11 (c) in comparison to state-of-the-art values for fully activated samples (1-2 Ωcm) are due to the used indium contacts. Such low resistivity values can only be measured if Ni/Au-contacts are used. However, such contacts need annealing during metallization and would activate the samples and, therefore, distort the results of any activation study.

To confirm the passivation of GaN:Mg by hydrogen and to understand the formation of Mg-H complex, SIMS measurements were performed on the samples displayed in FIG. 11. Hydrogen, oxygen, carbon, magnesium and silicon (not shown in SIMS FIG. 12) atomic concentrations were investigated and results are presented in FIG. 12. In (a) the hydrogen atomic concentration as function of the annealing temperature is shown. A hydrogen

concentration with a maximum of 1.5×10^{19} cm^{-3} can be observed close to the surface for the 700 nm p-type layer in the as-grown sample. The hydrogen concentration decreases towards the undoped buffer layer grown underneath the p-type film. An annealing at 450ºC leads to a decrease of the hydrogen concentration to 6×10^{18} cm^{-3} which is about half of the concentration in the as-grown sample. For the sample annealed at 650ºC, a temperature which is expected to result in fully activated samples, a reduction of hydrogen to $\sim 2 \times 10^{18}$ cm^{-3} is observed. This is an order of magnitude lower than the hydrogen concentration in the as-grown sample.
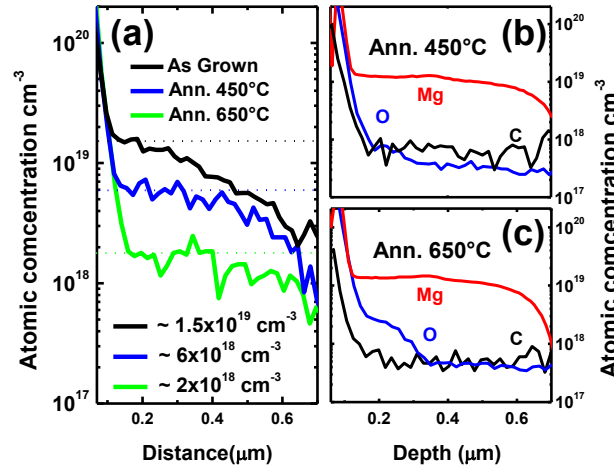
FIG. 12: (a) SIMS analysis of the hydrogen concentration in Mg:2×10^{19} cm^{-3} GaN. The hydrogen concentration decreases with the annealing temperature down to the detection limit for fully activated samples. (b) SIMS spectra for Mg, O and C after annealing at 450°C and (c) after annealing at 650°C. The amount of oxygen and carbon is in the expected background concentration for MOCVD grown Ga-polar GaN.

For comparison, the concentrations of Mg, O and C are displayed for the two annealed samples in FIG. 12 (b) and (c). According to these SIMS scans, the Mg concentration for the sample, as expected, similar in both pieces, and lies around 1.5×10^{19} cm^{-3} with a slight drop towards the undoped GaN buffer layer. This drop at the interface between doped and undoped layer is typically observed in GaN:Mg/GaN:nid. The reason for this drop is that Mg needs to reach a critical surface coverage before it is incorporated in a steady-state.[108, 109] Nevertheless, it is remarkable that the Mg curve in (b) and (c) fits excellent to the profile on hydrogen in the as-grown sample in (a). In addition, the annealing does not seem to have an effect of the

concentration of O and C. Just a slight increase of O can be observed at the surface of the sample caused O diffusion, in case of annealing at 650ºC. But, the overall bulk O concentration is not affected. However, the atomic concentrations of C and O species are around the expected background concentration due to the applied growth conditions and polarity.

Comparing FIG. 11 and FIG. 12 and the results from Section 3.1.1, an interesting conclusion can be made. First, the Mg concentration of annealed and not annealed GaN:Mg layers matches the hydrogen concentration of an as-grown sample suggesting the passivation of Mg by a Mg-H complex and the incorporation of the complex during growth as a whole; whenever a Mg atom is incorporated during growth also a hydrogen atom incorporated and both will form a complex.[108] While the resistivity decreases, the amount of carbon and oxygen are not affected by the annealing. Thus, no major compensation of Mg by those species is likely and the high resistivity in as-grown sample is due to the passivation by hydrogen. As demonstrated above, the PL does change significantly as function of the activation by annealing. For activated samples, strong ABX2 and ABX3 transitions but no intense ABX1 transition are observed. Therefore, it can be concluded that the conductivity is related to a transitional state of the Mg or the deep ground state (DGS) of Mg_{Ga}. The shallow Mg_{Ga} state seems not to be significant in highly doped and activated samples, because no significant optical transition can be found in such samples. For the DAP transitions, it is observed that the electrical activation is connected to a decrease of DAP3 and the presence of a stable and intense DAP2 emission. This also indicates that the electrical conductivity of the sample is connected with the deep ground state of Mg (ABX3). This fits well to the observed ionization energies of Mg in GaN of ~200 meV [81] and optical observations of Monemar *et al.*[72] The decrease of the DAP3 intensity can be explained by less compensation of ABX3 related acceptor or an increased compensation of the ABX2 related acceptor. A connection of the ABX transitions to Mg-H seems to be unlikely since the activation by annealing increases the ABX transition intensity and decreases the resistivity while at the same time SIMS analysis indicates an order of magnitude less H in the crystal. The results that the major donor connected to the DAP transitions seems to originate from the DBX2 which was identified as oxygen (Section 3.1.1) and also fits very well to the observations from the annealing

experiment. In all samples, a DAP emission can be measured, independent from the activation status of the sample. In SIMS stable oxygen background was observed in all samples. The changes in DAP transition spectral position and slight changes in intensity seems to be a result of a change in the acceptor state of the Mg and the presence of Mg acceptors by the dissociation of the Mg-H complex. The decrease of the DAP/ABX ratio in FIG. 11 is mainly a result of an increase of the ABX transitions, but not a decrease of the overall DAP intensity (however the dominating transition shifts from DAP3 to DAP2 as discussed above). This again suggests, that the Mg-H complex is not observed optically in the shown spectra. This observation rather suits a change in the concentration of passivated acceptors and thus, a change of the Mg state due to the dissociation of the Mg-H complex.

3.1.3 Self-compensation of GaN:Mg - V_N-related Defects at High Mg Doping

If GaN is heavily doped with Mg, high resistivity values can be measured even when the film has been annealed after the growth. Doping of Mg above $2-3 \times 10^{19}$ cm^{-3} leads to an increase of the resistivity of annealed samples[68] and at sufficient high doping in the 10^{20} cm^{-3} regime the material can even turn to be n-type conductive.[85] This observation is not part of the passivation by Mg-H since hydrogen is strongly reduced or even removed by the thermal annealing. Above Mg:2×10^{19} cm^{-3}, the self-compensation of Mg starts to reduce the conductivity of the material.[83] Self-compensation means that at a specific doping concentration the increase of dopants lead to a constant or decreased free-carrier concentration.[110-112] A saturation of the carrier concentration can be caused by an interstitial or amphoteric behavior of the dopant,[110] but a decrease of carriers needs a compensating defect of the opposite charge species. Self-compensation is in general understood as compensation of the dopant by intrinsic lattice defects.[110, 111] In GaN:Mg this intrinsic lattice defect causing the self-compensation is expected to be the nitrogen vacancy (V_N).[68, 83] However, the details of the self-compensation are not clear. A number of defects have been identified in the literature describing the self-compensation of GaN:Mg. The major suspects are: the pure triple charged V_N, a $(V_N-H)^{2+}$ complex,[113] a V_N-Mg complex[93] and O_N.[85] The oxygen compensation occurs at Mg:$>1 \times 10^{20}$ cm^{-3} and is due to the inversion of the Ga-polar GaN to N-polar GaN,[114] where two orders of magnitude higher O levels are observed.[85]

However, the self-compensation goes hand in hand with an increase of the resistivity of the film due to a decrease of the mobility and free-carrier concentration caused by the compensation of the dopant. In the following, Hall resistivity measurements are presented since an accurate carrier concentration measurement is limited by Hall setup (current source) and the non-ohmic contacts of compensated GaN:Mg (see Section 2.3). For a Mg doping series of Mg:$1x10^{19}$ cm^{-3}–$5x10^{19}$ cm^{-3} the self-compensation process will be described in FIG. 13. In (a), the resistivity of the samples are displayed as function of the Mg doping concentration. All presented samples have been fully activated by annealing (at 650ºC) to remove most of the hydrogen passivation of Mg (described in Section 3.1.2). Mg doping till $2x10^{19}$ cm^{-3} leads to a decrease of the resistivity and an increase of free carrier concentration. The doping regime below $2x10^{19}$ cm^{-3} is dominated by the hydrogen passivation, which can be removed by annealing. The lowest observable resistivity in our samples is ~1.5 Ω cm at Mg:$2x10^{19}$ cm^{-3} doping and corresponds to a free carrier concentration of ~$2x10^{17}$ cm^{-3}. This conductivity mainly determined by the ionization energy of Mg at room temperature. If the Mg doping concentration is increased and GaN is doped more than the self-compensation limit of $2x10^{19}$ cm^{-3} (critical doping concentration before self-compensation occurs), an increase of the resistivity is observed.[68, 108, 115] Therefore, the doping regime above $2x10^{19}$ cm^{-3} is named in FIG. 13 (a) as self-compensation regime. The increase of resistivity by an increase of doping concentration is also named overcompensation as it is connected with a significant increase of Mg compensating donors. Other issues like a Mg passivation or interstitial Mg would lead to a constant resistivity as function of doping. A donor-like point defect or complex dominating at that doping regime is the needed to explain this increase in resistivity. In order to highlight the influence of doping on the blue luminescence at 2.85 eV, the room temperature PL from 2.4-3.5 eV of the Mg doping series is presented in FIG. 13 (b). This blue luminescence typically observed in p-type GaN at room temperature at high doping concentrations. The samples $1x10^{19}$ cm^{-3} and $2x10^{19}$ cm^{-3} do not show blue luminescence and it has to be mentioned that no sample doped below $1x10^{19}$ cm^{-3} showed blue luminescence, as well.[71, 84] An increase of Mg doping above the self-compensation limit at $2x10^{19}$ cm^{-3} leads to the presence of the blue luminescence at 2.85 eV. It has to be noted that a yellow luminescence at 2.2 eV was also present in the PL of the samples at room temperature. This luminescence can be observed in all samples and is not significantly impacted by the Mg

doping concentration. In literature the yellow luminescence is widely investigated and expected to be connected to V_{Ga}[71] or more likely to C.[116] Since C is controlled by the growth condition (namely the supersaturation by the V/III-ratio) and its concentration is not expected to be affected by the Mg concentration, it will not be discussed further.[59]
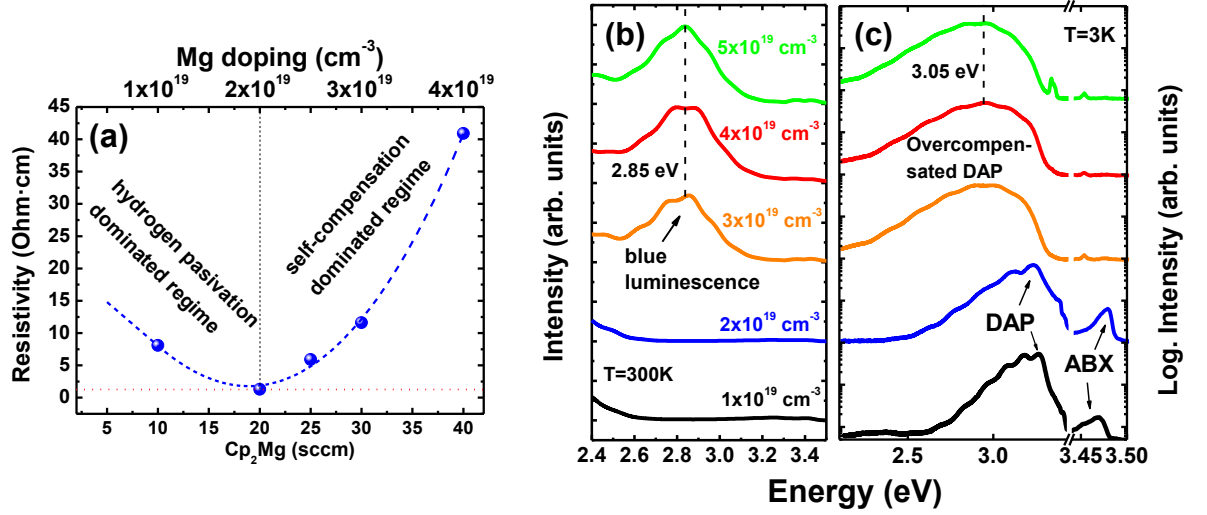
FIG. 13: Self-compensation of GaN:Mg: (a) Resistivity of GaN:Mg for high doping concentration. The resistivity of the annealed samples increases with Mg concentration for doping above $2 \times 10^{19} cm^{-3}$ (self-compensation of Mg). (b) Room temperature PL shows the increase of the blue luminescence at 2.85 eV in the self-compensation range. (c) PL at 3K of DAP and ABX transitions. Above Mg:$2 \times 10^{19} cm^{-3}$ doping a decrease of ABX transitions and an overcompensated DAP with its maximum at 3.05 eV can be observed.

The low temperature (3K) PL of the Mg doping series is presented in FIG. 13 (c) to investigate the impact of doping on the bound excitons and DAP transitions. At doping below 2×10^{19} cm^{-3}, a DAP transition at ~3.27 eV and the typical ABX transitions are observed. The DAP transitions are related to Mg acceptor states and O as a donor,[117] while the ABX transitions are related to neutral Mg states as discussed in section 3.1.2. DAP transitions are always observed, even in activated Mg doped GaN below and at the self-compensation limit, because of the oxygen background level of ~2×10^{17} cm$^-$ in the samples. ABX transitions are typically only observed for activated sample where the Mg-H complex is dissociated. An increase of the Mg doping concentration above the self-compensation limit leads to a significant decrease in intensity of the ABX transitions. In addition, the DAP shows a significant red shift and a broadening, while the resistivity of the samples increases. At

Mg:5×10^{19} cm^{-3} doping, the spectrum consists of a highly overcompensated DAP luminescence with a maximum at 3.05 eV.[71, 118, 119] The peak at 3.05 eV in the low temperature spectra is the same peak as that observed at 300K in FIG. 13 (b) around 2.85 eV (blue luminescence).[120] Thus, the lineshape of the overcompensated DAP transition in highly doped material is dominated by the underlying blue luminescence. This blue luminescence is directly associated with the self-compensation process, but its origin is still controversial. In literature, different peak positions for the overcompensated DAP are reported, but the typical peaks are originated in a range between 2.95 eV and 3.05 eV.[71] Deep donors, which compensated the Mg were discussed as a possible origin of the blue luminescence. Eckey *et al.*, for example, explained the 2.95 eV and 3.05 eV luminescence as deep donors at 240±30 meV and 350±30 meV and a shallow Mg acceptor at ~200 meV.[118] Kaufmann *et al.* identified the blue luminescence as a donor acceptor pair transition with Mg_{Ga} as acceptor and a V_N-Mg_{Ga} complex as donor.[68, 83, 84, 93] Other interpretations in the literature suggest $(V_N-H)^{+2}$ as reason for self-compensation.[121] This complex would be a deep donor which compensates two Mg acceptors. This was supported by Gelhausen *et al.* who proposed as well V_N-H and H-related complexes as being involved in the compensation of Mg.[79] However, most of the works agree with the picture of either V_N or V_N-related complexes as the origin of the self-compensation in Mg doped GaN and a relation of the blue luminescence to those vacancies as observed in room temperature PL or in the line shape of the low temperature DAP emission (FIG. 13).

A so-called GaN:Mg ladder structure was grown in order to determine the influence of annealing on the atomic concentrations of Mg, H, O and C and reach a deeper insight into the self-compensation mechanisms. This structure consisted of a 1.3 μm undoped GaN template followed by intercalated Mg-doped layers of 200-300 nm thickness with different Mg concentrations, each separated by undoped layers (200-300 nm). The sample was fully activated using annealing at 650°C. The structures were prepared in this manner for subsequent SIMS analysis. The SIMS analysis on the GaN:Mg ladder is presented in FIG. 14.
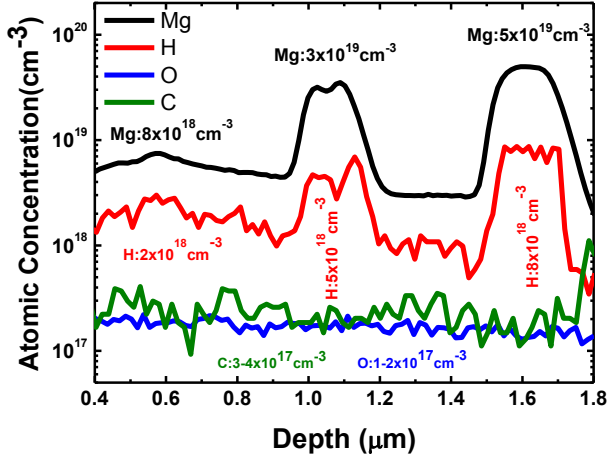
FIG. 14: SIMS analysis of a so called GaN:Mg ladder structure with three different doping concentrations of 8×10^{18}, 3×10^{19} and 5×10^{19} cm^{-3} (annealed at 650°C). Layers doped with Mg:3×10^{19} and 5×10^{19} cm^{-3} should not have significant hydrogen passivation since the H:5×10^{19} and 8×10^{19} cm^{-3} level is much lower than the Mg concentration. Oxygen and carbon are incorporated with amounts as low as 10^{18} cm^{-3} and therefore cannot be responsible for the self-compensation.

Three Mg doping levels have been used for the intercalated layers: 8×10^{18} cm^{-3}, 3×10^{19} cm^{-3} and 5×10^{19} cm^{-3}. The hydrogen level for the GaN sample doped with Mg:8×10^{18} cm^{-3} is after annealing at 650ºC around 2×10^{18} cm^{-3} which is the expected value for activated samples with doping below the self-compensation limit (section 3.1.2). For doping concentrations above the self-compensation limit of Mg:2×10^{19} cm^{-3}, the hydrogen concentration of not activated samples does not fit the Mg concentration (not shown). As a matter of fact, the hydrogen concentration in the samples never increased to a level above 2×10^{19} cm^{-3}. One could conclude that these samples are not fully passivated which would in turn lead to a low resistivity. However, this is contradictory to resistivity measurements presented above (FIG. 13). Therefore, since not enough hydrogen is available to passivate (or self-compensate) the Mg, it can be concluded that the simple Mg-H complex is not responsible for the self-compensation.[83, 108, 115] For annealed samples like the layer with Mg:3×10^{19} cm^{-3} doping layer as presented in FIG. 14, the hydrogen concentration is 5×10^{18} cm^{-3}. The Mg:5×10^{19} cm^{-3} layer reveals as well a high hydrogen concentration (8×10^{18} cm^{-3}). These hydrogen amounts are well above those of samples doped below the self-compensation limit that have been activated. As a matter of fact, the hydrogen concentration of samples doped above the self-compensation limit is not significantly changed by annealing.[108] This indicates that above the

self-compensation limit, a certain amount of H is stable against thermal annealing while at low Mg doping the amount of hydrogen has its equilibrium at $\sim 2 \times 10^{18}$ cm^{-3}, thus independent of the Mg doping concentration. In other words, above the self-compensation limit, hydrogen seems to form a new complex different to the usual Mg-H complex that can be dissociated by thermal annealing. Castiglia *et al*. proposed the existence of two different Mg-H complexes. First, a metastable complex, leading to Mg-acceptors after thermal annealing, and second, a complex which is stable against thermal activation and electrically inactive.[108] Although the formation of a metastable Mg-H complex seems to be very likely and appropriate enough to explain the residual hydrogen for highly doped samples, it should be mentioned that also V_N-H complexes could be stable against the annealing as well.[113, 115, 121]

As discussed above, the residual amount of hydrogen cannot be solely responsible for the self-compensation. In the 5×10^{19} cm^{-3} doped sample, the hydrogen amount is not even 20% of the Mg concentration and thus, cannot explain the low conductivity (the Mg-H is electrically neutral and does not provide for additional compensating charges – it only passivates). Even a $(V_N\text{-H})^{2+}$ complex could compensate just little more than 30% of the amount of Mg doping. The measured hydrogen concentration in the highly doped samples is therefore a way to explain the self-compensation. Hydrogen plays a minor or no role at all for self-compensation in p-type GaN. Thus, other defects like the V_N-Mg complex or the triply charged V_N are more likely responsible for the self-compensation in GaN:Mg.

In addition to the hydrogen level, the carbon and oxygen concentration is shown in FIG. 14. Carbon can be observed with concentrations $\sim 4 \times 10^{17}$ cm^{-3} in all layers and is not affected by the Mg doping. The comparable high C concentration is related to the applied growth conditions and in general could be reduced by the growth with an adjusted supersaturation.[59] The oxygen concentration is also constant for all Mg doped GaN layers at $\sim 2 \times 10^{17}$ cm^{-3}. This amount corresponds to the typical background oxygen concentration typically observed in Ga-polar GaN samples grown with the used MOCVD reactor and have been annealed. The Mg doping does not affect these concentration even at Mg:5×10^{19} cm^{-3} and inversion domains are not significantly expected to be present till Mg:1×10^{20} cm^{-3},[85] to increase the background oxygen concentration. Due to the comparable low incorporation levels of C and O, both species cannot be held responsible for the self-compensation.

In addition to the investigation of the compensation with PL and SIMS, the influence of the Mg doping on the strain is investigated. Raman spectra of an undoped and Mg doped GaN samples were measured in $z(xx)\underline{z}$ configuration, to observe the occurrence of the E_2(high) Raman mode.[122] The position of the non-polar E_2(high) mode is mainly influenced by the strain state of the GaN film. Thus, the determination of the position of the E_2(high) is useful to measure the strain state of the film. In addition, the Full width at half maximum (FWHM) of the mode can be used to reveal defect incorporation in the film, since defect incorporation leads to a broadening of the E_2(high). The Raman analysis of the E_2(high) peak position and the FWHM of the mode is presented in FIG. 15 on GaN:Mg samples with varying doping concentration.
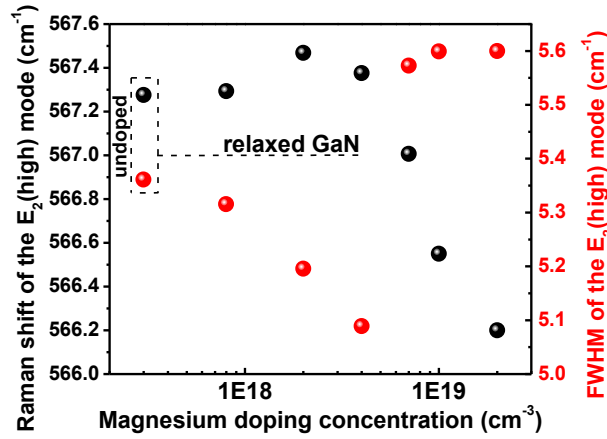
FIG. 15: Position and the FWHM of the GaN E2(high) Raman mode depending on the doping for concentrations ranging from Mg:5×10^{17} cm^{-3} to 2×10^{19} cm^{-3}. For comparison results from an undoped sample are shown. The Raman spectra were recorded at 300K.

The relaxed position of the E_2(high) at 567 cm^{-1} is marked in FIG. 15 in agreement with literature.[77,123] For the undoped GaN sample, the position of the E_2(high) peak indicates a slight compressive strain of the film due to the lattice mismatch of the GaN layer to the c-sapphire substrate.[123] A high doping till 4×10^{18} cm^{-3} leads to slight increase of the compressive strain. For further increased Mg doping of above 4×10^{18} cm^{-3}, a decrease of the compressive strain can be found. Finally, above 1×10^{19} cm^{-3} Mg doping, a tensile strain can be observed. Simultaneously, the FWHM of the E_2(high) mode decreases till Mg:4×10^{18} cm^{-3} and suddenly increases for doping above Mg:4×10^{18} cm^{-3}. This observation indicates a change

in defect incorporation in the sample at Mg doping concentrations around $1x10^{19}$ $cm^{-3}$and suggests that defect incorporation triggers the strain state from compressive to tensile strain. Since Mg has a larger ionic radius as compared to Ga, an increasing compressive strain for higher Mg-concentrations is expected.[124] However, if any other defect is incorporated parallel to Mg, additional tensile or compressive strain can occur. For doping below Mg:$4x10^{18}$ cm^{-3} the E_2(high) mode shifts to higher energies, the strain becomes more compressive. This can be fully explained with incorporation of Mg on Ga-lattice site. Above Mg:$4x10^{18}$ cm^{-3} the compressive strain decreases towards tensile strain suggesting the incorporation of an additional defect, possibly the nitrogen vacancy. The observations of an increased FWHM of the E_2(high) mode supports this suggestion. Responsibility of hydrogen for the change of the strain state is unlikely, since all samples have been fully activated by post growth annealing and no significant incorporation of hydrogen could be found in SIMS as depicted in FIG. 14. Also C and O incorporation did not change upon increased doping concentration. Nitrogen vacancies on the other hand are expected to lead to tensile strain. The change of the strain state of the Mg doped GaN film with a doping concentration above Mg:$4x10^{18}$ cm^{-3} may, therefore, be a fingerprint of the beginning self-compensation by V_N-related defects.

Using the results from luminescence, SIMS and Raman measurements as presented above, it is concluded that nitrogen vacancies are most likely responsible for the self-compensation in GaN:Mg with magnesium concentrations above $2x10^{19}$ cm^{-1}. Hydrogen was the only species that changed in incorporation in GaN:Mg with doping concentration as observed by SIMS (FIG. 14). Probably incorporated in an Mg or V_N related metastable complex, H is not expected to cause the observed self-compensation.[83, 108] First, its amount is just too small to lead to such high resistivity values as observed in FIG. 13. It was estimated that it could only contribute to 20 – 30% of the overall compensation. And second, the change of the strain state upon increasing doping could not be understood as hydrogen is expected to be incorporated as a complex and should consequently lead to compressive strain. Other notable impurities observed in the layer were oxygen, carbon and silicon (whereby the latter was not discussed but results are in general similar to those of carbon). However, the concentration of all of these impurities did not change with Mg doping concentration and their incorporation level was within normal and expected ranges.

On the other hand, a blue luminescence was observed in all samples with Mg doping above 2×10^{19} cm^{-1} (FIG. 13), and the intensity of this blue luminescence strongly increased with Mg doping. As discussed, the blue luminescence is widely associated with nitrogen vacancies throughout literature, either as a complex or isolated defect.[68, 83, 84, 93] The increased incorporation of nitrogen vacancies could also explain the change of the strain state as observed by Raman spectroscopy. A single isolated nitrogen vacancy would act as a triple donor leading to highly compensated or even n-type material.[83] Finally, theoretical calculation showed that the formation energy of the nitrogen vacancy is strongly decreased for p-type material making an incorporation of more V_N very likely for high Mg concentration.[82] Thus it is proposed that the incorporation of nitrogen vacancies is the main cause for self-compensation in highly Mg doped samples. This finding will be further confirmed throughout the next sections. Furthermore, it can be concluded that a control of the incorporation of nitrogen vacancies may be the key to generate better p-conductivity in GaN, an approach that will be discussed in the next section under the key words Fermi-level point defect control.

3.2   Fermi-level Management Using Above Bandgap Illumination

Point defects, either native defects like V_N, or impurities like Mg_{Ga} or their complexes like Mg-H, determine the electrical conductivity of GaN:Mg. Therefore, controlling the formation or incorporation of point defects during growth is essential. The incorporation is connected to the Fermi-level effect and will be discussed first in Section 3.2.1.

Next, the effect of above bandgap illumination will be presented in Section 3.2.2. The basics of the theoretical framework will be discussed very shortly to justify the effect of UV-illumination during the growth on the incorporation of point defects. For a detailed theoretical framework of Fermi-level management, the reader is referred to the dissertation of James Tweedie.[13] The present work can be understood as the experimental counterpart and proof of the theoretical framework from Dr. Tweedie. The experimental analysis of above bandgap illumination on the GaN:Mg model system will be presented in the chapter "Point Defect Control in GaN:Mg" (Section 3.3).

3.2.1   The Fermi-level Effect and the Formation Energy of Point Defects

In general, the energy of formation of a point defect (E^f) is a function of the Fermi energy, or the electronic chemical potential. In terms of the Fermi energy the energy of formation of a charged point defect with charged state q (0, 1, -1, 2, -2,...) can be expressed as (2):[13, 82]

$$E^f(x^q) = E_{ref}(x^q) - \sum_i n_i \mu_i + q(E_F - E_V) \tag{2}$$

x^q is here defined as the defect concentration. $E_{ref}(x^q)$ is the reference free energy of the crystal and depends on intrinsic properties of the crystal. The index (i) indicates a species of atom added or removed by introduction of the defect. μ is the chemical potential of an atoms and n is number of such atoms. The term $\sum_i n_i \mu_i + q(E_F - E_V)$ in (2) represents the electrochemical potential, described by the Gibbs energy at a given temperature, pressure and electrical potential. $q(E_F - E_V)$ represents the electron exchange energy and is equal to the formation energy of a single charge carrier multiplied by q. The sum in (2) depends not only

on the nature of the point defect, but also on the chemical potentials of the species involved and can be influenced by the growth conditions.

The dependence of the formation energy of a charged defect on the Fermi-level position is called in the literature Fermi-level effect.[125-128] This relation can be theoretically calculated using density functional theory (DFT). Doping of a semiconductor directly affects the position of the Fermi-level. A change of the formation energy of charged defects is triggered by the doping concentration. The relation between formation energy E^f of a charged defect and its concentration x^q is described by (3):

$$[x^q] = N_i \cdot exp^{\frac{-E^f(x^q)}{k_BT}} \tag{3}$$

Equation (3) is defined for the case of thermal equilibrium and k_B is the Boltzmann constant and T is the temperature of the crystal. N_i is here the product of the number of sites and the number of configurations in which the defect may be incorporated.
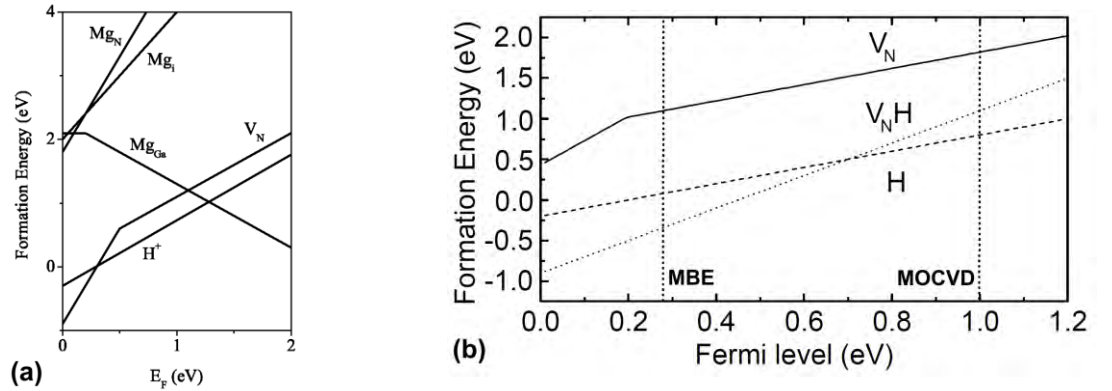
FIG. 16: (a) Formation energy of typical point defects in GaN:Mg as a function of the Fermi-level as calculated by DFT. Formation energies of Mg-related point defects and the compensators V_N and H (donors). *Picture taken from Van de Walle et al.[82]* **(b) Formation energies of the donors H, V_N and V_N-H complex.** *Picture taken from Alves et al.[113]*

However, the concentration of charged point defects is related to the doping concentration of the crystal. Two different calculations of formation energies of typical points defects in GaN:Mg calculated with DFT are shown in FIG. 16, to visualize the incorporation of charged defects as function of the doping concentration. The pictures are taken from the works of Van

de Walle *et al.*[82] and Alves *et al.*[113] and are used to explain the compensation of Mg acceptors in GaN by low formation energies of charged point defects close to the valence band.

As it can be seen in FIG. 16 (a) and (b), the formation energy of the intrinsic and extrinsic donors V_N, H and V_N-H is decreased towards the valence band (0 eV). P-type doping shifts the Fermi-level towards the valence band and leads to an increased incorporation of extrinsic and intrinsic point defects. This results, depending on the amount of Mg doping, in either hydrogen passivation by Mg-H complexes or the self-compensation of Mg by V_N-related defects as discussed in the previous Section 3.1. In addition to the incorporation of compensating defects, the formation energy of the Mg_{Ga} acceptor also depends on the position of the Fermi-level. Close to the valence band, the slope of the curve Mg_{Ga} is flat. This can be explained by the fact that the neutral Mg^0 acceptor that has lower formation energy than the ionized Mg^- acceptor at any given Fermi-level. It could also be a sign that at high doping concentration Mg is incorporated in the form of a complex. A change in Fermi-level will therefore not change the overall Mg concentration in the crystal. Nevertheless, if the Fermi-level is moved towards the middle of the bandgap, less incorporation of donor type point defects is expected, which would result in less compensated Mg acceptors.

3.2.2   The Steady State Formation Energy: UV illumination During the Growth

In order to directly control the charged point defect concentrations in a semiconductor, a non-equilibrium process scheme can be proposed in which the quasi-Fermi level for each particular charge reservoir is raised by an external excitation in this steady-state condition. For the proposed steady state condition $np = n_i^2$ no longer holds true. In this case, there is not a single Fermi-level that describes the populations of the free holes and electrons as it was described in the previous paragraph (Section 3.2.1). By exposing the material to UV-illumination (above bandgap illumination) during growth, a non-equilibrium process is created which is based on the continuous generation of charge carriers. This generates the demand of extension of the analogy between Fermi-level and the electrochemical potential. The electrochemical potential of charged defects in a semiconductor with steady-state populations of free charge carriers have to be expressed in terms of the quasi-Fermi levels.

Thus, for the UV-illumination during the growth, a new definition of the formation energy in (2) has to be found in terms of a charge balance at steady state. The steady state of the electron exchange energy $q\varphi$ is defined with reference to the valence band maximum by (4):[13]

$$q\varphi = \frac{q}{2}(F_n - F_p)$$ (4)

F_n and F_p are the quasi Fermi-levels for electrons and holes. A definition of quasi Fermi-levels can be found in Gerischer.[129] The formation energy from (2) has to be rewritten in the case of steady state formation energy E_{ss}^f of a charged defect in the charge state q and can be expressed in general to (5):[13]

$$E_{ss}^f(x^q) = \left[E_{ref}^f(x^0) - q(E_{ion} - E_V)\right] + \frac{1}{2}\left[q(F_n - E_V) + q(F_p - E_V)\right]$$ (5)

The first term in (5) describes the reference free energy $E_{ref}^f(x^0)$ of the bulk crystal in the neutral state of the crystal and the chemical potential. E_{ion} is the ionization energy and E_V is referring to the valence band maximum. The first term is not affected by the UV-illumination. The change of the formation energy at a steady state is therefore determined by the change of the quasi Fermi-levels in the second term in (5) (red marked).

In addition, the change of the formation energy ΔE^f affected by the illumination can be defined since the first term of (5) is not affected by the illumination, where the steady state quasi Fermi-level of the majority carrier is approximately equal to the equilibrium Fermi-level. It is important to note that the formalism in this section is written such that the majority charge carriers are a product and the minority carriers are a reactant. The change of formation energy of the dopant $\Delta E_d^f(x^q)$ is defined in equation (6) and the change of the formation energy for the compensating defect of the dopant $\Delta E_c^f(c^r)$ is presented in equation (7):[13]

$$\Delta E_d^f(x^q) = -\frac{q}{2}(F_n - F_p)$$ (6)

$$\Delta E_c^f(c^r) = -\frac{q}{2}(F_p - F_n) \tag{7}$$

c^r is the concentration of compensators in the crystal to the concentration of x^q of the dopant. In both equations the quasi Fermi-level of electrons F_n are always larger than the quasi Fermi-level of holes F_p. But the sign for the electron and hole quasi Fermi-levels are flipped. As a result, a negative formation energy change is always found for the dopant in Equation (6). For a compensator the formation energy change gives always a positive value in Equation (7). Thus, the steady state process is always changing the formation energy of a charged defect. In other words, the incorporation of the dopant has to be increased while the incorporation of the compensating defects is been decreased. This is a very effective point defect control scheme.

The following additional results can be concluded from the theory developed in the dissertation of James Tweedie:[13]

- Photo-generated minority and majority carriers create separate quasi Fermi-energies. The majority carrier concentration will not be significantly increased by the photo-generation. In contrast, the effect is significant for the minority carriers since the intrinsic minority carrier concentration is orders of magnitude lower than the concentration of photo-generated carriers.

- The small change of minority carrier concentrations is far enough. Therefore, relatively low power illumination is sufficient to change formation energies of charged defects.

- The observed change in incorporation is not due to a change in the growth conditions like temperature or V/III-ratio. The power of the UV-illumination source is simply not high enough to affect the growth conditions in any way.

- UV penetrates only ~100 nm, but carrier diffusion resulting from p-n junction affects the formation energy through the thickness of the doped layer (~700 nm). The profile of the defect formation energy follows the quasi-Fermi level.

As reference for the last statement, the calculated quasi-Fermi levels are shown in case of p-type GaN that is illuminated with an UV-lamp as mentioned in Section 2.1 (such a lamp can be attached to the MOCVD reactor). In FIG. 17 (a), the Fermi-levels are calculated for an annealing temperature of 550ºC and in (b) for the growth temperature of ~1050ºC.
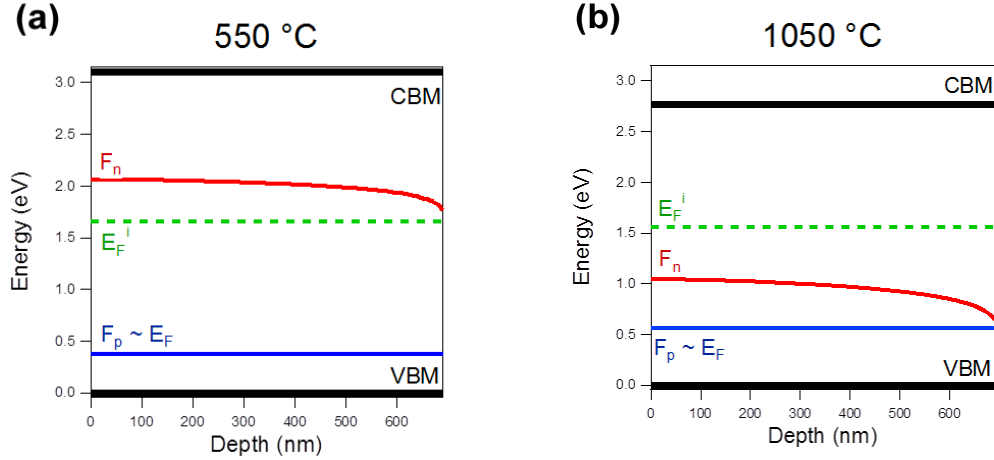
FIG. 17: Energy band diagram of p-type GaN under above-bandgap illumination. (b) at annealing temperature of 550ºC. (a) at typical growth temperature around 1050ºC. *Pictures taken from Dissertation of James Tweedie.*[13]

In the following sections, GaN:Mg will be used as a model system for point defect control by UV-illumination. The major assumptions that can be made for Mg-doped GaN from the theoretical modeling in the dissertation of James Tweedie are:[13]

- If the Fermi-level is increased in the Mg-doped GaN system, then the formation energy of Mg_{Ga}, an acceptor, decreases, while the formation energy of donors such as H, O and V_N increases.

- In case of n-type material, like low-doped GaN:Mg (here the oxygen impurity still dominates the electrical properties and makes it n-type) the formation energy of the acceptors increases (Mg_{Ga}), while the formation energy of donors (O, V_N) decreases.

3.3   Point Defect Control in GaN:Mg

After detailed investigations on compensating defects in GaN:Mg and the presentation of the theoretical background of above bandgap illumination as example for a Fermi-level management, the experimental proof of the theoretical concepts will be presented in the following chapter. GaN:Mg is used as a model system for the point defect control scheme where a change in the quasi-Fermi levels is expected to lead to change in the formation energy of charged defects. As discussed in the previous sections, a broad variety of point defects which affect the electrical conductivity can be found in GaN:Mg (passivation and self-compensation). A reduction of the amount of point defects during the growth by the applications of novel methods is strongly desired to improve the properties of existing GaN-based devices. Specifically, the following goals related to Mg doping in GaN are sought after: reduction of the Mg passivation by reducing the incorporation of hydrogen as a charged defect, and reduction of the Mg compensation by reducing V_N and its complexes. If these goals could be achieved, no post-growth activation would be needed which would simplify device fabrication and higher hole concentrations could be achieved as the self-compensation is reduced. In order to separate between these two effects, the influence of the point defect control by above bandgap illumination is presented separately. First, a reduction of hydrogen incorporation and thus, the passivation by Mg-H complexes at doping concentrations below the self-compensation limit are presented. Secondly, for samples grown with Mg concentrations in the range where the self-compensation applies, the influence of UV light on the formation of V_N and its complexes is investigated. In addition, the influence of UV-illumination on low-doped GaN:Mg is presented. In those samples the oxygen donor is the dominating species and Mg is the "unwanted" dopant (compensator), therefore, this system can be used to show the applicability of the concept on n-type material. From these results it can be concluded that the presented point defect control scheme using above bandgap illumination is feasible to control point defects in p-type and n-type semiconductors independent on the species of the dopant.

3.3.1 Point Defect Control of Hydrogen During Annealing

The effect of UV-illumination as a Fermi-level management scheme will be discussed with regards to the influence of UV-light during the post growth annealing. This is the first experimental demonstration of the application of the theoretical framework on the influence of UV-illumination on the annealing of Mg-doped GaN as discussed above (Section 3.2) and in the dissertation of J. Tweedie (Chapter 5).[13]

As discussed in Chapter 3.1.2, Mg-doped GaN is passivated by Mg-H complexes but a post growth annealing in a furnace leads to the dissociation of the Mg-H complex and the removal of the H. These annealing conditions determine if the sample is fully or only partially activated. The best annealing condition to dissociate the Mg-H complex and to fully activate the GaN:Mg was found to be annealing at 650ºC under N_2-atmosphere for 2 hours (Section 3.1.2).[56, 130]
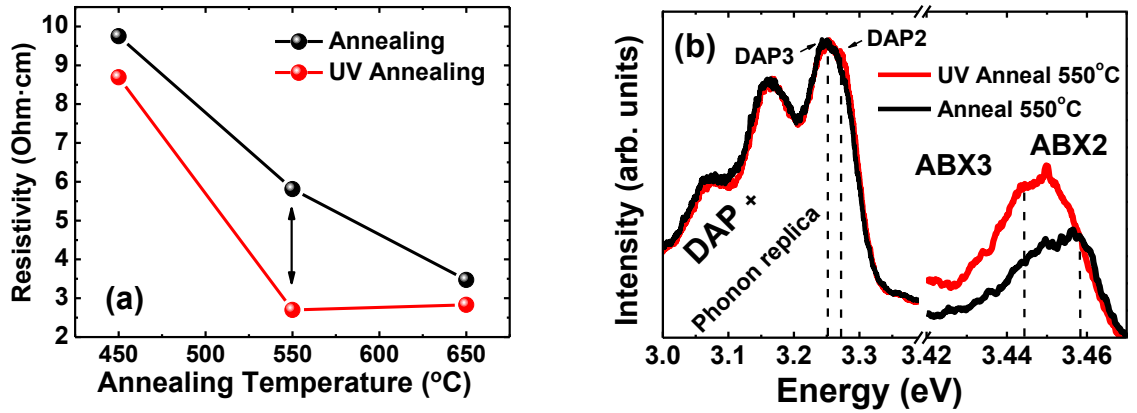
FIG. 18: Activation of Mg:2×10^{19} cm^{-3} doped GaN. (a) Resistivity measurement. (b) PL of sample annealed with and without UV. UV annealing leads to more intense ABX transitions.

FIG. 18 shows the resistivity and PL signal GaN doped with Mg:2×10^{19} cm^{-3} as a function of the applied annealing temperature. Both PL and resistivity can be understood as a measure for activation in the samples. Indium contacts were used for the Hall resistivity measurements (discussed in Section 2.3). In (a), the resistivity of samples are displayed that were annealed with and without UV-illumination under the conditions mentioned above. Independent of illumination, the resistivity of the samples decreases with increasing annealing temperature. However, a reduced overall resistivity of samples that were annealed with UV-illumination

can be found. Annealing of a sample at 550ºC, which is not considered an optimal temperature, but applying UV-illumination leads to a full activation similar to annealing at 650ºC. Thus, an enhanced dissociation of the Mg-H complex due the UV-illumination is suggested. In order to support the resistivity analysis, a PL analysis of the two annealed samples at 550ºC is presented in (b). Typical DAP transitions and their phonon replica, as well as a strong ABX, can be found. As discussed in Chapter 3.1.2, the activation of p-type GaN at $2x10^{19}$ cm^{-3} leads to an increase of the DAP2 transition at 3.275 eV and a decrease of DAP3 at 3.256 eV. For the DAP transitions, the spectrum of the UV-annealed sample in (b) suggests a slight increase of the DAP2. More obvious is the effect of UV-illumination during the annealing on transitions in the ABX region. The activated sample shows a strong ABX transition consisting of an ABX2 and ABX3. In Chapter 3.1.2, the fully activated samples annealed at 650ºC with significant decrease in hydrogen concentration revealed a dominating ABX3 transition which was in combination with the DAP/ ABX ratio ultimately recognized as a measure for the dissociation of the Mg-H complex. In comparison to the non-UV annealed sample, the UV-annealed sample shows the same behavior: a more intense ABX3 and a more overall strength of ABX transitions. This finding is consistent the observation in FIG. 18 (a).

Therefore, it is concluded that UV-illumination enhances the dissociation of the Mg-H complex under non-optimal annealing conditions (550°C); lower annealing temperatures are sufficient to lead to fully activated GaN:Mg.[105, 130] This finding is very promising as it demonstrates a first glimpse on the abilities of the proposed Fermi-level control scheme. In the next section, the above bandgap illumination will be applied during growth and an even more intense effect will be found which could make any post growth annealing obsolete in the future.

3.3.2   Point Defect Control of Hydrogen During the Growth

After presenting the applicability of above bandgap illumination as a Fermi-level point defect control scheme on the activation of Mg-doped GaN, its influence on the hydrogen incorporation during the growth will be discussed. This will be discussed separately from the influence of UV-growth on the self-compensation.

Hydrogen is present in the growth of GaN:Mg throughout the whole process as a product of the dissociation of NH_3, TEG and Cp_2Mg. Hydrogen is easily incorporated in GaN. As discussed throughout this work, hydrogen is typically incorporated in p-type GaN as a Mg-H complex. It passivates or compensates the material and may therefore be understood as a donor. Following the Fermi-level control scheme presented in Section 3.2, the incorporation of H should be suppressed if above bandgap illumination is provided during the growth. This important proposal will be tested experimentally in this chapter.

Table 3 shows the resistivity (which can be understood as a measure for the activation) of GaN samples doped with Mg ranging from $1x10^{19}$ cm^{-3} to $4x10^{19}$ cm^{-3} with and without illumination during the growth as determined by Hall effect measurements. This doping range was chosen because it suggests high hydrogen passivation of Mg and is around the self-compensation limit of Mg in GaN at $2x10^{19}cm^{-3}$ as discussed in Chapter 3.1.3. In addition, in order to allow a comprehensive comparison, some samples grown without UV illumination underwent an additional post growth annealing process. Samples that are as-grown (not annealed) are displayed in Table 3 (a) and the resistivity of post-growth annealed samples is displayed in (b). As demonstrated with PL and Hall effect measurements in Chapter 3.1.2, as-grown samples that were not subsequently annealed have a high resistivity, which is expected to be caused by the formation of the Mg-H complexes (not shown in Table 3). Samples grown under UV illumination have a low resistivity even when they have not been activated in a furnace after the growth. Their resistivity is comparable with the resistivity of non UV-grown samples in that have been activated by annealing (Table 3 (b)). Due to self-compensation, it is expected that samples with Mg concentration around $2x10^{19}$ cm^{-3} have the lowest resistivity values, a trend that can also be observed for UV-grown samples. This suggests that the UV-illumination during the growth is reducing the incorporation of hydrogen, especially for the Mg doping concentration of $1x10^{19}$ cm^{-3} and $2x10^{19}$ cm^{-3}, a doping range where the major reason of the high resistivity of as-grown samples is the formation of the Mg-H complex. The

small difference in the resistivity between the UV-grown and annealed non UV-grown samples are understood to arise from the different electrical contacts used for the resistivity measurements, like described in 0. For UV-grown samples and non UV-grown samples in column (a), indium contacts were used which allow only ohmic contacts of minor quality. In contrast, the, Ni/Au-contacts were used on the annealed samples in column (b). Ni/Au-contacts, if applied to non-annealed GaN:Mg would activate the samples due to the high temperature of the metallization process and would make the experiment, therefore, worthless. In Table 3, for non-annealed, non UV-grown samples with Mg doping levels of 3×10^{19} cm^{-3} and 4×10^{19} cm^{-3}, a lower resistivity is measured in comparison to samples with lower doping concentrations. Although these samples were not activated, they are not highly resistive. The lower resistivity is a result of lower hydrogen incorporation and, therefore, less passivation of Mg.[108] This is in agreement with the observations that are discussed in Chapter 3.1.2 and 3.1.3 and suggests that the self-compensation due to V_N-related point defects (not Mg-H complexes) takes place in this doping regime. Further discussion on the effect of UV-growth on the V_N-related point defects, including the resistivity measurements of UV-grown samples with Ni/Au-contacts, will be discussed in Section (3.3.3).

Table 3: Hall resistivity of GaN:Mg samples grown with and without UV-light illumination: (a) As-grown, no annealing using In-contacts (b) After post growth annealing in a N$_2$-atmosphere for 2 hours using Ni/Au-contacts.

Mg doping con-centration (cm^{-3})	(a) Resistivity (Ω cm)		(b) Resistivity (Ω cm)
	non UV-growth	UV-growth	non UV-growth
1×10^{19} cm-3	highly resistive[a]	11±1	9±1
2×10^{19} cm-3	highly resistive[a]	3±1	1.5±1
3×10^{19} cm-3	35±2	16±1	12±1
4×10^{19} cm-3	42±4	27±3	38±1

[a] Limited by the measurement system caused by very high resistance.

To clarify the results of resistivity measurements, additional PL measurements were performed on UV-grown and as-grown samples. In FIG. 19, the PL at 3K of two Mg:2×10^{19} cm^{-3} samples is presented. One sample (red) has been grown with UV illumination; the other sample (black) is an as-grown sample. Neither samples have been activated with a post-

growth annealing. A significant difference in the PL spectra between both samples can be observed. The spectrum of the as-grown sample shows the typical DAP transitions with an overlap of DAP2 and DAP3 and no observable ABX transitions. A more intense DAP3 overlap leads to a broadening of the whole DAP transition. The more intense DAP3 in the as-grown sample and the relation to the ABX transitions was presented in the previous Chapters 3.1.1 and 3.1.2. As-grown samples that are passivated by the Mg-H complex have typically an intense DAP3 transition and no ABX transitions in the PL. In contrast, the spectrum of the UV-grown sample shows ABX transitions and a DAP2 peak. The DAP3 is reduced by the UV-growth similar to the observations on activated Mg:$2x10^{19}$ cm^{-3} samples in Section 3.1.2. In addition, an intense ABX3 and slightly less intense ABX2 can be found. This suggests the presence of the deep ground state of Mg, as part of activated highly doped GaN:Mg. These observations for the UV-grown sample in FIG. 19 suggest the same activation grade as activation would achieve by post growth annealing in a furnace. The observations from Hall resistivity are therefore consistent with the PL result.
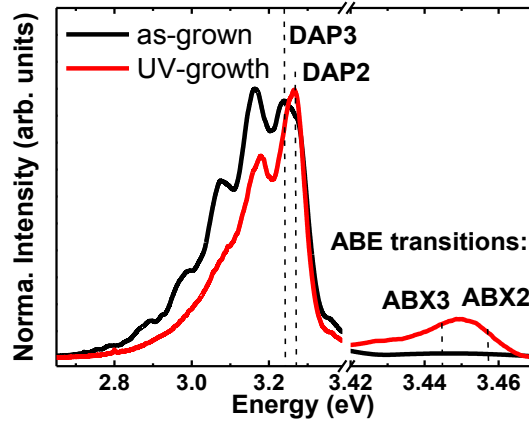
FIG. 19: PL measurement at 3K of two Mg:$2x10^{19}$ cm^{-3} GaN samples as-grown and grown with UV-illumination. UV growth leads to increase in ABE transitions and a blue shift from DAP3 towards DAP2.

Following the electrical characterization by Hall effect measurements and the optical characterization by PL, the incorporation of hydrogen and magnesium is investigated using SIMS similar to the investigations presented in Chapter 3.1.2. Similar ladder structures as discussed here previously have been grown involving 200-300 nm thick intercalated Mg-doped layers with different Mg concentrations and each separated by undoped layers.

Accordingly, SIMS atomic concentration depth profiles of Mg and H on the GaN:Mg ladders grown with and without UV-illumination are shown in FIG. 20. Two different doping concentrations were used for the GaN:Mg ladder: a Mg doping of 3×10^{19} cm^{-3} and 6×10^{18} cm^{-3}. For the SIMS shown in FIG. 20 (a) and (b), it is important to note that these structures have not been activated by a post growth annealing in a furnace. The sample grown without UV-illumination in (a) has an overall high H concentration suggesting the passivation of Mg by Mg-H complexes (Section 3.1.2).[108, 131] In this instance, two different conditions can be observed: (1) For the Mg:6×10^{18} cm^{-3} doping, the H concentration closely follows the Mg concentration and has essentially the same concentration level. (2) For the Mg:3×10^{19} cm^{-3} doping, a H concentration with half that of the Mg concentration with a maximum of 1.5×10^{19} cm^{-3} can be observed. In comparison, the sample grown under UV-illumination in (b) shows a significant reduction in the overall H concentration. The layer doped with Mg:3×10^{19} cm^{-3} has a maximum H level of 8×10^{18} cm^{-3} and furthermore, for the lower Mg concentration of 6×10^{18} cm^{-3}, a reduction in the H level is observed down to a concentration of 2×10^{18} cm^{-3}. It is very important to note that the UV-illumination does not influence the Mg concentration and that the concentration is in agreement with what is expected for the given growth conditions. This is in accordance to the expectations from theory in Section 3.2. In addition to the Mg and H concentrations, the atomic concentrations of the impurities O, C and Si were measured by SIMS (not shown). The actual atomic concentration of Si was below their corresponding background level for the particular measurement and no conclusions can be made. The concentration of C was less than 5×10^{17} cm^{-3} and the concentration of O was 5×10^{17} cm^{-3} for the as-grown sample without annealing, respectively. In this case, O and C are not considered as main compensators in GaN:Mg at this doping concentration as discussed above in Chapter 3.1.2.[85, 114] The UV-growth affects the O concentration slightly and a value of 2×10^{17} cm^{-3} can be determined. The atomic concentration of C remains constant at 5×10^{17} cm^{-3} independent of UV-illumination. That could mean the UV light has either no influence on C incorporation (if C is considered as a donor) or more likely, the acceptor behavior of C in GaN:Mg is dominating, since acceptor concentrations should not be change by the UV growth.
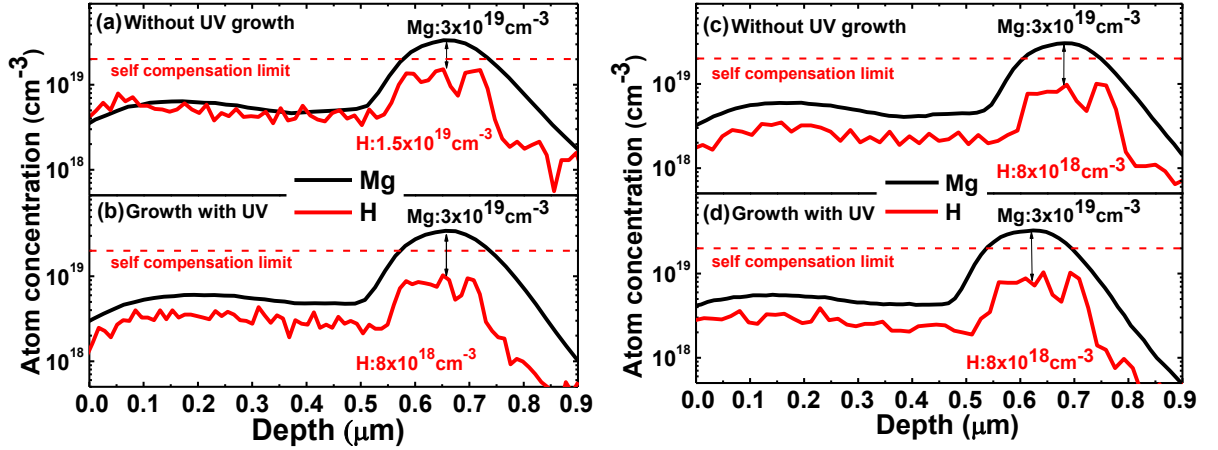
FIG. 20: SIMS analysis of GaN Mg "ladders". All ladder structures have two layers doped with Mg:6x10^{18} cm^{-3} and Mg:3x10^{19} cm^{-3}. (a) As-grown ladder without UV-illumination. (b) UV-grown ladder without annealing. (c) Annealed ladder without-illumination. (d) UV-grown ladder after annealing.

As shown in Table 3, for Mg concentrations of 2x10^{19} cm^{-3} a resistivity of around 1.5±1 Ωcm can be measured with Hall. This resistivity value is understood as being representative for fully activated p-type GaN at this Mg level and is in good agreement for values of thermally annealed p-type GaN grown with MOCVD in the literature.[56, 105, 131, 132] As described previously, The SIMS analysis confirms the reduction of atomic hydrogen by annealing to a concentration of around 2x10^{18} cm^{-3} for Mg doping levels around 6x10^{18} cm^{-3}. This hydrogen concentration seems to be the equilibrium hydrogen concentration that can be achieved after complete activation by thermal annealing below the self-compensation limit, which is in agreement with the conclusions in Chapter 3.1.2. The corresponding H concentration background level for the particular samples is slightly below 1x10^{18} cm^{-3}. In FIG. 20 (c) the as-grown sample and in (d) the UV-grown sample are displayed after thermal activation. For (c) and (d), the SIMS atomic concentration depth profiles after annealing are following the previously described conditions. Both samples (c) and (d) show comparable levels of hydrogen after annealing. This demonstrates that growth under UV-illumination reduces the amount of hydrogen in a similar degree as the post growth annealing does. In addition, it is in very good agreement to the resistivity observations in Table 3. It is interesting to note, that for a Mg concentration of 3x10^{19} cm^{-3} the sample has a residual H concentration of 8x10^{18} cm^{-3} independent of activation by UV-illumination during growth or thermal annealing. This

strongly suggests that this amount of hydrogen is not bound to Mg in the expected Mg-H configuration at this doping concentration and therefore does not respond with further dissociation as was already described in Chapter 3.1.3. This amount of hydrogen could be present in a different charge state or form a different neutral complex,[108] such as bound to V_N [79, 121] or another neutral Mg-H complex, thus making it stable against illumination during growth or annealing. Another explanation could be a hydrogen-related complex as an acceptor. As mentioned above, UV-Illumination (as a Fermi-level control scheme) would not be effective in changing the incorporation parasitic acceptors.

The two observed H incorporation levels in SIMS could be understood in terms of the self-compensation limit that is in agreement with the resistivity measurements in Table 3. Below the limit, H is present at the same concentration as Mg before the activation anneal, thus only H bound to Mg in the form of Mg-H complexes is expected. Above the self-compensation limit, not all Mg is bound to H; therefore passivation by the Mg-H complex cannot be the main reason for the increase in resistivity. This argument justifies the assumption that above this limit, native point defects or their complexes such as V_N or V_N-Mg complex, as described by Kaufman *et al.*,[83] are involved in the compensation. Due to the lower amount of hydrogen, V_N-H complexes can also be excluded as a main reason for the compensation at this higher doping range. This observation clearly indicates that hydrogen incorporation becomes less favorable at Mg concentrations greater than 3×10^{19} cm^{-3}, which is similar to the observation by Castiglia *et al.*[108]

Overall, there is a significant reduction in the H incorporation when the GaN:Mg is grown under UV-illumination, independent on the Mg concentration and its relation with the self-compensation limit. This can be clearly observed in SIMS and resistivity measurements. It indicates that above bandgap illumination suppresses the incorporation of H as a charged defect (H+) and reduces the formation of the Mg-H complex during growth. Note that illumination only has an effect on charged species and not on neutral states. This could explain the observation that a residual amount of hydrogen can be measured in highly doped samples and it indicates that H in these samples is incorporated as a neutral state or in a neutral complex.

3.3.3 Point Defect Control of V_N During the Growth

After the description of the influence of UV illumination during the growth on the incorporation of hydrogen below the self-compensation limit at 2×10^{19} cm^{-3}, the influence on the self-compensation will be analyzed. As discussed in Chapter 3.1.3, the main reason for self-compensation in GaN:Mg is the V_N and possible complexes of those, like the V_N-Mg complex or the V_N-H complex. As discussed in the previous Chapters 3.3.2 and in 3.1.3, the V_N-H complex is unlikely the major reason for self-compensation, since SIMS showed no significant concentrations of H and the model of Kaufmann *et al.*[83] involving V_N-Mg and the triple charged V_N is a better explanation. The following discussion concerns the influence of UV-illumination on the Hall resistivity and PL on a doping series between 1×10^{19} cm^{-3}–5×10^{19} cm^{-3}.
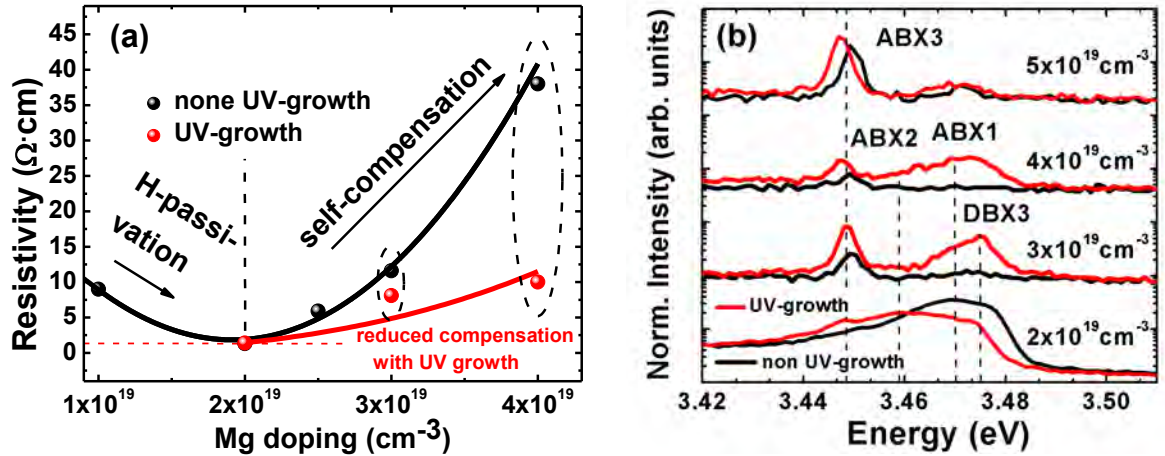
FIG. 21: Self-compensation of GaN:Mg with and without UV-illumination during the growth. (a) Resistivity measurements as function of Mg doping concentration (lines guide to the eye). All samples underwent post growth annealing. Results from the UV-grown samples indicate less compensation at high doping. (b) PL measurement at 3K of the bound excitons. More intense ABX transitions can be observed for UV-growth.

In FIG. 21 the resistivity and bound exciton transitions of samples grown with and without UV-illumination are shown to describe the activation of Mg. In (a), a typical resistivity curve describing the self-compensation is presented. Values for the samples grown without illumination are in accordance to Table 3. All used samples have been annealed to focus the observations on the self-compensation and reduce the passivation by hydrogen. As discussed in Section 3.1.3 the resistivity increases with Mg doping above 2×10^{19} cm^{-3} as result of the

self-compensation by V_N or their complexes. For UV-grown samples, a decrease of the resistivity in comparison with samples grown without UV illumination is observed. At 4×10^{19} cm^{-3}, a big change in resistivity can be achieved by UV illumination. The resistivity has changed by a factor of 4 from 38 Ωcm to 10 Ωcm. This directly suggests a significantly reduced self-compensation caused by the illumination during growth. At Mg:2×10^{19} cm^{-3} and below, a very slight influence on the resistivity could be determined. Below the self-compensation limit, the crystal is mostly just passivated by H, which is removed by the UV or the post growth annealing. Therefore, the resistivity of the sample in this regime is limited by the ionization energy of Mg at given temperature, which will not be affected by the UV growth. In this regime, no major change of the resistivity is expected in accordance with the experimental results.

To compare the resistivity results and justify the argument of a reduced compensation of Mg evoked by UV illumination during growth, the PL at 3K in the range of the bound excitons is displayed in FIG. 21 (b). The Mg:2×10^{19} cm^{-3} UV-grown sample reveals only a small change of the BX transitions with a slight shift of the maximum towards a more intense ABX2 and ABX3 and a decrease of the DBX3 transition in comparison to non UV growth. This could be explained by a reduced amount of oxygen donors by the UV illumination, therefore proving a demonstration of the illumination on the compensating donor concentration. However, as concluded in Section 3.1.3, oxygen is no major compensator of GaN:Mg in this doping regime and therefore, no major change in the resistivity can be expected. For Mg:3×10^{19} cm^{-3} and Mg:4×10^{19} cm^{-3}, the UV-illumination leads to a well pronounced increase of the ABX transitions. ABX1 can be exclusively observed for the UV-grown samples but not in the non UV-grown samples. For the Mg:5×10^{19} cm^{-3} sample, a slight increase in the ABX3 intensity can also be observed. These observations are consistent with the observation of a decreased resistivity in FIG. 21 (a). In addition to the changes in intensity of the ABX transitions, a slight red shift of the ABX peaks can be observed due to UV light illumination which can be explained by a changed point defect concentration like a changed V_N-Mg defect incorporation.
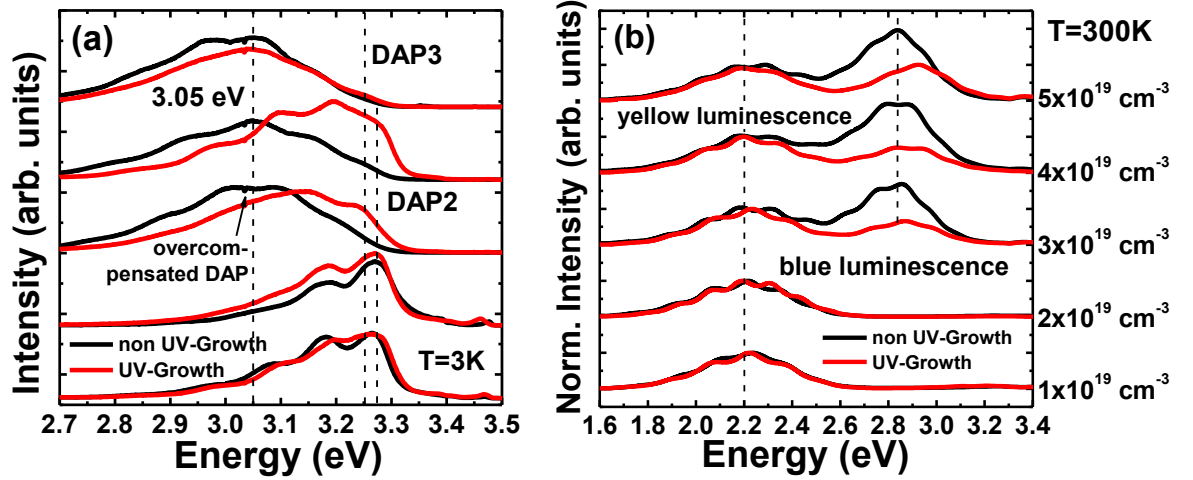
FIG. 22: PL of GaN:Mg doping series grown with and without UV-illumination. (a) PL at 3K. The UV-illumination has a significant influence on the DAP transitions. (b) PL at 300K. The UV-illumination changes significantly the intensity of the blue luminescence at 2.85 eV in the self-compensation range above Mg:2x10^{19} cm^{-3}.

As demonstrated in Section 3.1.3, the deep luminescence, specifically the DAP transitions and the blue luminescence, can give valuable insight into the self-compensation of GaN:Mg. In FIG. 22 the PL at 3K in (a) and the PL at room temperature in (b) as function of doping are displayed. The red curves represent the spectra of UV-grown samples and the black curves represent the non UV-grown samples. In (a) the influence of the UV growth on the DAP and overcompensated DAP transitions are presented. For Mg:1x10^{19} cm^{-3} and Mg:2x10^{19} cm^{-3} doping, the UV illumination during growth leads to a more intense ABX transition and an increase of the DAP2 intensity as described in the previous chapters. Above the self-compensation limit for Mg:3x10^{19} cm^{-3} – 5x10^{19} cm^{-3}, non UV-grown samples reveal an overcompensated DAP with a maximum at 3.05 eV, typically for the self-compensation of Mg. In Section 3.1.3, the origin of this maximum was identified as V_N-Mg complexes or at least V_N-related. The change of the luminescence in (a) by the UV illumination during growth is significant. The UV-illumination seems to blue shift the overcompensated DAP luminescence and DAP2 and DAP3 transitions can be observed for samples doped as high as Mg:3x10^{19} cm^{-3} and Mg:4x10^{19} cm^{-3}. This is explained by a decrease of the underlying blue luminescence at ~3.05 eV and an increase of the DAP transitions. This interpretation directly suggests a reduction of the self-compensation by V_N-Mg complexes. Furthermore, since the

presence of the DAP2 and DAP3 indicates more Mg acceptor states that are not bound to V_N but available for electric conductivity (compare resistivity in FIG. 21 (a)). The Mg:$5x10^{19}$ cm$^-$^{3} sample shows only a minor influence of the UV-illumination. Just a slight decrease and shift of the overcompensated DAP transition towards the DAP transitions can be found. The change of the formation energy by the UV illumination at this doping concentration might not be efficient enough to decrease the compensation or another defect or complex is effective at this doping concentration that cannot be controlled by the UV (e.g. a deep acceptor).

This interpretation is supported by the investigation of the influence of the UV light on the blue luminescence at 2.85 eV as displayed in FIG. 22 (b) (room temperature PL). The spectra have been normalized to the yellow luminescence at 2.2 eV. As discussed earlier, no big changes in the yellow luminescence intensity are expected, since the origin of the yellow luminescence is C related[116] and its concentration is constant in all samples (Section 3.1.3). Below the self-compensation limit, no blue luminescence can be observed for any sample as comparable few nitrogen vacancies are incorporated. An increase of the Mg concentration leads to an emerging blue luminescence at 2.85 eV. The samples grown under UV illumination with doping above the self-compensation limit reveal a significant reduction of the blue luminescence suggesting a severe reduction of the V_N-Mg complexes. This observation fully confirms conclusions drawn from the spectra presented in FIG. 22 (a). The only difference compared to the observations from FIG. 22 (a) is that in the Mg:$5x10^{19}$ cm^{-3} sample grown with UV, a reduction of the blue luminescence can be found. However, the luminescence seems to be a little more intense than of the Mg:$3x10^{19}$ cm^{-3} and Mg:$3x10^{19}$cm^{-3} UV-grown samples. The UV light, therefore, also decreases the V_N compensation for Mg:$5x10^{19}$ cm^{-3}, but as mentioned above, the change in formation energy for this doping concentration might be effective.

To fortify the argument of a reduced V_N-concentration by UV and its affiliation to the blue luminescence, PLE measurements were performed. In FIG. 23 the PLE at 2K on two Mg:$3x10^{19}$ cm^{-3} samples grown with and without UV-illumination is shown. The detection for both samples was set around the blue luminescence at 3.0 eV. Similar PLE measurements were presented in Section 3.1.1 where the ABX and DBX transitions were identified. The PL signal of the Mg:$3x10^{19}$ cm^{-3} sample is presented for comparison and identification of the recombination channels.
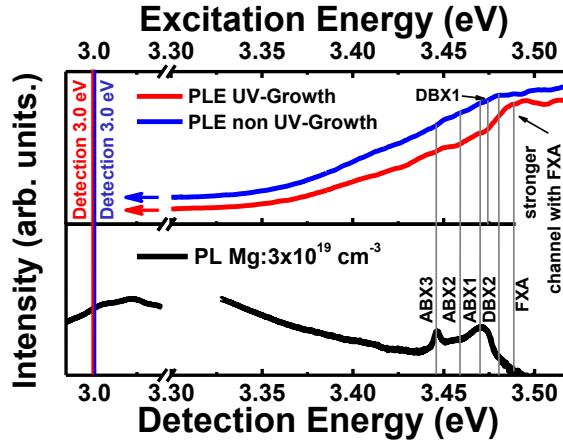
FIG. 23: [b] **PLE at 2K of GaN doped with Mg:3×10^{19} cm^{-3} grown with and without UV-illumination. Detection on blue luminescence at ~3.0 eV. The excitation spectrum for the UV-grown sample is different to that of the as-grown sample. The UV-grown sample shows a stronger excitation channel with the FX and almost none with DBX2 and DBX1.**

The excitation spectrum of the non UV-grown sample in FIG. 23 reveals an excitation channel with all the ABX transitions, as well as the DBX1 and DBX2. This can be understood in terms of an overlap of the DAP transitions and the blue luminescence for this Mg doping concentration (compare FIG. 22(a)). On the other hand, the blue luminescence is expected as a transition between V_N-Mg donors and Mg acceptors[83] and should have excitation channels with ABXs and the DBX1. The presence of an excitation channel with DBX1 is very interesting since the DBX1 was identified as V_N or at least V_N-complex related (Chapter 3.1.1). Thus, the DBX1 is expected to have an excitation channel with the blue luminescence. The excitation spectrum of the UV-grown sample still shows the ABX excitation channels, but excitation channels with DBX1 and DBX2 are missing. However, a more prevalent excitation with FXA and FXB can be found. A reduction of the donors connected to DBX2, and especially DBX1, is evident. This observation is very much in agreement with the reduction of self-compensation in highly-doped GaN:Mg by the UV. The disappearance of DBX2 as an excitation channel, also suggests a reduced amount of oxygen donors. Reduced amounts of Mg compensating donors can be found in PLE on an UV-grown sample.

---

[b] This PLE measurement was performed by Christian Nenstiel at the TU-Berlin as part of a collaborated research on GaN:Mg.

3.3.4   UV illumination During the Growth of Low Mg-Doped GaN

In the previous chapters it was proven that above bandgap illumination during the growth of highly doped GaN reduces the incorporation of compensating donors like H and V_N. But the concept of point defect control by above bandgap illumination, as discussed in Chapter 3.2, is not just limited to p-type material. It can be used as well in n-type material. To demonstrate that this concept is also feasible for n-type GaN, the results on low Mg-doped GaN are discussed below. As it was observed in Sections 3.1.2, 3.1.3 and 3.3.2, a background concentration of oxygen is omnipresent in all GaN layers, independent of any Mg doping. Since oxygen typically acts as a shallow donor, undoped or low Mg-doped GaN samples can be considered to be n-type (with very low carrier concentrations). Thus, at low Mg doping concentrations, Mg is the compensating defect of the donor like point defect O. The incorporation of Mg can be controlled by the UV-above bandgap illumination during the growth. Since SIMS measurements cannot give reasonable results for low Mg concentrations because of the detection limit of Mg at $\sim 5 \times 10^{17}$ cm^{-3}, the following investigations are solely based on PL results.
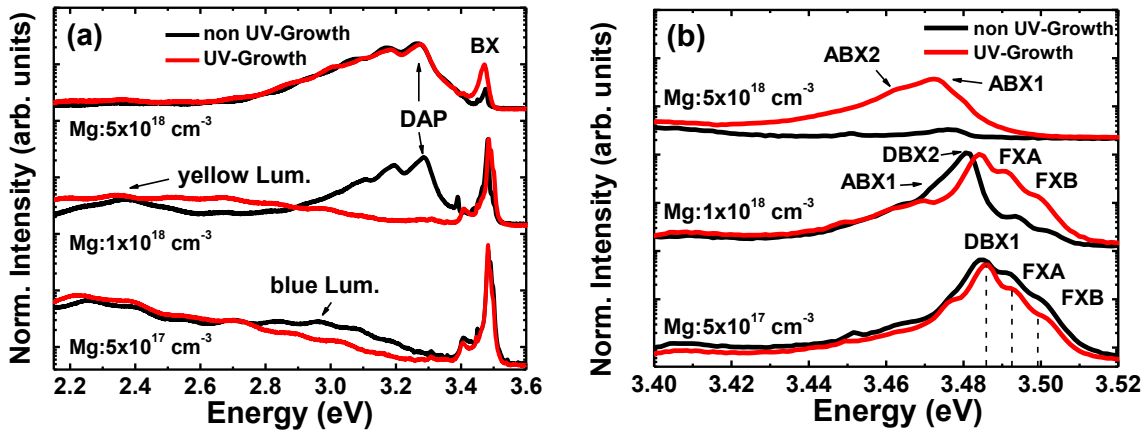
FIG. 24: Low temperature (3K) PL of GaN:Mg with low doping concentration grown with and without UV-illumination. (a) DAP, blue- and yellow luminescence at low Mg doping. (b) bound exciton transitions. UV-illumination at low Mg doping leads to a decrease of Mg incorporation and an increase of donor related emission.

In FIG. 24 the PL at 3K of samples doped with 5×10^{17} cm^{-3} – 5×10^{18} cm^{-3} are presented. The luminescence of samples grown with and without UV is shown. In FIG. 24 (a), the deep

luminescence is shown with focus on the yellow, blue and DAP transitions. In FIG. 24 (b), the near band edge bound exciton PL can be seen. The sample doped with Mg: 5×10^{17} cm^{-3} has intense BX transitions and a yellow luminescence at 2.2 eV. The yellow luminescence is related to C[116] and represents the C background concentration that is related to the growth condition.[59] In addition, a weak blue luminescence at ~3.0 eV can be found. The UV-growth at this doping concentration decreases the blue luminescence intensity; the yellow luminescence is not affected. In the range of the near band edge luminescence of the Mg:5×10^{17} cm^{-3} sample, a strong DBX1 luminescence and the FXA and FXB transitions are observed. The growth under UV illumination decreases the FX transitions and increases the intensity of the DBX1 transition. In addition, a slight blue shift of the BX transition can be observed as discussed in Section 3.1.3. Hall resistivity measurements revealed, despite the doping with 5×10^{17} cm^{-3} Mg, n-type resistivity for the UV-grown sample and a highly resistive film (not measurable) for the sample grown without illumination. From these observations the reduction of compensating Mg by the UV-illumination can be concluded which leads to stronger V_N and O related DBX emission and the observed blue shift. In addition, a decrease of the FX transitions can be found as the free excitons have a higher probability to bind to a defect. The reduction of the blue luminescence by UV illumination during growth may then also be explained by reduced incorporation of Mg acceptors as compensators for the donors V_N and O since the blue luminescence is connected to Mg acceptors and V_N-Mg donors.

For Mg:1×10^{18} cm^{-3}, a similar conclusion can be made. Hall resistivity measurements indicate an n-type resistivity of ~0.02 Ωcm for the UV-grown and a very high resistance for the non UV-grown sample which is attributed to an increase of the donor concentration and a decrease of the Mg acceptor concentration. In FIG. 24 (a), the sample grown without UV illumination, shows a DAP1 transition at 3.287eV. UV illumination during growth leads to a complete disappearance of DAP1 and a very weak intense blue emission. In addition, a change of the bound exciton luminescence can be observed in FIG. 24 (b). The sample that has not been grown with UV illumination has a DBX2 and an ABX1 transition which is related to oxygen and Mg responsible for the DAP transition in FIG. 24 (a). The growth with UV-illumination and 1×10^{18} cm^{-3} Mg doping, leads to a decrease of the ABX1 transition and to a more intense DBX1 and DBX2 transition. The peak position of the DBX1 is similar to that observed in the

sample with Mg:5×10^{17} cm^{-3} grown under UV illumination. This indicates that the blue shift is caused by more compressive strain through the decreased Mg concentration (Mg on lattice site introduces tensile strain).

In contrast to the low-doped samples, the sample grown with 5×10^{18} cm^{-3} Mg doping shows no significant influence of the UV growth on the DAP1 luminescence (FIG. 24 (a)). The bound excitons are dominated by the ABX1 and ABX2 transition when grown under UV illumination. The intensity of the ABX transitions significantly increases by UV-growth. This observation suggests the decrease of hydrogen passivation of Mg by Mg-H complexes as it was discussed in Chapter 3.3.2. For concentrations above 5×10^{18} cm^{-3} the Mg doping concentration dominates the donor concentration and the UV, therefore, leads to a reduction of Mg compensating donors.

In conclusion, a study of the influence of UV illumination on donor-dominated GaN was represented. When the Mg doping level is on the scale of intrinsic donor concentrations, Mg is understood as being the compensating acceptor. Thus, above bandgap UV illumination controls and modifies the incorporation of Mg and lower Mg levels can be found due to the UV light. At higher concentrations around 5×10^{18} cm^{-3}, the UV illumination leads to an enhanced p-type film as it was discussed in earlier sections. For Mg:1×10^{18} cm^{-3}, a strong n-type character was produced by the UV light. The intrinsic concentration of O_N, V_N and any other donors, has to be in the order of 10^{18} cm^{-3}. It should to be pointed out that the idea of a relation between the blue luminescence and the V_N-Mg donor and Mg acceptor is in very good agreement with the observations of a reduced Mg concentration. The increase of V_N donors as function of UV-light during growth is very interesting; as a higher V_N concentration seems to be present at this doping concentration, then it would be expected. On the other hand, the change of the formation energy for the V_N might be higher in comparison to O at this Mg doping level. Further theoretical calculations will be necessary in the future to support this idea.

The concept of UV illumination can be used for n-type material, as well as for p-type material. Mg-doped GaN was used here only as a model system, but the concept can be applied to any material. It is expected that it can be very useful for example for N-polar GaN,

where the intrinsic concentration of O is two magnitudes higher than in Ga-polar GaN. In a lateral p/n-junction the O concentration difference is used for creating a p-type Ga-polar film and an n-type N-polar film side-by-side. Both layers are Mg doped with $2x10^{19}$ cm^{-3} and the excess of O is responsible for the n-type character in the N-polar film. However, the donor concentration is compensated by the Mg. As it was discussed above, the Mg compensation can be controlled in donor dominated GaN. UV illumination during the growth of lateral p/n-junctions with side-by-side doping of Ga-polar and N-polar films can, therefore, control point defects in both layers simultaneously. It is expected that the quality of lateral p/n-junctions can be enhanced. According investigations will be presented in the next chapter.

3.4   Summary

The influence of above bandgap illumination was investigated using GaN:Mg as a model system. To be able to understand the influence of UV illumination, point defects in GaN:Mg were investigated first. PL and PLE was used to identify the reason for passivation of Mg at low doping concentrations below the self-compensation limit of Mg:2×10^{19} cm^{-3}. The PL shows the appearance of acceptor bound exciton ABX1 at 3.47 eV, ABX2 at 3.458 eV and ABX3 at 3.445 eV. In addition, the donor bound exciton DBX1 at 3.483 eV, DBX2 at 3.480 eV and DBX3 at 3.474 were identified. The DAP observed typically in GaN:Mg at ~3.27 eV was identified as an overlap of three DAP transitions: DAP1 at 3.287 eV, DAP2 at 3.275 eV and DAP3 at 3.256 eV. The DAP transitions are attributed to the donors and acceptors attributed to the DBX and ABX transitions. DAP1 is attributed to DBX2 and ABX1 or ABX3, while DAP2 is attributed to DBX2 and ABX2 or ABX3. The DAP3 transition is based on DBX2 and ABX3. For the DBX and ABX transitions, the according binding energy was determined. From the binding energies, the species of the bound excitons was verified using Haynes rule. DBX1 was identified as a V_N-related donor, DBX2 as related to an oxygen donor and DBX3 as an overlay of an ionized DBX2 and a neutral donor. The acceptor bound excitons were identified as Mg in different states. ABX1 was identified as a shallow transient state of Mg and ABX3 is a deep ground state of Mg. This finding is in excellent agreement to the theoretical work of Lany et al.[73] and from the experimental observations of Monemar et al.[72] The DAP transitions are related to the oxygen donor and Mg in different states.

Following the identification of Mg doping-related emission lines in the PL spectra, the new knowledge was applied to evaluate thermal activation of GaN:Mg samples. It was shown that the activation of Mg-doped GaN, which is understood as the dissociation of the Mg-H complex, leads to an increase of the ABX3 and ABX2 transitions with a dominating DAP2 transition. A luminescence trace of the Mg-H complex was not found in PL. The reduction of Mg passivation at doping concentrations around 2×10^{19} cm^{-3} lead to the appearance of the deep ground state of Mg by ABX3 with a binding energy of 195 meV. Residual Mg acceptors are compensated by oxygen donors at the concentration of ~2×10^{17} cm^{-3} and are responsible for the DAP2 peak. The use of UV-illumination during the post growth annealing and the illumination with UV-light during growth of Mg-doped GaN below the self-compensation limit lead to a decrease of the H concentration as observed with SIMS measurements. Thus, it was demonstrated that the incorporation of H is be controlled by UV illumination. As a fingerprint of this reduced H incorporation, a reduced Mg-H passivation was found. This can

make post growth annealing obsolete. Using comprehensive PL and SIMS measurements, it was shown that above the self-compensation limit of 2×10^{19} cm^{-3}, Mg-doped GaN is compensated by V_N-related defects. This explains the typically observed radical decrease of the resistivity in this doping regime. The most likely compensator of Mg is the Mg-V_N-complex which is also responsible for the blue luminescence at 2.85 eV in PL spectra (at 300K) of GaN:Mg. Using SIMS analysis, hydrogen-related passivation or compensation of Mg could be excluded as the main reason for the self-compensation. Any residual hydrogen concentration was shown to be stable against thermal annealing and UV illumination during the growth. As a possible explanation, it was suggested that for higher Mg doping ranges, hydrogen is incorporated in a different state.[108] UV illumination of GaN:Mg doped with more than 2×10^{19} cm^{-3} significantly decreased the blue luminescence which was accompanied by a decrease in the Hall resistivity. The above bandgap illumination during the growth was able to decrease the number of V_N-Mg donors in the crystal and control the self-compensation. This observation was found to be consistent with PLE measurements on UV-grown Mg-doped GaN. Thereby, the disappearance of DBX1 and DBX2 as blue luminesce excitation channels, suggest a decrease in donor concentrations by the UV. DBX1, identified with V_N-related donors, was reduced by the UV. In addition, a reduction of oxygen represented by DBX2 was observed.

Finally, the applicability of above bandgap illumination to control the point defects in n-type semiconductors was investigated. For low-doped GaN:Mg below Mg:1×10^{18} cm^{-3}, where the doping concentration is similar to the oxygen (donor) background concentration, the UV illumination during the growth resulted in a strong decrease of Mg compared to non UV-grown samples. At Mg:1×10^{18} cm^{-3} a significant n-type conductivity observed caused UV illumination during growth, while non UV-grown samples were highly resistive. This argued that at Mg doping below 1×10^{18} cm^{-3} Mg acceptors are the compensator to intrinsic or extrinsic donors like oxygen.

UV-growth can, therefore, control the compensation of n-type doping by acceptors. Using Mg-doped GaN as a model system, these results show that a point defect control by UV illumination during the growth is feasible in n-type and p-type films. This scheme can be used to control compensation of dopants in almost any semiconductor were strong compensation effects occur.

4. Growth and Fabrication of AlGaN-based Lateral Polar Structures

AlGaN films with N- and III-polar orientation can be grown side-by-side by forming a lateral polar structure (LPS). These LPS can used for a variety of applications like photonic crystals[133], oxide integration or lateral transistors structures, but the most prominent applications that have been demonstrated are second harmonic generation (SHG) by quasi phase matching (QPM)[8, 134, 135] and lateral polar p/n-junctions.[22, 136] In the following chapter, the fabrication and growth of those AlGaN LPS are investigated, focused on SHG as an application. Here a smooth domain surface of opposite polarity, a sharp interface between the domains and equal heights are crucial for wave propagation within the structure and to achieve sufficient conversion of light by quasi-phase matching. Nevertheless, a detailed characterization of the polar domains and the enhancement in quality of AlGaN LPS are important for all applications that could arise from the use of these structures. The whole composition regime from GaN, to AlN in a LPS is therefore investigated in the following chapter.

Since SHG is one of the major goals that follow as an application of AlGaN LPS, the first Section (4.1) will describe its applicability for quasi phase matching and its design with respect to the expected conversion efficiency of the structure. For this, the required periodicity of N- and III-polar patterns in the form of stripes that affect QPM will be discussed.

In Section 4.2, the fabrication and growth of high-quality GaN LPS will be presented. Here the influence of the fabrication on the quality of the inversion domain boundaries and the influence of the growth conditions on the growth rate of simultaneously grown N- and Ga-polar domains in close proximity will be studied.

Section (4.3) will determine the influence of the Al composition in AlGaN LPS on the surface quality and growth rate of the domains. In addition, an AlN LPS will be demonstrated for the first time as this is most desired for SHG in the UV, a section will focus on the characterization of such structure.

4.1　Design of Lateral Polar Structures for Second Harmonic Generation

AlGaN can be used for nonlinear optics device. Nonlinear optics devices allow for the conversion of the wavelength of coherent light sources, like lasers, via second harmonic generation (SHG).[8, 137-140] Here the fundamental wavelength of a laser is converted to half of the original wavelength or in terms of frequency, the fundamental frequency ω is doubled to 2ω. Often this process is also called frequency doubling. AlGaN alloys can be used for second harmonic generation, since they exhibit a relatively large on-axis nonlinear coefficient $d_{33}^{(2)}$. The second order nonlinear optical coefficient of a wurtzite crystal has a second-rank tensor that simplifies by symmetry considerations and by considering arguments based on the dispersion of the electronic contribution to the nonlinear susceptibility, to two independent components $d_{31}^{(2)}$ and $d_{33}^{(2)}$. In practice, only the on-axis nonlinear optical coefficient $d_{33}^{(2)}$ is involved in a SHG experiment. For example, in the case that SH light can be generated from a certain fundamental light, the input field at frequency ω is polarized along the z-axis. Hence, the generated polarization is only polarized along the z-axis, and the relevant component of the tensor is $d_{33}^{(2)}$. In this case, the other nonlinear optical coefficient $d_{31}^{(2)}$, vanishes. Thus, for the case of SHG, the frequency-domain polarization $P_z^{(2\omega)}$ is related to the frequency-domain components of the applied electric fields by (8):[141]

$$P_z^{(2\omega)} = 2\varepsilon_0 d_{33}\left[E_z^{(\omega)}\right]^2 \tag{8}$$

The second harmonic nonlinear optical coefficient $d_{33}^{(2)}$ for GaN has been determined theoretically to be 6 pm/V[142] and experimentally around 7–16 pm/V.[143, 144] For AlN, values between 4–7 pm/V were reported.[143, 145] AlGaN alloys lack experimental data, but based on the observed values for the end members, the $d_{33}^{(2)}$ can be estimated to be around 4–16 pm/V. In addition to such large nonlinear coefficient, AlGaN alloys exhibit distinct advantages over conventional nonlinear materials like $LiNbO_3$ and GaAs. The transparency window for $LiNbO_3$ is between 350 nm – 5 µm and for GaAs between 873 nm – 13 µm. The transparency

window for GaN ranges between 365 nm – 13.6 μm, thus covering the whole range of LiNbO$_3$ and GaAs. GaN has the potential to be used for SHG in either the far infrared or the near UV. Furthermore, the window can be extended deeper into the UV (~200 nm) by alloying GaN with AlN. From this, AlGaN alloys would be an excellent alternative for optical frequency conversion into the mid- and deep-UV range, where electrically pumped semiconductor lasers have not been achieved.

However, efficient wavelength conversion requires phase matching between the fundamental and second harmonic light ($n^{2\omega} = n^{\omega}$). III-nitrides possess insufficient birefringence for conventional phase matching, because of optical isotropy. FIG. 25 (a) shows in the bottom that the phase matching condition for Nitrides cannot be fulfilled, since there is no θ that satisfies the following condition: $n_e^{2\omega} = n_o^{\omega}$. Thus, quasi phase matching (QPM) is instead used; QPM allows for constructive interference of propagating waves which increases SHG efficiency.[146, 147] QPM can be achieved in devices through periodic, lateral polarity inversion along the c-axis, particularly in III-Nitrides. Such devices are called periodically oriented lateral polarity structures (PO-LPS) or simply LPS and consists of III-polar and N-polar domains grown side-by-side. This periodic alternation of the sign of the nonlinear coupling coefficient can compensate for a nonzero wave vector mismatch.[148, 149]

The effect of QPM is shown in FIG. 25 (b) by the second harmonic output power as function of distance in the nonlinear crystal (see equation (11)). For non-phase matching, the alternation of the sign of the SH power leads to a repetitive "growth" and "decay" of the output power. In contrast, quasi phase matching, by alternating the sign of $d_{33}^{(2)}$ after a coherence length, l_{coh}, which leads to an ongoing "growth" or increase of the SH output power. Thus, QPM leads to an inversion of the relative phases of the forced and free waves after an odd number of l_{coh}. A proper phase relation is maintained for the increase of the SH output power.[150]

QPM in periodically poled structures has proven to be a very useful technique to achieve SHG in GaAs.[147, 151-153] On the other hand, this approach have been unsuccessful in ZnO,[154] where the fabrication of such structures have proven difficult. So far, periodic structures in wurtzite GaN (LPS) have mainly been demonstrated by using molecular beam epitaxy (MBE).[8] However, the crystalline quality and structure periodicity of these GaN-based QPM structures are not sufficient; furthermore, no AlN QPM structures have been demonstrated. Using

MOCVD for the fabrication and growth of LPS has several advantages over MBE in terms of growth rate[155] and ease of point defect control. Therefore, the present work focuses on AlGaN LPS grown by MOCVD, as an alternative to achieve SHG well into the UV by QPM structures.
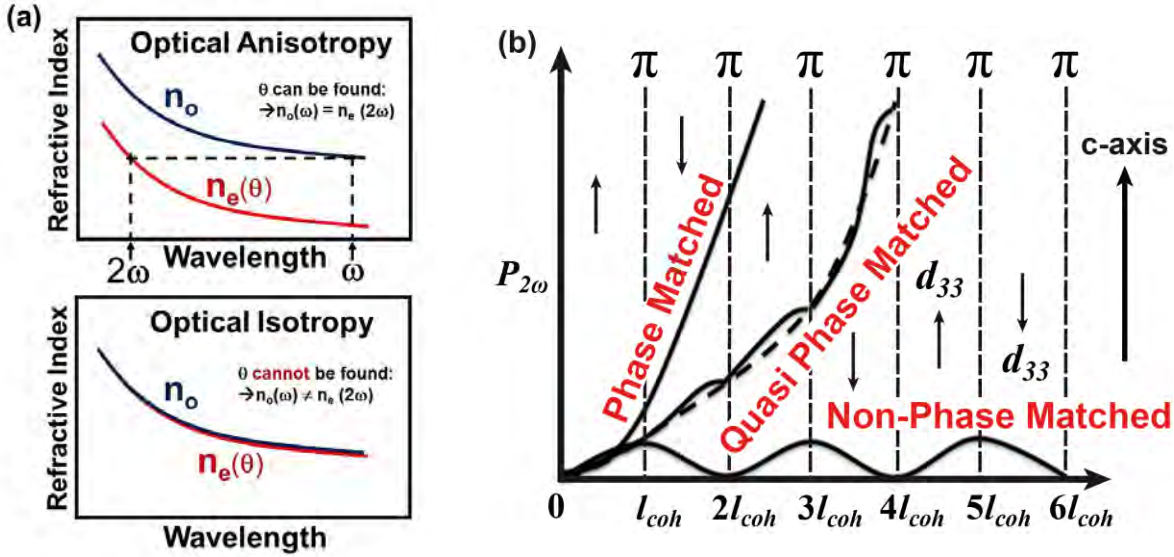
FIG. 25: Birefrigent phase matching versus quasi phase matching. (a) Comparison of optical isotropy and anisotropy. Since nitrides show optical isotropy (just 3% average refractive index difference), birefringent phase matching is not possible and QPM is needed. (b) Second harmonic output power as function of traveling wave distance.[150] Changing the sign of $d_{33}^{(2)}$ after distance l_{coh} leads to quasi phase matching and enhancement of the SH output power.

The design of the LPS plays a significant role if it is used for second harmonic generation. Lateral stripes of N- and III-polar AlGaN have to be grown side-by-side for constructive interference of the traveling waves. The polarization of the propagating fundamental wave, responsible for the SHG, is only polarized along the z-axis thus the SHG conversion is most efficient if the wave is propagating perpendicular to the AlGaN c-axis. A constant phase relation between the interacting waves during their propagation through the crystal is required to achieve quasi-phase matching with efficient energy transfer during the nonlinear frequency conversion. This is achieved through the periodic inversion of the crystal allowing for the periodical modulation of the nonlinear coefficient sign $d_{33}^{(2)}$. For a detailed description of QPM, the reader is referred to the books of A. Yariv (Optical Electronics in Modern

Communications)[156], R. W. Boyd (Nonlinear Optics)[157] or G. New (Introduction to Nonlinear Optics).[158]

The conversion response for QPM depends on the periodicity of the grating along the length of the crystal.[159] The optimum stripe length in a LPS necessary to achieve first order quasi-phase matching depends on the wavelength of the fundamental wave and the refractive index of the material for the fundamental and SH waves.[159] The periodicity of the grating Λ is given by (9):[8]

$$\Lambda = 2 \times l_{coh} = 2 \times \left(\frac{\lambda_\omega}{4(n_{2\omega} - n_\omega)} \right) \tag{9}$$

λ_ω describes the fundamental wavelength at ω, and $n_{2\omega}$ and n_ω are the refractive indices at the second-harmonic and fundamental wavelength. The periodic grating Λ is equal to twice the coherence buildup length l_{coh} (see also FIG. 26) of the nonlinear interaction. The coherence length is, therefore, the stripe length of one polar domain in a LPS. For the case of identical refractive indices of the III-polar and N-polar AlGaN the stripes for both domains have equal length (FIG. 26).
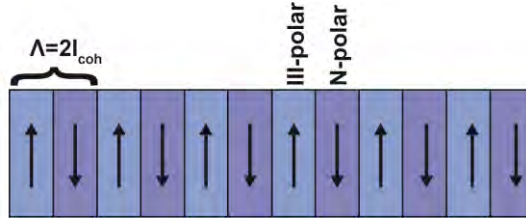
FIG. 26: Schematic of a LPS and the periodic grating

The calculation of the periodicity of the grating Λ needs the dispersion of the refractive indices of the AlGaN. The refractive indices are expressed by the first order Sellmeier dispersion.[160-163] As part of the present work on LPS, the refractive indices of N- and III-polar AlGaN over the whole compositional range was determined. Parts of this work were published in collaboration with Martin Rigler from the University of Ljubljana.[164] The periodic gratings for the AlGaN LPS in the present work were calculated under consideration of these measured values.

The calculation of the periodicity of the grating using Equation (8) is valid only for the first order QPM. This means that the locally generated second harmonic (SH) is out of phase by π with respect to the propagating SH wave after half of the period. QPM of the m-th order is achieved by periodic reversal of $d_{33}^{(2)}$ every m coherence length. Thus, an effective nonlinear coefficient d_{33} can be defined as (10):[148, 159]

$$d_{eff} = \frac{2}{m\pi} d_{33}^{(2)} \tag{10}$$

Equation (10) implies that for a fixed length of the whole structure, the conversion efficiency is $1/m^2$ times lower in the m-th order QPM compared to the first order QPM. The lager period of higher-order QPM leads, therefore, to lower conversion efficiency. Thus, the AlGaN LPS in this present work were designed to achieve a first order QPM, but in general higher order QPM can also be achieved with the fabricated LPS structures.

The conversion efficiency of the LPS is defined by the ratio ($\eta_{SHG}=P_{2\omega}/P_{\omega}$) of the fundamental input laser power P_{ω} and the SH output power $P_{2\omega}$. The SH power $P_{2\omega}$ is given by Equation (11):[165, 166]

$$P_{2\omega} = \frac{8\pi d_{eff}^2 L^2}{n_{\omega}^2 n_{2\omega} c\varepsilon_0 \lambda_{\omega}^2} \frac{P_{\omega}^2}{A_{OVL}} sinc^2(\Delta\beta L/2) \tag{11}$$

In Equation (11), d_{eff} is the effective second-order nonlinear coefficient and L is the interaction length (total length of the stripe structure). The mismatching factor $\Delta\beta$ is defined as $\beta_{2\omega} - \beta_{\omega} = 2(2\pi)(n_{2\omega} - n_{\omega})/(\lambda\text{-}2\pi)/\Lambda$,[149] where β is a mode propagation constant, c and ε_0 are speed of light and permittivity in vacuum, and A_{OVL} is the equivalent overlap area. The overlap area is an area of waveguide on which input light is focused, when coupled into the LPS waveguide.

An optimal periodicity for first order QPM for four different fundamental wavelengths is presented in Table 4. Depending on the SH wavelength, the Al content in AlGaN has to be

matched to compensate for the transparency. As mentioned above, QPM using a LPS can be achieved for wavelengths ranging from the infrared to the UV range. In Table 4 (a), an example for the optimum grating using a Nd:YAG laser with 1064 nm fundamental wavelength is presented, giving a periodic grating with periodicity of ~5.5 μm. This example was chosen because the Nd:YAG laser can achieve high output powers and is excellent for demonstrating the QPM using a GaN LPS. In addition, the values for 532 nm fundamental wavelengths are shown in (c), highlighting the values for the 4th harmonic of the Nd:YAG laser (or 2nd harmonic of 2nd harmonic). Here at least x=0.6 $Al_xGa_{1-x}N$ is needed to make the material transparent at a wavelength of 260 nm. The minimum SHG wavelength 225 nm presented in the Table 4 (d) is achieved by SHG using a pure AlN LPS that converts a fundamental wavelength of 450 nm (InGaN laser) to 225 nm using a grating with 700 nm periodicity. This example is chosen because InGaN lasers with 450 nm are commercially available. It has to be noted that the conversion of a 405 nm blue-ray laser is expected to be close to the absorption edge of AlN even though high-power blue-ray lasers would be the best choice for fundamental power (P_ω) and short SH wavelength (202 nm).

Table 4: Periodic gratings of $Al_xGa_{1-x}N$ LPS for different typically fundamental laser sources

Example	(a)	(b)	(c)	(d)
$\lambda_{fundamental}$	1064 nm	920 nm	532 nm	450 nm
λ_{SHG}	532 nm	460 nm	266 nm	225 nm
$Al_{content}$	0	0	0.6	1
Transparency	362 nm	362 nm	260 nm	202 nm
n_ω[160]	2.29	2.29	2.15	2.11
$n_{2\omega}$[160]	2.39	2.39	2.22	2.43
Λ [a]	5.5 μm	3.4 μm	0.9 μm	0.7 μm

[a] Calculation based on the refractive index determination from Özgür *et al.*[160]

High Al content AlGaN or in the best case, AlN is desired for LPS to convert light into the UV spectral regime. Furthermore, higher Al content and shorter wavelengths provide for a larger refractive index difference, which determines the periodicity of the grating. This facilitates the fabrication of the structure by lithography and etching. In addition, high Al-

content AlGaN is desired, as the value of the nonlinear coefficient $d_{33}^{(2)}$ is strongly dependent on the fundamental wavelength above half of the bandgap energy in AlGaN. Below half of the bandgap, the value of $d_{33}^{(2)}$ is almost constant. For UV applications, the fabrication of AlN LPS is therefore favored.
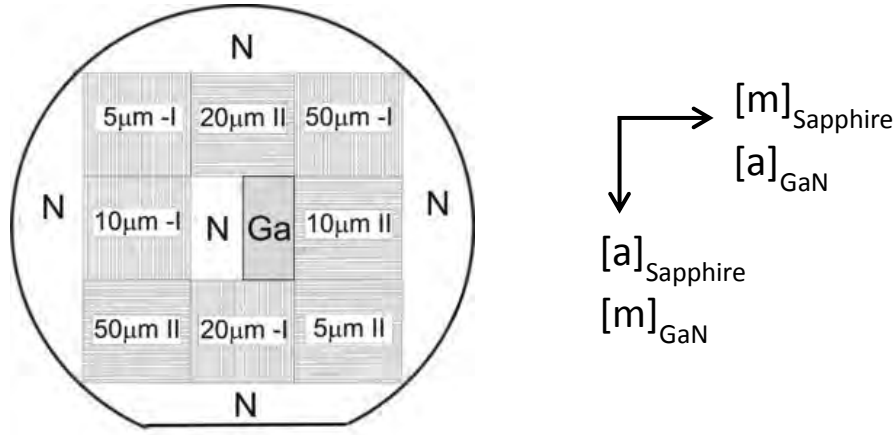
FIG. 27: Mask design / Stripe structure / Orientation

In order to optimize and test the fabrication process of AlGaN LPS and investigate the influence of growth conditions on the quality, a mask with different periodic gratings has been designed. The mask designed for the 2" sapphire wafer is shown in FIG. 27. This mask was primarily used for the fabrication process of AlGaN LPS templates. The fabrication process is described in section 2.5.2. The periodic gratings that can be produced with this mask vary from 10 μm – 100 μm (the values shown in FIG. 27 represent the corresponding coherence length and therefore the width of a single stripe). Also, the mask was designed to test for the influence in growth conditions on the growth rate for stripes parallel and perpendicular to the a-plane. Thus, all the periodic gratings are represented twice on the mask. In the middle of the mask, two large stripes with 5 mm x 10 mm for III- and N-polar AlGaN can be found. (In FIG. 27, the Ga-polar domain in the center represents the III-polar domain.) On the corners, the mask is designed to achieve large N- or III-metal polar domains, depending on the type of photoresist used during the fabrication of the template (negative or positive). The 5 μm grating can be used for testing the conversion using a Ti:Sapphire laser.

4.2   GaN-based LPS: Growth Rate and Crystalline Quality

GaN-based lateral polar structures have been demonstrated by several groups.[167-169] As discussed in the previous chapter (4.1), the LPS consists of Ga- and N-polar GaN grown with MOCVD side-by-side separated by an inversion domain boundary (IDB).[136, 170] It has been demonstrated that under typical growth conditions, GaN growth is mass transport limited, thus the growth rate should be independent of the polar orientation.[153, 154] However, some observations suggest that a difference in the growth rate between the domains exists under certain conditions,[155, 156] especially when the two polar orientations are grown in close proximity. This has led to contradictory conclusions suggesting that there is an intrinsic growth rate difference between the two polar orientations, thus making the fabrication of a flat LPS impossible.[171, 172] To illustrate this problem, in FIG. 28 cross-sectional SEM images of separately grown Ga- and N-polar GaN is presented, as well as a LPS with Ga- and N-polar GaN grown side-by-side.
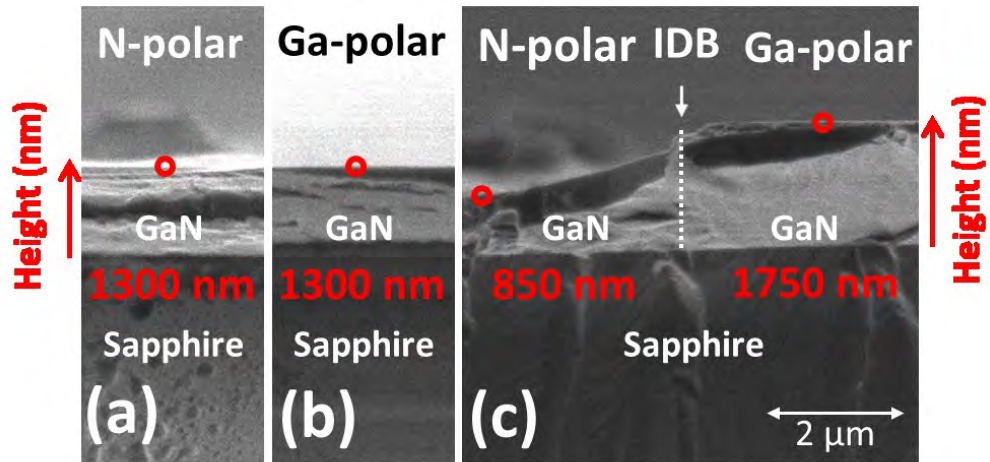
FIG. 28: Cross-sectional SEM images of GaN films grown with the same growth conditions. (a) N-polar GaN grown separately on a full 2" c-plane sapphire wafer. (b) Ga-polar GaN grown separately on a full 2" c-plane sapphire wafer. (c) GaN LPS: SEM close to the inversion domain boundary (10 μm wide stripe structure). The inversion domain boundary was identified in accordance to the literature.[136]

FIG. 28 (a) shows a cross-sectional SEM of N-polar GaN and (b) shows a cross-sectional SEM of Ga-polar GaN, both grown on a 2" sapphire wafer. Both films were grown under the

same conditions and time. Using cross sectional SEM, the thicknesses of the GaN films for both samples was estimated to be 1.3 µm Thus, if N- and Ga-polar GaN is grown separately, the same growth rate is observed. FIG. 28 (c) shows a cross sectional SEM image of a LPS in the vicinity of the IDB. This LPS sample has been grown under the same growth conditions as the GaN films shown in FIG. 28 (a) and (b). In this case, the N-polar domain is 850 nm thick while the Ga-polar domain is 1750 nm thick. This highlights the height difference of 900 nm and demonstrates the growth rate difference of N- and Ga-polar domains when grown side-by-side in a LPS, as mentioned above. The Ga-polar domain in FIG. 28 (c) grows 450 nm thicker than the Ga-polar GaN film in (b). The difference in thickness between the N-polar domain in FIG. 28 (c) and the film in (a) is also 450 nm. A comprehensive estimation of the overall mass of the N- and Ga-polar domains leads to the conclusion that the mass of GaN in FIG. 28 (c) is conserved as compared to (a) and (b) suggesting that the growth is mass transport limited as previously demonstrated for N- and Ga-polar films. This indicates that there is no intrinsic growth rate difference between the N- and Ga-polar GaN. The difference in height was observed when the N- and Ga-polar GaN was grown side-by-side. Two possible explanations were suggested for this observation: (1) the height difference in a LPS is caused by the fabrication process of the templates where a possible surface contamination leads to a delay in nucleation of the N-polar GaN and a positive feedback to the Ga-polar growth. (2) The height difference is caused by the growth conditions, that is, Ga mass transport occurs from one domain to the other as dependent by the process supersaturation. In the following sections these two possibilities are investigated. It will be shown that the latter explanation is very likely and that the mass transport can be controlled via the growth conditions. In addition, the influence of the fabrication on the properties of the LPS is analyzed.

4.2.1   Influence of the Fabrication Process on the LPS Properties

The influence of the template fabrication, especially the patterning by etching, on the quality of the inversion domain boundary, surface roughness and periodicity of the periodically oriented GaN will be presented in the following section. The LPS properties are critical for the conversion efficiency of the crystal if a GaN LPS is used for SHG because of possible scattering of the coupled light. In addition, it was proposed that the patterning was responsible for the height of Ga- and N-polar GaN domains deposited side-by-side due to a delayed

nucleation of the N-polar domain. RIE can critically damage the c-plane sapphire surface during the patterning process,[173] which could influence the nucleation and growth of the N-polar domain. High temperature annealing, typically used to recover any damage thus converting the sapphire surface to be epi-ready cannot be applied to the LPS templates,[174, 175] since the AlN buffer for the Ga-polar domains would be affected by the high temperatures.[176] Thus, a standard H_2-etching and NH_3-annealing should be sufficient. The role of etching on the growth of both polar domains of a periodically poled GaN layer was investigated; especially the surface of the template after RIE and KOH-etching.

In FIG. 29, high-resolution AFM images of the KOH and RIE processed LT-AlN layers are shown after H_2-etching and NH_3-annealing (the pre GaN growth treatments are described in Chapter 2.5.2) to investigate if surface contaminants are present and can be removed. In FIG. 29 (a), the surface of the AlN layer after KOH-etching appears very similar in terms of feature size, to a surface of an unetched AlN layer. This layer underwent the same preparation steps as a KOH-prepared LPS template would, as described in Chapter 2.5.2. No surface features associated to contamination can be observed resulting from KOH etching or the fabrication process. Therefore, the LT-ALN can be assumed to be epi-ready for Ga-polar GaN growth. It should be noted that films resulting from KOH etching exhibit this surface property even before the H_2 and NH_3 annealing. This indicates that very minor surface defects (not shown) are introduced by KOH and the related processing steps. Thus, a pre-growth treatment is not mandatory for the AlN-layers. In contrast to KOH processing, a contamination layer (not shown is observed on the surface of the AlN nucleation layer, which resulted from RIE etching (possibly hydroxides).[177] The contamination layer (hydroxides) on the surface interferes with AFM probing, which is seen by the elongation of AlN islands on sapphire while undergoing AFM topographic imaging. If the surface is not annealed, this contamination layer can influence the growth of Ga-polar GaN on the surface. However, a post growth 20 min H_2-etching in combination with 10 min NH_3-annealing (FIG. 29 (b)) can clean the surface and transform it back into a grainy structure with small features similar to the KOH-etched surface. A shorter etching and annealing time lead to a partially removed contamination layer that resulted in mixed polar GaN domains. Thus, H_2 and NH_3 treatments are needed after the RIE etching procedure to reduce the amount of contamination and surface damage, creating an epi-ready surface for the Ga-polar GaN growth.[60]
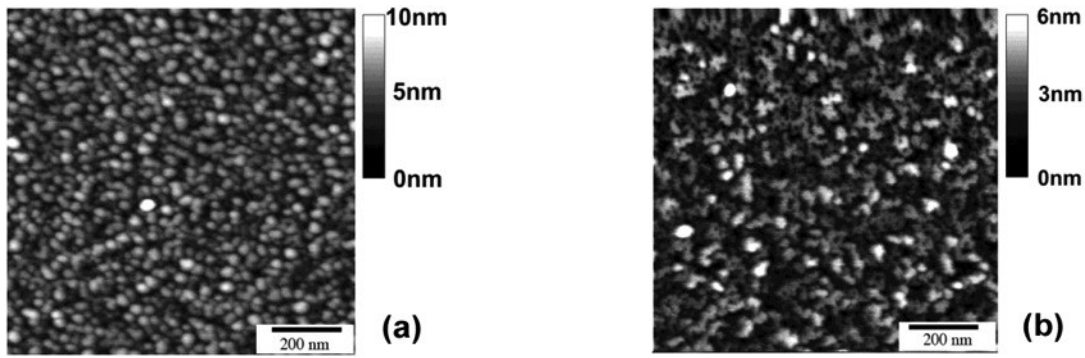
FIG. 29: AFM on the AlN surface after KOH (a) and RIE etching (b) and after H_2 and NH_3 annealing in the MOCVD reactor.

The AlN layers are typically not affected by the etching as they are protected by photoresist or a Ti-mask. In contrast, the c-sapphire surface is directly exposed to the RIE- and KOH-based etching process. AFM images of the templates after etching to the c-sapphire surface with RIE (b) and KOH (a) are presented in FIG. 30. Images shown were recorded after the pre-growth surface treatment of 20 min H_2 etching and 10 min NH_3 annealing. The post-growth annealing of the KOH etched sapphire results in a grainy surface with 3 nm high features. Therefore, this surface that is obtained after the annealing is comparable to as-delivered sapphire surfaces after the same pre-growth annealing since no residual contamination can be found. It should be mentioned that for the KOH-patterned sapphire surfaces, the H_2 etching and NH_3 annealing times can be reduced to 7 min and 4 min, values that are typically used for as-delivered sapphire. In contrast to the KOH patterning, the fabrication process using RIE is expected to have a significant influence on the surface quality of the sapphire, since RIE easily etches the substrate.[173] Accordingly, RIE patterning may cause damage to the surface if the AlN layers are slightly over-etched. As mentioned above, annealing at the high temperatures of 1100–1500°C cannot be used to recover the sapphire surface for the N-polar GaN growth,[123,124] since those high temperatures would affect the state of the AlN nucleation layer.[176] Thus, a non-aggressive smooth patterning with RIE is essential, this being achieved after several etching experiments with low etch rates (as described in Section 2.5.2).
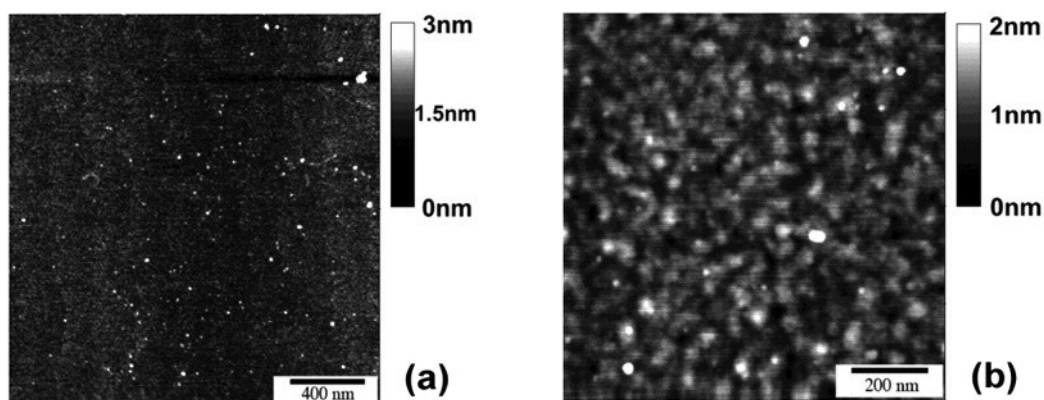
FIG. 30: AFM on sapphire surface after KOH- (a) and RIE-etching (b) and after H$_2$- and NH$_3$- annealing in the MOCVD reactor.

In FIG. 30 (b), a high resolution AFM image of the RIE patterned sapphire is shown. The slow etching requirement and the pre-growth etching with H$_2$ (20 min) and annealing with NH$_3$ (10 min) reveals small features in the height range of 2 nm, similar to a surface after KOH etching and NH$_3$ annealing. However in comparison to the KOH patterned sapphire in FIG. 30 (a), this surface state cannot be achieved with a significantly shorter pre-growth H$_2$ etching and NH$_3$ annealing, indicating that some surface damage by RIE etching is present. However, the longer time H$_2$ etching and NH$_3$ annealing can provide epi-ready surfaces even for RIE patterned templates. Finally, RIE etching may lead to Cl residual amounts on the surface, but XPS measurements (not shown) revealed no kind of contamination on the sapphire surface with chlorine or hydroxide. Therefore, influence of those contaminants that could affect the nucleation of the GaN can be excluded.

FIG. 31 shows the interface quality between the AlN layer and the etched sapphire. The AFM images (FIG. 31 (a) and (b)) of the etched templates show at the interface a step of around 20 nm due to the AlN nucleation layer, suggesting successful etching with KOH and RIE without over-etching into the sapphire substrate. But, a closer look at the interface reveals that the fabrication of the periodically patterned templates using KOH etching causes rough edges on the AlN nucleation layer stripes. This could cause very irregular interfaces between the two domains once the stripes are overgrown with GaN. The RIE patterning in contrast (b) creates very sharp edges on the AlN stripes. An extensive study of KOH etching, varying the KOH solution and the etching time has been done prior to the KOH etching result in FIG. 31 (a). This result can been considered as a typical interface at smooth KOH etching conditions that

has been achieved and represents, therefore, the difficulty of achieving sharp interfaces for templates fabricated with KOH in the μm scale.
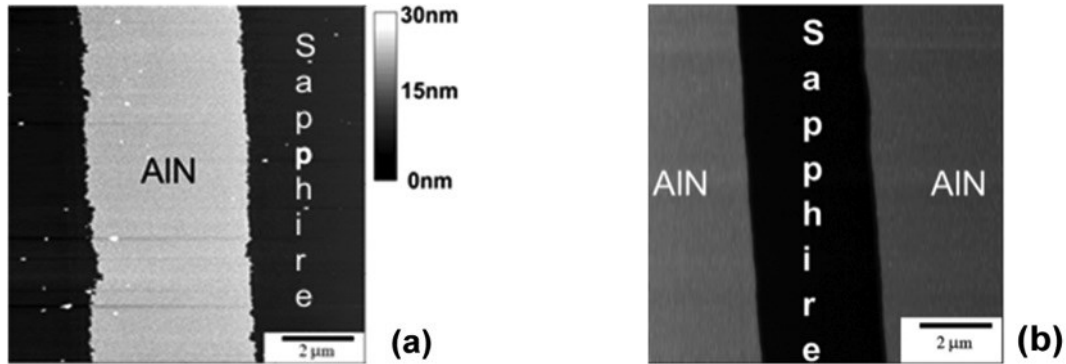
FIG. 31: AFM images of KOH (a) and RIE (b) patterned templates for lateral polar structures (the same AFM scale applies for both pictures).

However, using RIE-based patterning for the template fabrication process, as displayed in FIG. 31 (b), results in high-quality templates with sharp edges at the AlN stripes within the μm scale. This is a remarkable and technologically important observation since the interface sharpness between the N- and Ga-polar GaN domains is critical for efficient SHG conversion. The inversion domain boundary in the final periodically oriented GaN LPS is expected to rely on the initial AlN stripe. The AFM image in FIG. 31 (a) shows that the width of the irregular area in the LT-AlN layer can be estimated to be around 200 nm. This width is on the order of the wavelength of the light that will be used for frequency doubling into the UV-range. Thus, RIE etching is necessary for structures that are designed for optical devices, especially in the UV range.
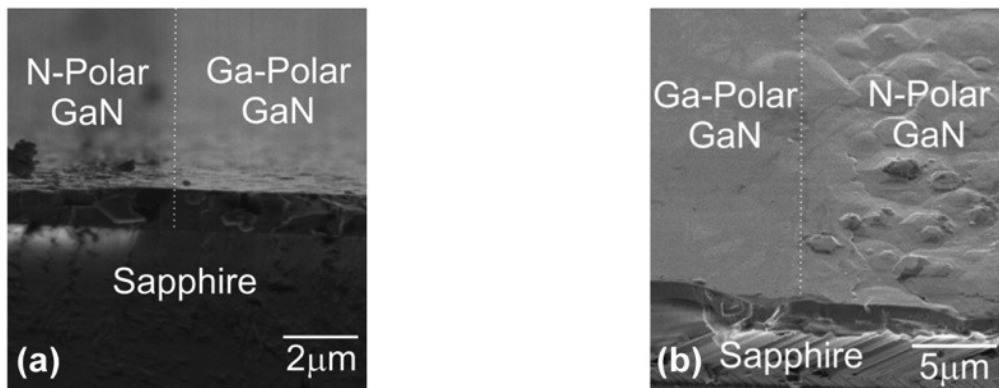
FIG. 32: SEM (60° cross-section) picture of KOH (a) and RIE (b) patterned templates overgrown with GaN.

Following this argument, the KOH- and RIE-patterned templates from FIG. 31 were used to grow a GaN-based LPS. FIG. 32 shows SEM micrographs from the area near the inversion domain between the Ga- and N-polar GaN LPS structure grown on the templates previously described. The KOH-etched template resulted in mixed polarity near the inversion domain boundary region and a rough Ga-polar surface.[168, 178] This is in accordance with the observations in FIG. 31, where an irregular AlN layer interface after KOH etching was shown. Thus, a mixed polarity was predicted close to the inversion domain boundary when overgrown with Ga-polar GaN. Similar observations for GaN on KOH-etched AlN were previously made.[134] In contrast, the Ga-polar domain for the structure grown on the RIE patterned template resulted in a smooth surface while the N-polar domain resulted in the typical hexagonal features[178]. The root mean squared (RMS) roughness, as determined by AFM, was below 1 nm and 12 nm for the Ga-polar and N-polar domains, respectively.
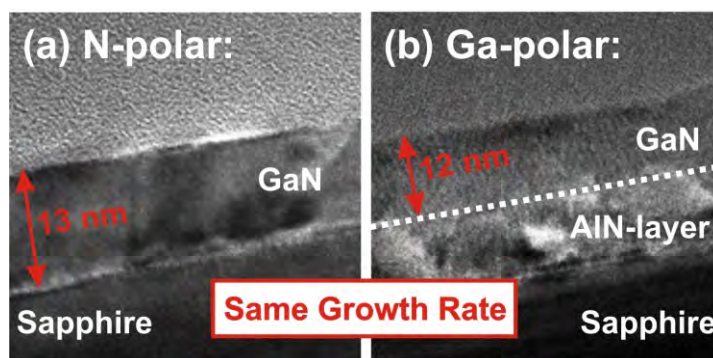
FIG. 33:[c] TEM pictures of thin GaN films. (a) N-polar GaN deposited on sapphire. Previously to the growth, an AlN nucleation layer was removed with RIE. (b) Ga-polar GaN deposited on a 20 nm AlN nucleation layer. The AlN layer was processed following the complete template fabrication procedure. The polarity of the films was confirmed by KOH-etching (see 4.2.2) of additional wafer pieces.

Finally, the influence of the RIE process on the nucleation of N- and Ga-polar GaN domains is investigated. FIG. 33 (a) shows a TEM image from a 13 nm thick N-polar GaN film deposited on sapphire. Prior to growth, the c-sapphire surface was etched with H_2 for 20 min and NH_3 for 10 min. Furthermore, the bare sapphire surface was obtained by RIE etching of a 20 nm AlN nucleation layer, as to simulate the growth of N-polar GaN during the LPS

---

[c] TEM images were taken by Stefan Mohn from the Leibnitz Institute for Crystal Growth Berlin.

processing. Despite the RIE fabrication, the expected growth rate was still achieved on the sapphire surface for the N-polar GaN film. No delay in nucleation was observed as a result of the surface processing in comparison to the Ga-polar GaN film. FIG. 33 (b) corresponds to a Ga-polar film grown simultaneously to the N-polar film but with a 20 nm AlN nucleation layer that has been processed following the same procedure as for a LPS template. The same thickness of 12 nm was observed in the Ga-polar film as for the N-polar film. This indicates that the RIE processing does not lead to the growth rate difference that is observed for GaN LPS. The growth rate difference in a GaN LPS, therefore, might be connected to the side-by-side growth of the domains of opposite polarity within the µm scale, that is, due to the mass transport from one domain to the other.

4.2.2 Influence of Growth Conditions on the Domain Growth Rate in GaN LPSs

As discussed in the previous section, the fabrication is not related to the growth rate differences observed between the N- and Ga-polar GaN domains. Nevertheless, mass conservation is observed (FIG. 28 (c)), when N- and Ga-polar are grown side-by-side in a GaN LPS. It is proposed that the domains height difference is influenced by the growth conditions and mass transport from one domain to the other is expected to occur. In order to validate this hypothesis, the influence of the V/III-ratio on the growth rate is investigated by the change in the NH_3 flow, corresponding to a change in Ga vapor supersaturation. The vapor supersaturation can be defined as the normalized difference in input partial pressure of the species with the equilibrium vapor pressure of species.[62, 179] GaN LPS were grown under the growth conditions explained in Chapter 2.5.2 and the NH_3 flow was adjusted to achieve V/III ratios of 100, 200, and 800. It was observed that the modification of the V/III-ratio had a significant influence on the growth rate of the two domains. In FIG. 34 (a) cross-section SEM images of GaN LPS samples grown under different V/III-ratios are presented. The N-polar regions are marked red and the Ga-polar regions are marked green; a vertical white dashed line denotes the IDB region between the domains. All presented images in (a) are recorded for 10 µm wide domains. FIG. 34 (b) summarizes the observations from the cross-sectional SEM images in (a). The thicknesses of the N- and Ga-polar domains are shown as function of the V/III ratio during growth, as well as the thickness difference between both domains. The

values in (b) are average values of the height of domains. At a V/III ratio of 100, the N- and Ga-polar domains show an average thickness of 0.8 μm and 1.7 μm, respectively. This would suggest a higher growth rate for the Ga-polar domains at this condition. If the V/III ratio is increased to 200, both polar domains have a thickness around 1.2 μm. This value is close to the measured thickness for N- and Ga-polar films grown separately, that is, not in a LPS geometry. Interpolation of the thickness difference in FIG. 34 (b) suggests a zero thickness difference at a V/III-ratio of 225. A further increase in the V/III ratio to 800 leads to a reversal between the domains. In this case, the N-polar domain is dominant with a thickness of ~1.4 μm. This high V/III-ratio is not conducive to growth in the Ga-polar domain. Therefore, the growth rate difference can be reversed between N- and Ga-polar dominated growth depending on the V/III-ratio or implicitly by changing the Ga supersaturation. It should be noted, that in addition to the observation of the thickness difference between N- and Ga-polar domains, the influence of the V/III-ratio on the growth rate of the stripe in orientation parallel and perpendicular to the a-plane was investigated. Nevertheless, the orientation did not affect the growth rates; similar results as those presented in FIG. 34 were found.

The results described in FIG. 34 demonstrate that the V/III ratio can be used to control the layer thicknesses of N- and Ga-polar domains if grown side-by-side in the LPS geometry. The observations indicate that there is no intrinsic growth rate difference between different polarities during the MOCVD growth of GaN as it is proposed in some works.[155, 156] If the film thickness is averaged over the N- and Ga-polar domains, a total growth thickness of 1.1–1.3 μm can be observed, which is near the measured thickness of the Ga- and N-polar GaN layers grown separately on sapphire substrates. Nevertheless, this adds support to the hypothesis that the overall mass of the GaN during deposition is conserved despite the growth rate difference near the IDB, thus suggesting that the films are still grown under the mass transport limited regime.[180] Therefore, mass transport between the N- and Ga-polar domains is expected and dependent on the growth conditions.[181]
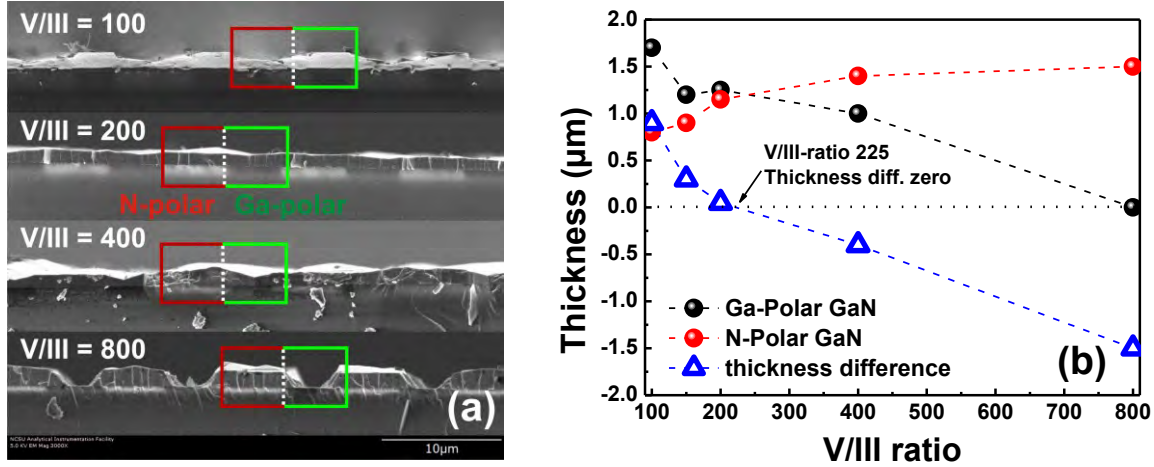
FIG. 34: Influence of the V/III-ration on the growth rate of N-polar and Ga-polar GaN that have been grown side-by-side in a LPS. (a) Cross-sectional SEM images of LPS samples grown with a varying V/III-ratio between 100–800. The white dashed line indicates the IDB. The periodic grating of the samples is 10 μm. (b) Thickness of the Ga-polar and N-polar domains of the LPS close to the IDB. In addition the thickness difference on the applied V/III-ratio between both domains is presented.

Mass transport across a crystal surface is determined by the balance of three different atomic fluxes (FIG. 35): the flux from the vapor to the surface, the flux from the surface back to the vapor due to desorption, and the flux along the surface. In typical MOCVD growth conditions, the III-specie is the limiting reactant, as the V specie is encountered in excess, thus the flux to consider is that of the Ga specie in this particular case. As this growth has been determined to be in the mass transport limited regime, the net flux towards the surface (difference between the flux from vapor to the surface and desorption flux) is equal to the diffusion flux along the surface towards atomic incorporation sites (ie. step edges). One particular length scale that defines this process is the atomic surface diffusion length that directly depends on the activation energies for desorption and diffusion. These energies are surface properties that depend on the crystal polar orientation, as that determines the surface, but does not depend on the growth conditions at constant temperature within the typical processing regime of MOCVD. In this case, the two different polar surfaces are expected to have different corresponding atomic surface diffusion lengths.

The net flux towards the surface is dependent on the vapor supersaturation. The vapor (Ga) supersaturation is directly controlled by the growth conditions (i.e. V/III ratio). On the other hand, the surface diffusion flux is only dependent on the surface adatom concentration gradient. Therefore, the macroscopic mass distribution profile that is determined by the mass transport due to these fluxes is directly dependent on the growth conditions, even at a constant temperature (as the experiments in this section). In other words, this macroscopic mass transport is dependent on growth conditions even though the atomic surface diffusion lengths are only functions of temperature. Nevertheless, a mass transport critical length due to the actual macroscopic mass distribution profile can be defined, as function of growth conditions. This critical length is associated to the macroscopic mass diffusion length, strongly depending on the polar surface, temperature and other growth parameters. In this way, mass transport between the different domains can be controlled by changes in the growth conditions that directly influence the supersaturation.
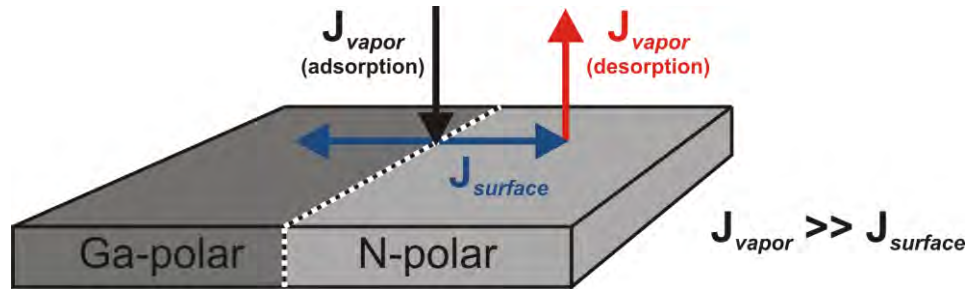
FIG. 35: Conservation of total mass flux. The mass transport across the surface is determined by the balance of: (black) The flux from the vapor to the surface, (blue) the flux along the surface and (red) the flux from the surface back to the vapor due to desorption.

Following this model, the domains with the longest associated critical length will have a negative net mass flux, that is, material will be lost from the domain towards the other domain. This will be evident for LPS with domain sizes within this length scale that is about tens of microns. In typical conditions, the Ga-polar domain will grow thicker than the N-polar domain, even within the mass transport limited regime. Nevertheless, the mass flux could be reversed if the growth conditions are changed to favor one domain over the other, thus finding the possibility of flat structures.
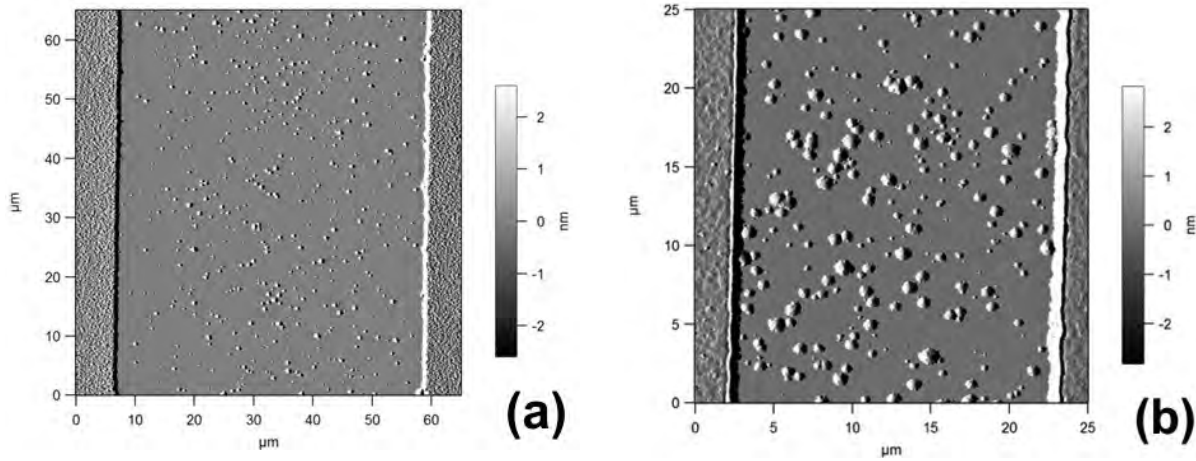
FIG. 36: Atomic force microscopy imaging on 50 μm wide stripes. Especially the N-polar domain (c-sapphire surface) is shown in the center of the images. (a) AFM for a LPS grown with a V/III-ratio of 100. (b) AFM for a LPS grown with a V/III-ratio of 200.

Further investigation to show the influence of the growth conditions (V/III-ratio) on the growth rate of the N-polar domains is presented in FIG. 36. FIG. 36 shows atomic force microscopy imaging on LPS templates that have been overgrown with GaN for 30 seconds to investigate the dependence on the V/III-ratio of GaN nucleation directly on bare sapphire and LT-AlN. In FIG. 36 (a), a 50 μm wide stripe is presented which was recorded in the area of the N-polar domain (sapphire surface). The corners of the image correspond to the Ga-polar domains deposited on the LT-AlN nucleation layers. The sample was grown at a V/III-ratio of 100. The N-polar GaN film is not fully coalesced with small nuclei that can be found on the sapphire surface. The density of the nuclei is higher in the center of the domain away from the IDB to the Ga-polar domain. In contrast, the Ga-polar GaN films in the corners are after 30 seconds of growth fully coalesced. In (b), the same region as in (a) was grown under a V/III-ratio of 200. The size of the nuclei in the N-polar region is larger compared to the nuclei in (a). The growth conditions have, therefore, a significant influence on the nucleation in the N-polar domain where the Ga- and N-polar GaN are grown side-by-side. The higher density of N-polar islands in the center of the stripe suggests the above-mentioned model of mass transport for a polarity dependent critical length that is dependent on the growth condition (V/III-ratio). In this example, the difference between the nucleation surfaces and the corresponding surface energies of the two different domains play a direct role along with the argument previously discussed.
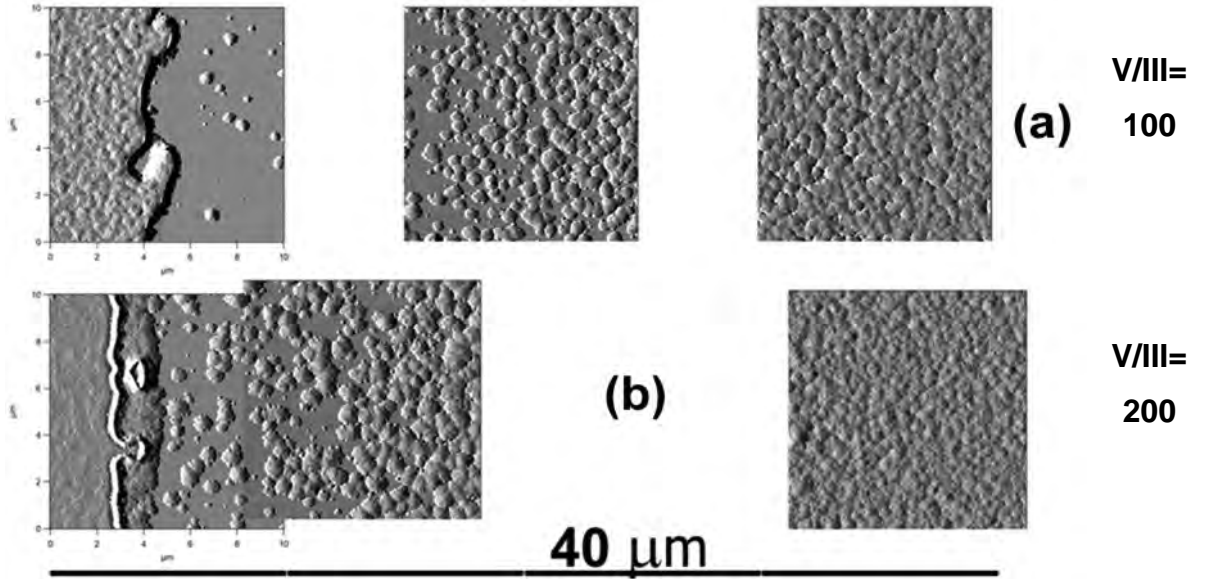
FIG. 37: Atomic force microscopy imaging on 5 mm wide N-polar stripes. AFM pictures have been taken at the IDB presented in the images on the left. In addition images have been taken away from the IDB in the N-polar domain region. The upper 3 AFM images (a) are recorded on a LPS grown at a V/III-ratio of 100. The lower 3 AFM pictures (b) are recorded on a LPS grown at a V/III-ratio of 200. Both samples are GaN LPS grown for 30 seconds.

Nevertheless, the mass transport critical length must be finite. Thus, the nucleation is also investigated on wide (5 mm size) regions of Ga- and N-polar GaN grown side-by-side. FIG. 37 shows three AFM images for the N-polar domain away from the IDB. The images on the left are taken at the IDB. The three images overlap over a distance of ~40 μm away from the IDB. FIG. 37 shows (a) (top three images), a LPS grown at a V/III-ratio of 100 and in (b) (bottom three images) a LPS grown at a V/III-ratio of 200. The AFM image at the IDB for the V/III-ratio of 100 shows a low nuclei density on the sapphire surface close to the IDB. Further away, island growth can be observed (middle top image) and ~30 μm away from the IDB (in right top image) the N-polar film is coalesced. In (b) close to the IDB, a higher nuclei density can be found for a growth at a V/III-ratio of 200. In contrast to (a), in (b) as the distance increases to the IDB a full coalescence film can be found at ~10 μm away from the IDB. These observations suggest that after a certain distance away from the IDB, the N-polar film is coalesced in the same way as the Ga-polar domains are in the corners. After a certain distance away from the IDB, no growth rate difference is observed. A higher V/III-ratio leads to a shorter mass transport critical length.

To verify these observations, the thicknesses of the N- and Ga-polar domains are studied as function of V/III-ratio on large 5 mm domains in a LPS. As suggested from the previous results, the thickness difference between the N- and Ga-polar domains should converge away from the IDB. FIG. 38 shows SEM cross-sectional thickness measurements on the 5 mm domains for samples grown under different V/III ratios as a function of the distance from the IDB. In FIG. 38 (a) a sample grown under a V/III ratio of 100 is shown. The sample shows a 900 nm thickness difference at the IDB for the N-polar domain compared to the Ga-polar domain. As the distance to the IDB increases the thickness of both polarities converges and the height differences decrease until no height difference between the Ga-polar and N-polar domain can be found. For the N-polar domain, a constant thickness around ~1300 nm is reached after around 80 μm. For the Ga-polar domain, this thickness is already reached after 30-40 μm. It should be mentioned that the thickness close to the IDB in the Ga-polar region is above 1700 nm. Since the expected thickness, defined by the growth time under mass transport limited growth conditions, and the thickness away from the IDB is approximately ~1300 nm, we can assume that the increase in material on the Ga-polar domain, close to the IDB, is equal to the missing material on the N-polar domain. This furthers the argument that the growth is within the mass transport limited regime, as the total mass is conserved.

In (b) a sample is shown grown under a V/III ratio of 200. Here a height difference of approximately 50 nm is rapidly reduced within less than 2 μm. If the roughness of the N-polar film is considered, which leads to an increased noise level of the measured thickness in SEM imaging, the sample grown under these conditions can be assumed to be of equal height. For the sample grown under the highest V/III ratio of 800 in FIG. 38 (c), a constant thickness of the N-polar film is already reached after around 80 μm. On the other hand, the Ga-polar domain, despite the steady increase of the thickness, does not reach a constant value even 150 μm away from the IDB. The distance needed to reach equal height between the N- and Ga-polar domains could be interpreted as indicating the mass transport critical length. Thus, for the sample grown under a V/III ratio of 800, a long critical length on the Ga-polar side as compared to a shorter one on the N-polar side is observed. This leads to the lower thickness of Ga-polar GaN close to any inversion domain boundary at high V/III-ratios. In contrast to this, low V/III-ratios lead to longer critical length within the N-polar domains.
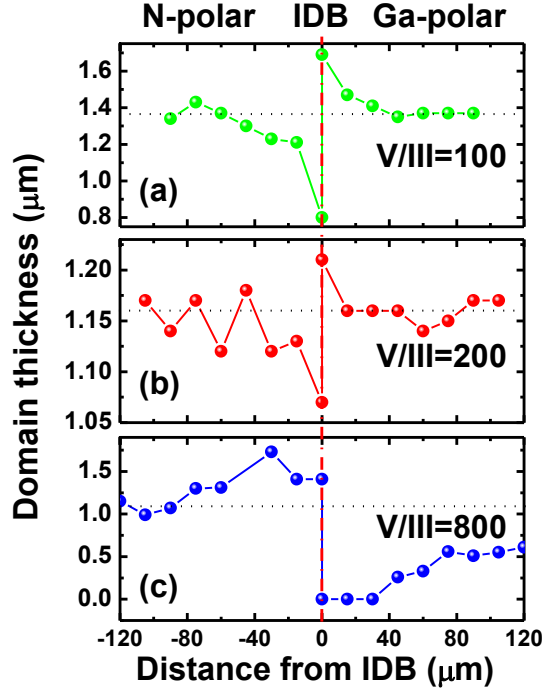
FIG. 38: Growth rate of GaN LPS close the inversion domain boundary as function of the V/III-ratio. (a) V/III-ratio of 100. (b) V/III-ratio of 200. (c) V/III-ratio of 800.

It was demonstrated that the commonly observed height difference between N- and Ga-polar domains grown in proximity is caused by a mass transport between the domains of opposite polarity. It was demonstrated that the commonly observed height difference close to the IDB of such LPS is not attributed to an intrinsic growth rate difference between the N- and Ga-polar domains. The growth difference and the mass transport can be controlled by such simple growth parameters as the V/III ratio, as representing the Ga supersaturation. Results from this work enables the growth of flat LPS for the fabrication of advanced devices.

As a confirmation of the results from this and the previous section and to show the possibility of fabrication of a high-quality GaN LPS grown with MOCVD, FIG. 39 (a) shows a LPS with 10 μm wide stripes grown on an RIE-etched template with a V/III-ratio close to the optimum of 225. The Ga-polar and N-polar stripes are of equal height. The inset in (a), displays an image of a larger area of the stripes as acquired by optical microscopy. It can be clearly observed that the Ga-polar domains are smoother than N-polar domains and the interface is sharp. The smoothness difference is typical for both polarities; the N-polar GaN is expected to

be rougher at the used growth condition and substrate. The microscope image reveals that the stripe structure can be repeated over large distances, making this periodically oriented GaN layer suitable for 2nd harmonic generation experiments as proposed in Chapter 4.1.
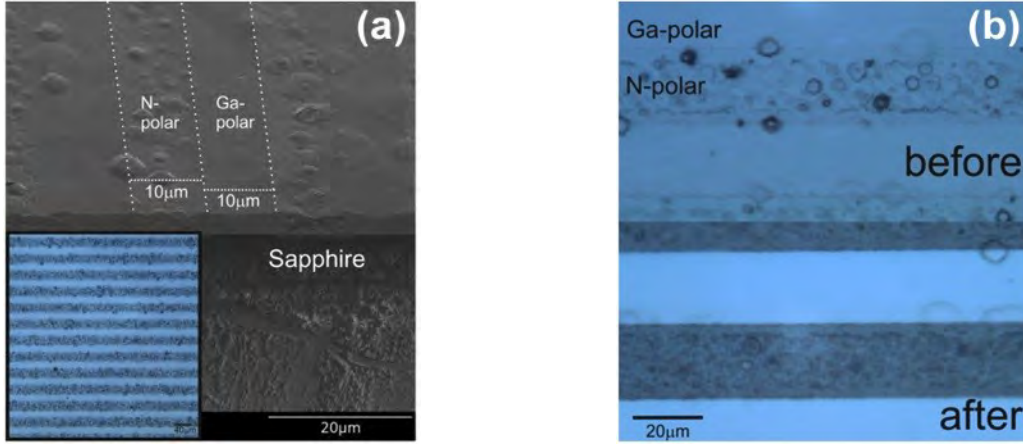
FIG. 39: SEM (60° cross-section) and an optical micrograph (inset) of RIE-etched 10 and 20 μm GaN periodically poled stripe structure (a) and an optical micrograph of a 20 μm GaN stripe structure (b) before and after KOH etching for determination of polarity (top to bottom).

In order to verify the Ga- and N-polarity of the GaN domains and exclude mixed polarity, stripes were wet etched using a 50°C warm 6M KOH solution for 5 min. The etching results are shown in FIG. 39 (b). Before and after the wet etching, the Ga-polar domains have not been changed and stay smooth as expected. In contrast, N-polar domains are significantly etched, indicated by a strong contrast change and smoothing of the surface. This behavior is typical for N-polar GaN as it has a KOH etching rate that is at least two orders of magnitude higher than that of Ga-polar GaN.[182] [183] This smooth etching solution and the short etching time leads to almost no etching dependence on the Ga-polar GaN and high etching on the N-polar GaN. Thus, the expected polarities are demonstrated and no mixed polarity could be found. In addition, resistance measurements reveal for the N-polar domains values of around 60 Ω. The Ga-polar domains in contrast are completely insulating. The origin of the different resistance is the higher oxygen incorporation in the N-polar GaN as compared to Ga-polar GaN making the resistance a good indicator of surface polarity.[22] Therefore, GaN with periodically oriented surface polarity has been grown and the successful growth of stripes with periodicities of 10 μm can be demonstrated that can be used for SHG.

4.3   AlGaN-based LPS

After a detailed discussion of the influence of the fabrication and the growth conditions on the quality of a GaN LPS, the following sections will focus on the influence of the Al content and the growth mode on the quality of AlGaN LPS. The differences between the N- and III-polar domains in AlGaN LPS especially are investigated in terms of the necessary properties for efficient QPM. N-polar AlGaN on sapphire with high Al content is expected to have a smoother surface in comparison to the relative rough N-polar GaN surfaces. This makes AlGaN LPS more favorable since the propagating light would suffer less scattering. Al content AlGaN LPS have advantages in its UV transparency, especially when applied to SHG generation. In addition, thicker AlGaN films can be grown on sapphire when the Al content is low in comparison to pure AlN on sapphire. This is relevant when the wavelength of the propagated fundamental wave is in the dimension of the film thickness.

However, first the influence of alloying GaN with Al in a LPS will be investigated. Here it will be shown that the presence of Ga significantly influences the mass transport between the two polar domains.

Since AlN LPS can be grown without a height difference between the polar domains, the crystal quality of the polar domains will be investigated as the best possible structure for SHG in the UV. A columnar structure of the N-polar domains will be found that arises from a 3D growth mode. Nevertheless it will be concluded that these N-polar domains exhibit a better optical crystal quality then the Al-polar domains.

4.3.1   AlGaN LPS: Domain Height Difference

The influence of the Al composition in AlGaN LPS on the height difference and crystal quality will be investigated to produce AlGaN LPS with smooth surfaces and equal domain height. $Al_xGa_{1-x}N$ LPS have been grown (the fabrication and growth is described in section 2.5.3) with an Al content between x=0.4-1.0. In FIG. 40, two AlGaN LPS are presented; in (a) the LPS has a 70% Al content and in (b) a content of 80%. A periodic structure with sharp interfaces between the two polar domains can be observed. In comparison to a GaN LPS, the surfaces of the N-polar domains are smooth and no hexagons are observed, as it is typical for N-polar GaN (see FIG. 38, Section 4.2.2). For verification of the polarity, the samples have

been etched with (6M solution) KOH at 23°C for 5 min. The sample before etching is displayed in the left and after KOH etching on the right for both (a) and (b). Both samples show that the N-polar region is etched by the KOH, confirming the N-polarity. In contrast, the III-polar domains are not affected by the KOH, indicating III-polarity.

(a) AlGaN: 70% Al   **(b)** AlGaN: 80% Al
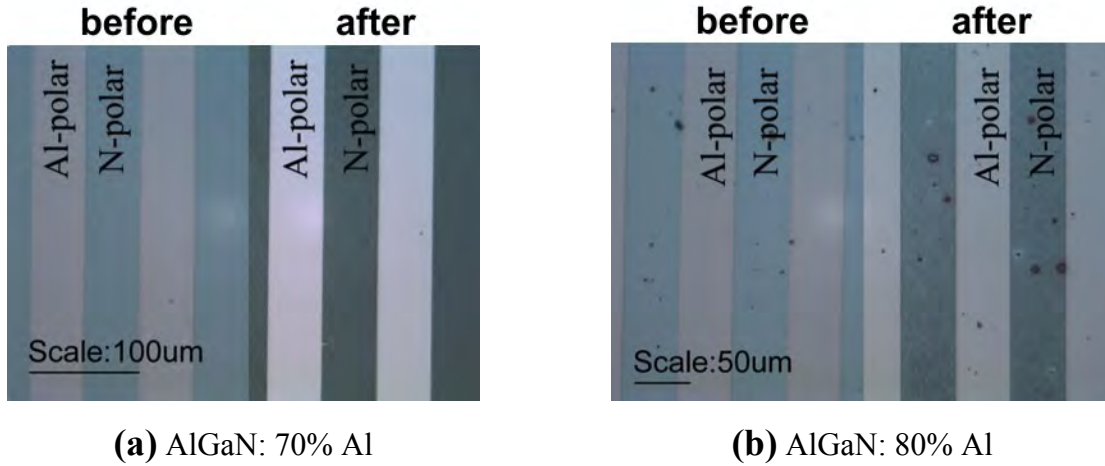
FIG. 40: Microscope images of AlGaN LPS before and after KOH etching determination of polarity. (a) $Al_xGa_{1-x}N$ LPS grown with 0.7 Al content. (b) $Al_xGa_{1-x}N$ LPS grown with 0.8 Al content.

In addition, the AlGaN LPS have been investigated with SEM to confirm any height difference between the polar domains. In FIG. 41 (a) SEM images of $Al_xGa_{1-x}N$ LPS with a varying Al content between x=0.4 - 1.0 are shown. Two major observations can be made from FIG. 40 (a): (1), the surface roughness in the N-polar domains is changed by the Al composition and (2) a height difference between the N- and III-polar domains can be observed, similar to the GaN LPS grown with V/III-ratios below 225. The height difference between the two domains is presented as a function of the Al composition in FIG. 41 (b). The thicknesses of the domains were determined by cross sectional SEM imaging. The height difference between the N- and III-polar domains depends on the Al composition of the films. It has to be noted that the composition change for the AlGaN samples from high to low Al content in FIG. 41 was obtained by increasing the TEG flow, that is, by increasing the Ga content of the alloy. Other growth conditions like temperature, pressure, NH_3 flow, and TMA flow were not changed to achieve the targeted composition. A higher Al content in (b) lead to a smaller height difference and, therefore, no significant mass transport (as discussed in the

previous chapter) from the N-polar domain to the III-polar domain. In other words, by adding more Ga to the alloy the height difference between the domains increases. Cross-sectional SEM micrographs reveal no height difference between the two domains in the AlN LPS (x=1.0). A small difference of 10-30 nm is attributed to the underlying AlN nucleation layer for the III-polar domain. This observation highlights an equal growth rate of Al- and N-polar AlN, which is in contrast to earlier findings in GaN.[168, 178] The AlN LPS will be discussed in detail in the next Section 4.3.2. However, it has to be mentioned that the growth conditions, especially the V/III-ratio, are not changed. Thus, this growth condition by itself does not explain the height difference between the domains. The mass transport towards the III-polar domain depends on the presence of Ga, as AlN LPS do not show any net mass transport towards one of the domains.
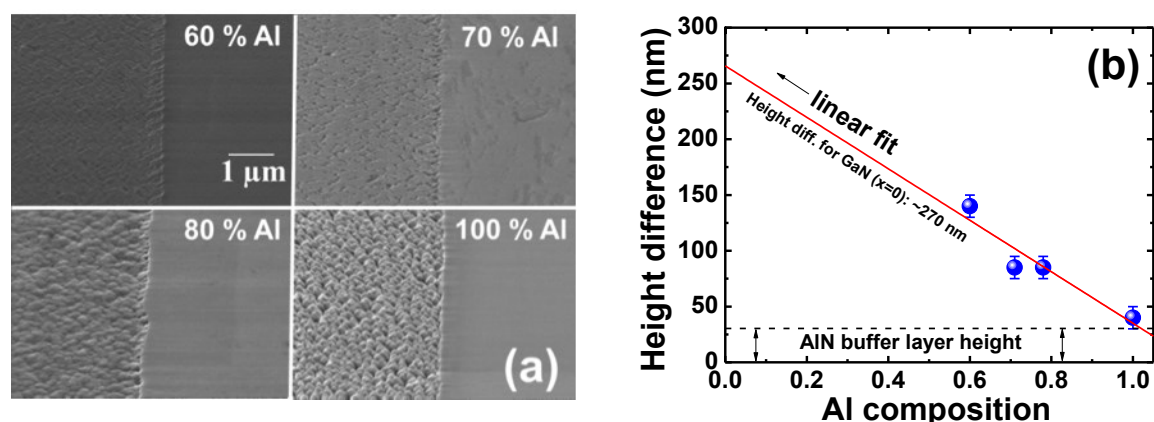
FIG. 41: SEM imaging of AlGaN LPS with varying Al content. (a) SEM pictures at the IDB of AlxGa1-xN LPS with varying Al content between 0.6 – 1.0. (b) Height difference between the N-polar domain and the III-polar domain as function of Al content. The positive height difference indicates a higher growth rate in the III-metal polar domain.

Therefore, it could be expected that for an AlGaN alloy, the domain regions close to the IDB would exhibit a compositional difference. In order to observe this compositional difference, PL and XRD measurements were performed on high Ga content LPS, where an increased composition difference is expected. In FIG. 42 the near band edge PL at 3K on a 50% Al content AlGaN LPS is shown. The free bound exciton (FX_A) can be observed for the N- and III-polar domains. The peaks were identified as free excitons by temperature dependent PL. The PL was measured for the regions close to the IDB.

.
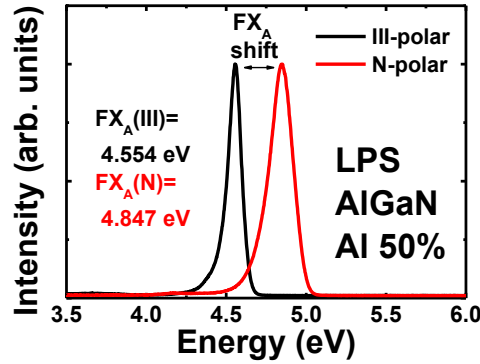
FIG. 42: Photoluminescence at 3K on AlGaN LPS (Al=50%). The position of the free exciton is shifted for the N-polar domain in comparison to the III-polar domain.

The free excitons peak positions of the III- and N-polar domains are considerable shifted against each other in FIG. 42. The free exciton for the III-polar domain is observed at 4.554 eV while the peak position for the N-polar domain is located at 4.847 eV. A variation of 293 meV can be found between the peak positions. In comparison to XRD measurements, such significant strain difference could not be found to explain the significant shift of the PL peaks. The TMA and TEG flow rates were intended for a composition of 50% Al for both domains. From PL, an Al composition of ~47% for the III-polar domain and an Al composition of ~60% for the N-polar domain can be determined. In comparison XRD analysis (not shown), a value of 43% for the III-polar and 55% for the N-polar domain could be observed. Therefore, a significant difference in composition >12% can be seen with higher Al compositions in the N-polar domain. This observation directly suggests that the Ga mass transport from the N-polar domain to the III-polar domain is similar to the one observed on the GaN LPS (Section 4.2.2). Since the Ga mass transport at a given growth condition seems to be towards the III-polar domain a lower Al composition can be found, while the opposite is observed in the N-polar domains.

4.3.2   Characterization of AlN LPS

AlN is a useful material system for optical and electronic applications because of the wide bandgap and its UV applications. Devices have been demonstrated based on Al-polar AlN, since this polar orientation indicates low defect incorporation and increased doping possibility in comparison with N-polarity.[184-186] In addition especially for electronic applications and sensors, the use of N-polar AlN might be also desirable because of low Schottky barrier heights and a low contact resistance.[169, 187] Nevertheless, control of both polarities and growth of AlN polar domains in proximity, like in a LPS, have not been demonstrated. AlN-based LPS are, as mentioned above, useful for UV-laser light conversion via SHG,[8] but in addition a new class of devices like high-power and high-frequency hetero field effect transistors and high-power UV-LEDs could be also fabricated by the use of AlN LPS.[168] In the previous Section 4.3.1, it could be shown that AlN LPS, in comparison to AlGaN LPS, do not show growth rate differences between domains grown in close proximity. The advantage of the use of AlN in comparison to pure GaN for LPSs lies in the transparency of AlN in the deep UV range (~ 200 nm). AlN LPS are beneficial for frequency doubling in the deep UV were GaN cannot be used. It has to be noted that AlN LPS for SHG also allow for wider periodic gratings in comparison to GaN, because of a lower refractive index difference in the UV (see Section 4.1). In the following section AlN LPSs will be characterized for film quality of the domains of opposite polarity and for the sharpness of the IDB between the two domains, since these characteristics can have critical influence on the conversion efficiency of such AlN LPS for SHG, or any other possible device based on an AlN LPS.

However, in FIG. 43 (a) a cross sectional SEM image of an AlN LPS around the IDB is presented. The sample was fabricated and grown in the same manner as the AlGaN LPS discussed in the previous section. The growth and fabrication procedure is similar to the one used for GaN LPS and was described in Section 2.5.3. However, the III-polar layer in FIG. 43 (a) is fully coalesced and exhibits a smooth surface with few defects.[178] This observation is in accordance to results in GaN LPS in Section 4.2.2. In addition, atomic force microscopy on III-polar domains reveal a step flow morphology with root mean square (RMS) values of 0.3 nm on a 5x5 µm area (not shown). In contrast to the III-polar films, the N-polar film in (a) left consists of multiple columnar like structures that are not coalesced near the surface. XRD measurements performed on the N- and Al-polar domains of this sample presented in (a),

reveal a comparable low FWHM of the (002) and (102) peak of 300–400 arcsec and 850 arcsec, respectively. A very low mosaicity of both polarities can be suggested and the columnar structures seem to be well ordered and aligned. Thus, a change of the growth mode can possibly explain the changed layer structure of the N-polar film in comparison to the Al-polar film. Here a two-dimensional growth mode is expected for the Al-polar film while the N-polar AlN would tend to grow in a columnar morphology leading to the observed rough surface in FIG. 43 (a).[188, 189] Nevertheless, the IDB between the Al- and N-polar domains is well defined as shown in FIG. 43 (b). Even for the small stripe size of 5 μm, sharp interfaces and well-defined domains can be produced suggesting that even smaller structures are possible with AlN. This is most important for SHG and conversion into the deep UV, when LPS are uses for frequency doubling. A well-defined periodicity can be seen in FIG. 43 (b).
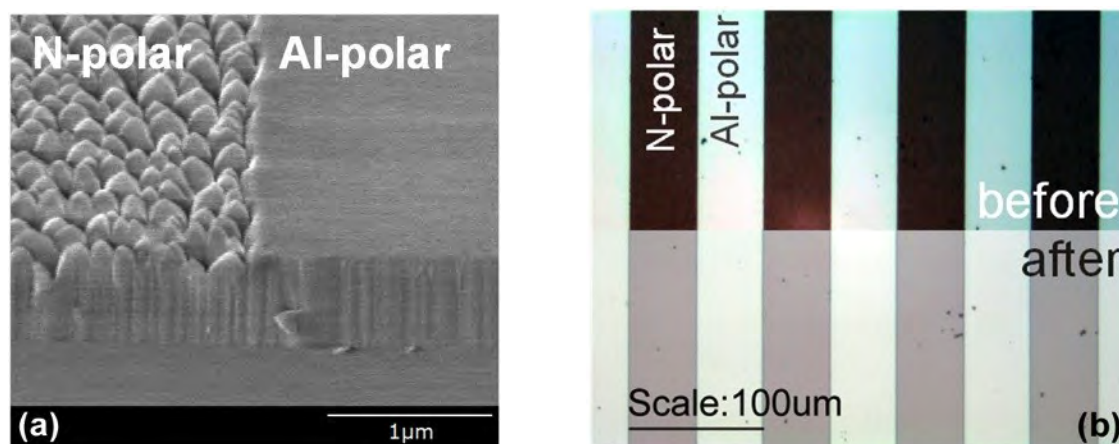
FIG. 43: Characterization of a 600 nm thick AlN LPS at the IDB. (a) SEM image (60° tilted) with domains of N- and III-polarity. (b) Microscope images of AlN LPS before (top) and after (bottom) KOH etching for determination of polarity.

However, in FIG. 43 (b) (6M solution) KOH etching at 70°C for 1 minute was performed for determination of polarity. The etching was performed on 50 μm wide stripes. The top of the image in (b) represents the AlN LPS before the etching and the bottom of the pictures is an AlN LPS that has been wet etched with KOH. No etching can be examined on the Al-polar domains, but the N-polar domains are fully removed by the KOH. This is in agreement with the expected high etch rate of the solution with 1400 nm/min for N-polar AlN versus 2

nm/min for Al-polar AlN. Therefore, this observation proves the expected polarity of the domains and no mixed polarity areas can be found. It should be noted that the darker color for the N-polar domain in the top picture of FIG. 43 (b) is due to the much rougher surface roughness.
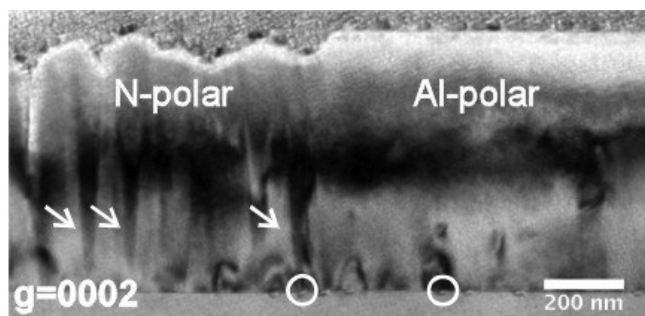
FIG. 44: Bright field TEM image of an AlN LPS at the IDB with the N-polar region on the left and the Al-polar region on the right.

In order to investigate the columnar structures and the quality of the AlN films, a bright field transmission electron microscopy (TEM) measurement was performed on the AlN LPS close to the IDB using a JEOL 2000FX operating at 200 kV. FIG. 44 shows the TEM image of a lateral boundary with a g-vector parallel to the c-axis of the same sample that has been characterized previously by SEM. The above observed columns for the N-polar domain can be observed and it can be determined that the N-polar film is coalesced within the first 300 nm–400 nm. The diameter of the columns can be determined to 100 nm–200 nm. In addition, V-like defects can be observed that are marked in FIG. 44 by white arrows. Jasinski *et al*. and Romano *et al*. identified these V-like defects in AlN and GaN as inversion domains (IDs) by using KOH etching and convergent beam electron diffraction (CBED).[190, 191] This identification could be confirmed by scanning tunneling electron microscopy analysis clearly indicating a polarity change from N-polarity to Al-polarity. In addition, it has to be mentioned that the observed IDs grow under an angle of approximately 4° which is comparable to the angle observed by Jasinski *et al*.[175] The white circles in FIG. 44 indicate voids in the sapphire substrate. The IDs are grown on top of the voids. It should be noted that the sapphire surface is not damaged before the growth of the AlN. The voids seem to form during the growth of the AlN, possible as results of the high growth temperature of 1250ºC. Recently Kumagai *et al*. reported about the origin of those voids in the sapphire as result of decomposition of

sapphire due the high temperatures.[192] Surprisingly, the voids in FIG. 44 found in the Al-polar domain seem to not influence in the Al-polarity and do not cause inversion. Therefore, the void formation seems to favors the Al polarity.

In addition, the dislocation density was determined for the Al-polar and N-polar domains. In both domains a low density of screw-type dislocations could be found and most dislocations are of mixed type. Similar densities of dislocations are found for both polarities of 1×10^{10} cm^2 representing a typical value for Al- and N-polar AlN grown on sapphire that can be found in the literature.[188, 189, 193, 194] In the case of N-polar films, most of the dislocations bend near the sapphire interface leading to a strongly reduced dislocation density at the film surface. In contrast in the Al-polar film, the dislocation bending is not as pronounced. It can be assumed that these different observations arise from different growth modes of the two polar films. The columnar growth mode of in the N-polar domains leads to lower strains as relaxation occurs through surface roughening and 3D-like growth. This is in addition to allowing for dislocation bending near the free surfaces offered by the columnar geometry. XRD and Raman measurements (not shown) confirm the conclusions made from the TEM analysis. The Al-polar domain indicated a compressive strain around 0.6 GPa and the N-polar domain shows a small tensile strain around 0.1 GPa. Due to the large lattice mismatch between AlN and sapphire, the fully coalesced Al-polar layer is highly strained with an increased dislocation density leading to only partial relaxation. In contrast, the N-polar AlN exhibits only a relatively small tensile strain, which is related to the 3D growth.

To compare and investigate the point defects in the Al-polar and N-polar domains, low temperature (5 K) photoluminescence spectra were recorded. The deep defect luminescence is presented in FIG. 45 (a). An intense luminescence can be found for the N-polar film at 3.5 eV, 3.2 eV, and 4.4–4.7 eV which were assigned to silicon, oxygen and Al-vacancies, respectively.[195, 196] This luminescence is an order of magnitude more intense in comparison to the Al-polar AlN film. This suggests that similar to N-polar GaN or InN, an increased point defect incorporation occurs on the anion side in N-polar AlN.[197] However in FIG. 45 (b), the representative spectra of the near band edge luminescence for the two polarity types are shown. Here the N-polar AlN film has three main peaks that can be identified as the free A-exciton (FX$_A$) around 6.034 eV, a silicon-related donor bound exciton (D^{0}X) at 6.012 and their corresponding phonon replicas around 5.92 eV.[198, 199] Temperature dependent

photoluminescence measurements were performed to confirm the assignment as well (not shown). Surprisingly, the free exciton emission is dominating the spectrum even at low temperatures. This is not expected since all excitons are expected to be bound to impurities. Similar observations were made previously for AlN grown on sapphire.[200] In contrast, homoepitaxial grown AlN layers on AlN do not indicate this observation and the bound exciton transitions dominate the spectra. More detailed investigations will be needed in the future to explain this unexpected observation. However, for the Al-polar domains the same emission lines can be observed in (b) as for the N-polar domains. Nevertheless, the peak positions are considerably shifted to higher energies and broadened for the Al-polar film (e.g. X_A from 14.3 meV to 22.3 meV). This suggests a higher optical quality of the N-polar in comparison to the Al-polar domains, since broadening is typically explained by the decreased crystal quality of films. Following results from Pantha *et al.*, the shift to higher energies are consistent with the compressive strain as observed by XRD above.[201]
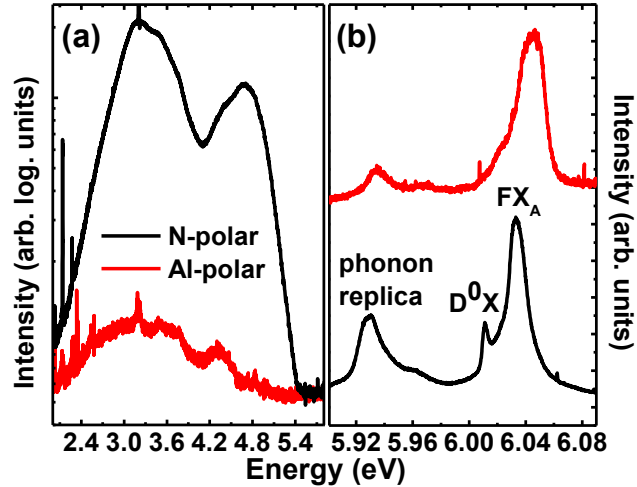
FIG. 45: Photoluminescence at 3K of an AlN LPS. (a) The deep defect luminescence region. (b) The near bandgap free and bound exciton transitions. Note that the y-axis in (a) is in logarithmic scale.

In conclusion, it was demonstrated in this section that AlN LPS could be grown following the typical polarity control scheme as implemented for the growth of GaN LPS. SEM and TEM images revealed a nanocolumn-like appearance of the N-polar domain that is coalesced near the sapphire interface. A 3D-like growth mode for the N-polar films lead to a lowering of the dislocation density, decreased strain and better optical quality in comparison to the Al-polar

films. The results for the AlN LPS will allow for a new class of AlN-based lateral polarity devices similar to those proposed for GaN. A smoother surface for the N-polar domains are desired since the roughness of the N-polar domains leads to scattering effects when the LPS is used for SHG and light is propagated laterally through the structure. Future work will focus on low temperature growth to reduce the void formation and, therefore, decrease the formation of inversion domains. In addition, the effect of temperature on the columnar growth for the N-polar domains should be investigated.

4.4   Summary

The fabrication and growth of AlGaN lateral polar structures was investigated. RIE etching instead of wet etching, was proven to provide for a more efficient fabrication of LPS templates. RIE etching leads to AlN nucleation layers sharp stripes on sapphire at the micrometer range as is needed for sharp inversion domain boundaries. GaN LPS shows a growth rate difference between N- and Ga-polar domains when grown in close proximity. Under typical growth conditions, GaN growth is mass transport limited, thus the growth rate is independent of the polar orientation. It could be shown that the fabrication of templates by etching is not responsible for damage to the surface nor a residual contamination from the fabrication process can be found on the templates before the growth of the LPS. The LPS fabrication process of the templates can, therefore, not be responsible for the growth rate difference of the domains in a GaN LPS. The contradictory observations of a different growth rate of N-polar and Ga-polar GaN in proximity to the separate growth of the polar films could be found to be due to a mass transport between the N-polar and Ga-polar domains that is dependent on the V/III-ratio during the growth. The change of the V/III-ratio can significantly influence the mass transport from one domain to the other and a condition could be found for equal thickness N- and Ga-polar domains. The V/III-ratio change in this experiment was reached by a change in ammonia flow and represents a change in Ga-supersaturation. In AlGaN LPS, the presence of Ga leads to height differences between the polar domains as the ones observed in GaN LPS. Interestingly it could be observed that AlN LPS do not show growth rate differences between domains grown in close proximity. In a series of AlGaN LPS with varying Ga content, the increase of Ga leads to an increase of the height difference between the domains. In addition, an Al composition difference in AlGaN LPS can be found for the polar domains grown in proximity and high Ga content suggesting, as well, the mass transport of Ga. These observations prove that Ga is migrating over a critical length depending on the Ga-supersaturation and the polarity, supporting the hypothesis described in the previous section. Last, the quality of an AlN LPS was investigated. The N-polar domains show a changed growth mode in comparison to the Al-polar domains leading to a nanocolumnar structure, but the film is found to be coalesced. This 3D growth mode of the N-polar domain leads to an increased crystal quality decreased strain.

5. Lateral GaN p/n-junctions Grown under UV Illumination

In this section, the results from Chapter 3, "Point defect control by UV illumination during the growth", and the results from Chapter 4, "Fabrication of high-quality LPS", will be used to highlight a pathway to the fabrication of a more efficient lateral p/n-junction. This should be understood as an example for the application of the point defect control scheme to a device. It will be demonstrated that a reduced compensation can be achieved which make above bandgap illumination during growth a powerful tool.

A lateral polar p/n-junction is another example of a possible application for an LPS despite SHG. A lateral polar p/n-junction consists of a p-type Ga-(or III-) polar domain grown side by side to an n-type N-polar domain. Such structures have been fabricated with MBE or MOCVD.[167, 202, 203] Lateral polar junctions can be used for a variety of applications; they can be used to realize lateral light emitting diodes[22] or for lateral transistors and other optoelectric devices.[204] The general structure of a lateral GaN p/n-junction is presented in FIG. 46 (a).
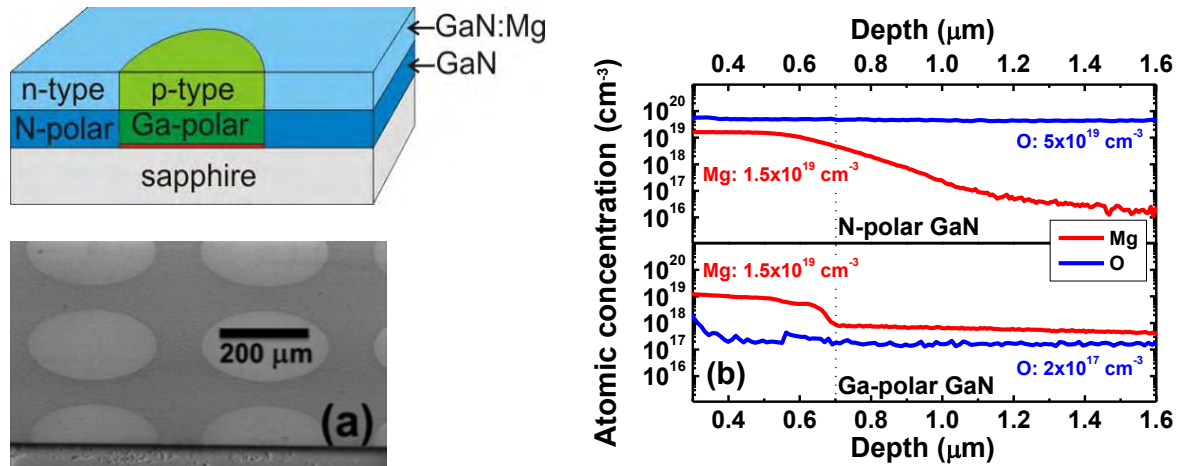

FIG. 46: (a) Structure of an LPS based p/n-junction (N-polar domains are designed as circles). Shown is a schematic and a SEM image of the real structure. (b) SIMS measurements of the Mg and O concentration in the Ga-polar and N-polar domains of a later polar p/n-junction. The data of (b) is published by Collazo et al.[22, 167]

Shown are a schematic and a SEM image of the real structure that has been grown. The fabrication of the displayed lateral polar junction uses the same fabrication processes described in 2.5.2 and in Chapter 4. A different patterning mask was used to achieve circular N-polar domains surrounded by Ga-polar material. A V/III-ratio of 250 was used to achieve N-polar and Ga-polar domains of equal height. The success of the chosen approach can be seen in the SEM image of FIG. 46 (a). No obvious height difference between the N- and Ga-polar GaN is observed, which is confirmed by AFM measurements (not shown). The deposition of GaN was done in two steps. First a 700 nm not intentionally doped GaN film was deposited followed by a 700 nm Mg doped GaN film, as can be seen in the schematic in (a). The Mg doping was performed with a concentration of $1–2\times10^{19}$ cm^{-3}. The lateral polar junction was grown twice, one time with and one time without UV illumination during the growth.

To achieve n-type conductivity side by side to p-type conductivity, the difference in surface energy of the N-polar and Ga-polar GaN is exploited. As a consequence of the difference in chemical reactivity and surface kinetics of the polar surfaces, a different behavior for the incorporation of intentional and unintentional defects can be found.[167] Oxygen especially is found to be an impurity that is incorporated more favorable into N-polar than into Ga-polar GaN. This intrinsic dopant selectivity of the two polar domains for O can be used to achieve p-type and n-type domains side-by-side using a Mg-doped LPS. For illustration, SIMS analysis on N-polar and Ga-polar GaN films doped with Mg is shown in FIG. 46 (b) (these layers were comparable to the p/n junctions described above just with a thicker (1000 nm) undoped GaN layer). The image shows results from the 700 nm thick doped layers in the left and the 1 μm thick undoped GaN layers on the right for N-polarity (top) and Ga-polarity (bottom). In both cases, a Mg concentration of $1–2\times10^{19}$ cm^{-3} for the 700 nm layer can be observed in accordance to the intended Mg doping. Polarity does not influence the incorporation of Mg. In contrast, the oxygen concentration for the N-polar domains is found to be O:5×10^{19} cm^{-3} and O:2×10^{17} cm^{-3} for the Ga-polar domain, independent of the Mg doping. This illustrates the more than two orders of magnitude higher intrinsic incorporation of O into N-polar GaN in comparison to Ga-polar GaN. Thus, in N-polar material, the O concentration is dominating the Mg concentration of 2×10^{19} cm^{-3}. Since O is a shallow donor

in GaN and Mg is considered to be relativity deep (as discussed in Chapter 3) the N-polar domains exhibit n-type conductivity. In the Ga-polar domains, the O concentration is well below that of Mg. Thus, compensation by O is small and the GaN is p-type conductive caused by Mg acceptors. The growth of these Mg doped GaN domains offside by side leads to a lateral polar p/n-junction. The successful growth of such a p/n junction is proven by current rectification, electroluminescence and photo-effect.[22, 167]

In both polar domains, the dopants Mg and O are compensated to a certain level by its counterpart in the N-polar domains 5×10^{19} cm^{-3} of O is compensated by $1-2 \times 10^{19}$ cm^{-3} of Mg, while in the Ga-polar domains $1-2 \times 10^{19}$ cm^{-3} of Mg is compensated by 2×10^{17} cm^{-3} of O. However, it was demonstrated in Chapter 3.3 that UV-illumination during the growth can control the compensation in p-type, as well as in n-type GaN. This concept is expected to work as well for the simultaneously grown n-type and p-type GaN in an LPS based lateral p/n-junction. As it was presented in the previous chapters, the incorporation of donors like O in p-type GaN:Mg, as well as the incorporation of acceptors like Mg in n-type GaN (Chapter 3.3) can be reduced. Thus, these compensators should be incorporated less in a Mg-doped LPS as well as in the Ga- and N-polar domains by the above bandgap illumination during growth leading to improved electrical and optical properties.
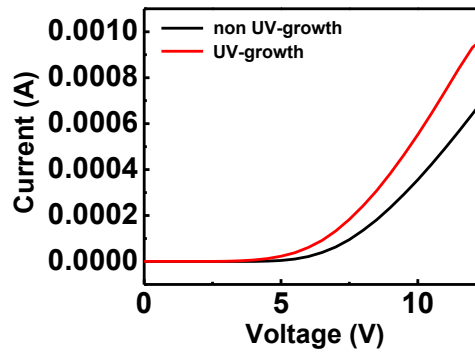
FIG. 47: Current-voltage characteristics (I-V curve) of the lateral p/n-junction grown with and without UV-illumination during growth.

In FIG. 47 the I-V curves of junctions with and without UV illumination are presented. Due to the chosen template each circular structure in FIG. 46 (a) represents one particular p/n junction. The I-V curves in FIG. 47 are obtained from the average of 10 different I-V curves

of different junctions for the case of UV- and non UV-growth. For the case of the UV-grown sample, all 10 measured I-V curves have lower onset voltage in comparison to non UV-grown junctions. Typically, the I-V curve of an UV-grown junction shows a 1-2 V lower onset voltage in comparison to the non UV-grown junction. This observation is a direct consequence of a higher conductivity of the domains (lower resistivity), reached by the reduced incorporation of compensators. It has to be noted that UV-grown junctions were fully activated even without post growth annealing in contrast to the non–UV-grown junctions that had to be activated. This is in agreement with results in Chapter 3.3.2 and the reduced Mg passivation by Mg-H due to the UV-growth.
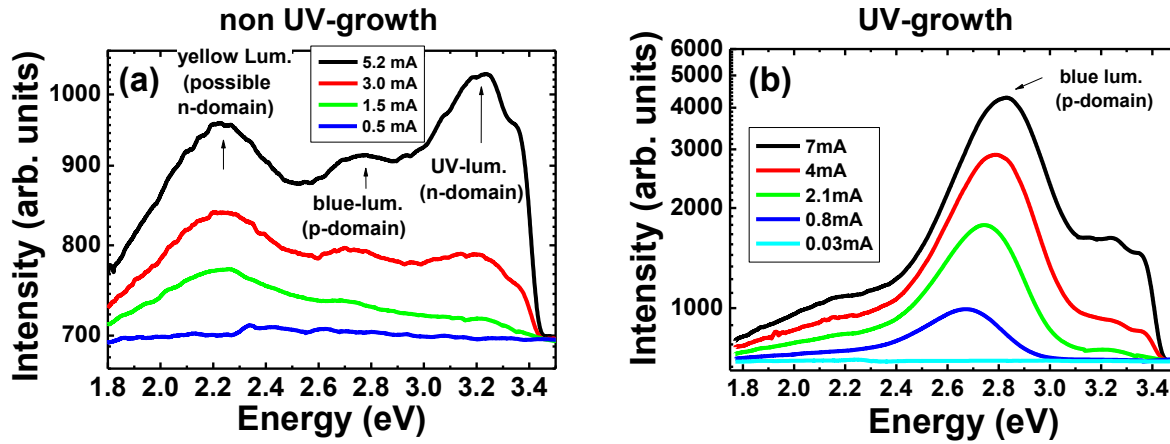
FIG. 48: Electro-luminescence of lateral p/n-junctions using an integrating sphere. (a) EL spectra of a junction without UV-illumination during growth. (b) EL spectra of a junction with UV-illumination during growth. The blue luminescence at 2.85 eV originates from recombination in the p-type Ga-polar GaN domain, while the yellow luminescence at 2.2 eV and UV-luminescence at 3.1-3.4 eV is due to recombination in the n-type N-polar domain.[2, 75, 136]

Further investigation on the effect of the UV growth on the junctions was performed by analyzing the electro-luminescence as presented in FIG. 48. In (a) the EL of lateral polar p/n-junctions are presented (no UV growth). The GaN p/n-junction shows luminescence at 3.1–3.4 and at 2.85 eV. The intensity of these peaks depends on the current that is used for EL. The yellow luminescence at 2.2 eV is possible due to the n-type N-polar GaN domains. As described by Akasaki et al, the luminescence at 3.1–3.4 originates from the transitions in the n-type domain and the luminescence at 2.85 eV is due to a transition in the p-type domain.[75] Since higher carrier concentrations are reached in the n-type N-polar domain than in the p-

type Ga-polar domains, the depletion region is expected to be bigger in the p-type domain in comparison to the n-type domain. As a consequence the p/n-junction recombination of injected holes and electrons is expected to be located in the p-type domain. Therefore, the luminescence at 2.85 eV is the real p/n-junction electro-luminescence of the injected carriers.

The luminescence at 2.85 eV can be observed in FIG. 48 (a) at relatively high currents of >3 mA and more. Still the EL spectra is dominated for all shown currents in (a) by the 3.1–3.4 eV luminescence and the yellow luminescence of the GaN template, stating a relatively poor p/n-junction quality, probably caused by the compensation in both domains.

In contrast, the electro-luminescence of the p/n-junction grown with UV illumination is presented in FIG. 48 (b). The UV illumination leads to an increased intensity of all major peaks by more than one order of magnitude. The luminescence at 2.85 eV is dominating the spectra for all displayed currents. The 3.1–3.4 eV luminescence and the yellow sapphire substrate luminescence is barely observable (notice logarithmic scale). This clearly indicates that the UV-growth has caused a significant change in the compensation stage of the domains leading to an increased the electro-luminescence intensity, especially for the N-polar domain. Therefore, the UV-growth of devices to control compensating point defect and increase the efficiency is proven feasible.

6. Summary and Conclusions

In this thesis, "Polarity Control and Doping in Aluminum Gallium Nitride", two significant and original achievements were demonstrated which are essential for the advancement of AlGaN technology:

(1) The first achievement is the successful development of a point defect control scheme based on Fermi-level management implemented by above bandgap UV illumination that was used to control the formation and incorporation of technologically relevant point defects into n- and p-type semiconductors.

For this achievement, the following measurements and assignments have been made: GaN:Mg was used as a model system to show the effect of UV illumination during growth on the incorporation of compensators of Mg acceptors. In order to understand the effect of UV illumination as a Fermi-level point defect control scheme, the effect of Mg doping on the incorporation of intrinsic and extrinsic point defects, which limit the conductivity of the material, was investigated. The optical transitions in GaN:Mg were analyzed by PL and PLE measurements and three different acceptor states could be found that were assigned to Mg in agreement with theoretical predictions from the literature. In addition, at least two different donors were identified, assigned to O and V_N, which along with the Mg acceptor states, gives rise to the well-known 3.27 eV donor acceptor pair (DAP) transition in PL measurements. The DAP transitions actually consist of a minimum of three different DAP transitions caused by the transition between different acceptor states. The DAP transitions are mainly showing the compensation of Mg mostly by O donors. When GaN:Mg is doped below the self-compensation limit of 2×10^{19} cm^{-3}, the samples are passivated by Mg-H complexes. It could be found that an activation of the samples by annealing led to an increase of a deep Mg acceptor state and that Mg-H complexes were showing no corresponding signature in PL measurements. The dissociation of the complex can be observed indirectly by an increase of acceptor bound excitons in PL, a decrease of the resistivity and by less concentration of H analyzed with SIMS. Above the Mg doping

limit at 2×10^{19} cm^{-3}, it could be shown that V_N donors and V_N-Mg complexes are responsible for the self-compensation in GaN:Mg. The use of UV-above bandgap illumination during the growth of GaN:Mg at any doping concentration significantly decreased the incorporation of point defects, while the Mg concentration was not affected. In the case of doping below the self-compensation limit, the samples grown with above bandgap illumination were fully activated. The PL also indicated full activation, while SIMS measurements showed less H. This observation directly suggested that the decreased incorporation of H during the growth and decreased concentration of Mg-H complexes was caused by the UV illumination. For samples grown with UV illumination above the self-compensation limit, the PL data suggested a significant reduction of V_N-related complexes, which caused the self-compensation. The UV growth led to a decrease of the blue luminescence in PL at 2.85 eV. By performing PLE measurements, less O and V_N donors could also be observed in the transitions. In n-type GaN caused by the intrinsic concentration of O, low Mg doping leads to the compensation of the donors. By applying UV illumination during the growth of such samples, a significant reduction in the incorporation of Mg acceptors was measured. Thus, using GaN:Mg as a model system, it could be proven that above band illumination reduces compensation in n-type, as well as p-type material, as predicted by the our Fermi-level point defect management scheme.

(2) **The second achievement was the successful growth of domains of equal height in AlGaN lateral polar structures. The growth rate difference between Ga- and N-polar GaN domains in a LPS grown in proximity was understood and controlled. It was concluded that the height difference of domains grown side-by-side is due to mass transport between the domains and can be controlled by the Ga supersaturation during the growth.**

For this achievement, the following study has been performed:

The investigation of the fabrication and growth of AlGaN LPS was performed in two major sections. At first GaN LPS were investigated to study the effect of fabrication and growth conditions on the polar structure. The fabrication procedure of templates by etching has no influence on the growth rate difference. Furthermore, the influence of growth conditions, in this case the V/III-ratio, on the growth of GaN LPS was analyzed.

When N- and Ga-polar GaN domains are separately grown (not in proximity), the growth rate and the expected thickness of the films are equal. Domains grown in proximity have shown, independent on the growth condition that the growth is mass transport limited and mass conservation could be observed. Changing the V/III-ratio that corresponds to a change in Ga supersaturation led to a tunable growth rate and thus, a controllable height difference between the two polar domains. Nevertheless, a condition was found such that the domains grew to the same height. These observations could be understood by mass transport between the domains that depended on the growth conditions. By application of these results, a GaN LPS with domains of equal height could be produced.

In a second section, the growth of AlGaN LPS was investigated. Due to the variation of the Ga content in AlGaN LPS, a surface mass transport between the domains has been observed. The higher the Ga content in AlGaN LPS the higher the growth rate difference between the domains. No growth rate difference could be observed for AlN LPS. This suggested the dependence of the Ga mass transport on the Ga supersaturation as the origin of the height difference in AlGaN domains grown in proximity. As a consequence, it could be observed that high Ga content AlGaN LPS suffer from a variation in composition close to the IDB between the III- and N-polar domains. These results strengthen the argument of a mass transport caused by the Ga supersaturation.

As AlN LPS are of great interest for second harmonic generation and could be grown with domains of equal height, a detailed characterization was performed on the structures. In contrast to GaN LPS, a high optical crystal quality could be found for the N-polar domains in comparison to the Al-polar domains. This result was found to be due to a changed 3D growth mode for the N-polar domains, leading in addition to a columnar structure that was coalesced after 200-300 nm from the surface. It is the first demonstration of a AlN lateral polar structure.

The combination of these major achievements was applied to the growth of a lateral polar p/n-junction. Equal height p-type Ga-polar domains in proximity to n-type N-polar domains have been produced. The n-type conductivity and the p-type conductivity is a consequence of a different intrinsic O donor incorporation of Ga- and N-polar GaN. Nevertheless, both domains are doped with Mg while growing these lateral p/n-junctions. Especially, in the n-type N-polar

domains O is partially compensated by Mg. The application of the above bandgap UV illumination during the growth of these junctions can significantly reduce the incorporation of compensators in the corresponding domains, O for the Ga-polar and Mg for the N-polar domain. The result was a significant enhanced electrical efficiency of the junction. The I-V curves of junctions grown with UV illumination indicated a 1-2 volts lower onset (turn-on) voltage. In addition, the electroluminescence of the junction with UV illumination during the growth showed more than an order of magnitude higher intensity in comparison to non UV-grown later polar p/n-junctions.

Finally, it should be noted that although the results of this work are important for a variety of applications, they transcend beyond the proposed applications within this present work. For example, the detailed analysis of GaN:Mg is important since even after p-type conductivity was achieved in the beginning of the nineties the optical transitions and the behavior of Mg in GaN is not fully understood. The clear observation of different acceptor states of Mg gives deeper insight into the GaN:Mg system and Mg as a p-dopant. In addition, the origin of the transitions in GaN:Mg are still controversial. The presented PLE analysis strongly suggests that no neutral Mg-H complex is involved in the DAP transition at 3.27 eV, a discussed alternative explanation for the DAP transitions. Also, the observed transitions in AlN LPS on sapphire and the 3D growth mode in N-polar domains are far-reaching. Achieving high-quality N-polar AlN might be also desirable as it could possibly be used for electronic applications and sensors.

Outstanding is the proved feasibility of a point defect scheme that can control compensators in n-type and p-type semiconductors. This scheme can be applied for other wide bandgap semiconductors where compensation effects limit or even prevent any kind of conductivity.

Future Work

Even more interesting results are expected on the basis of the achievements presented in this present work. Future work is suggested on each topic, as follows:

- Using above bandgap illumination in high Si-doped GaN to reduce the incorporation of C, which limits the free carrier concentration and the mobility. (It should be noted that as part of the present work, preliminary results suggest a decreased C concentration in GaN:Si by UV illumination during growth. A decrease in yellow luminescence at 2.2 eV could be obtained.)

- In high Al content AlGaN or AlN doped with Si or Mg, the compensation is critical. Here the ionization energies of dopants are higher and control of compensation plays a larger role than in GaN.

- The concept could be extended for other wide bandgap semiconductors that suffer from strong compensation, like ZnO.

- AlN and GaN LPS structures can be used to measure second harmonic conversion into the UV. (It should be noted that those measurements that show SHG in LPS structures are ongoing as part of collaboration with the University of Ljubljana, Slovenia. Unfortunately, they could not be finished before the completion of the present work.)

Publications

The following publications are published as part of this thesis:

Papers:

1 **M. P. Hoffmann**, M. Gerhold, R. Kirste, A. Rice, C.-R. Akouala, J. Xie, S. Mita, R Collazo and Z. Sitar; *Fabrication and Characterization of Lateral Polar GaN Structures for Second Harmonic Generation*; Proceedings SPIE; **8631**; 86311T1-86311T9 (2013).

2 R. Kirste, **M. P. Hoffmann**, J. Tweedie, Z. Bryan, G. Callsen, T. Kure, C. Nenstiel, M. R. Wagner, R. Collazo, A. Hoffmann and Z. Sitar; *Compensation effects in GaN:Mg probed by Raman spectroscopy and photoluminescence measurements*; Journal of Applied Physics; **113**; 03504(1)- 03504(5) (2013).

3 Z. Bryan, **M. Hoffmann**, J. Tweedie, R. Kirste, G. Callsen, I. Bryan, A. Rice, M. Bobea, S. Mita, J. Xie, Z. Sitar and R. Collazo; *Fermi-Level Control of Point Defects During Growth of Mg-Doped GaN*; Journal of Electronic Materials; **42** (5), 818-819 (2012).

4 G. Callsen, **M. Hoffmann**, M. R. Wagner, J. Tweedie, T. Kure, Z. Bryan, J. S. Reparaz, S. Aygun, M. Bügler, R. Kirste, J. Brunnmeier, R. Collazo, C. Nenstiel, Z. Sitar and A. Hoffmann; *Optical signature of Mg-doped GaN: Transfer process*; Physical Review B; **86** (7); 075207(1)-075207(14) (2012).

5 M. Rigler, M. Zgonik, **M. P. Hoffmann**, R. Kirste, M. Bobea, R. Collazo, Z. Sitar and M. Gerhold; *Refractive Index of III-metal-polar and N-polar AlGaN waveguides grown by Metal Organic Chemical Vapor Deposition*; Applied Physics Letters; **102** (22), 221106(1)-221106(5) (2013).

6 R. Kirste, L. Hussey, **M. P. Hoffmann**, W. Guo, I. Bryan, Z. Bryan, J. Tweedie, R. Collazo and Z. Sitar; *Polarity control and growth of lateral polarity structures in AlN*; Applied Physics Letters; **102** (18); 181913(1)-181913(4) (2013).

Talks:

1 **M. P. Hoffmann**, Z. Bryan, R. Kirste, J. Rajan, I. Bryan, A. Rice, R. Collazo and Z. Sitar; *Point defect management in Mg doped GaN by Fermi-level control during growth*; European Materials Research Society 2013 Spring Meeting; Strasbourg, France (May 2013).

2 **M. P. Hoffmann**, M. Gerhold, R. Kirste, A. Rice, C.-R. Akouala, J. Xie, S. Mita, R Collazo and Z. Sitar; *Fabrication and Characterization of Lateral Polar GaN Structures for Second Harmonic Generation*; SPIE Photonics West 2013 Spring Meeting; San Francisco, USA (Feb. 2013) *[Invited]*.

3 **M. Hoffmann**, J. Tweedie, R. Collazo, G. Callsen, T. Kure, R. Kirste and Z. Sitar; *A Detailed Photoluminescence study of Photo-assisted Point Defect Control in Magnesium doped GaN*; European Materials Research Society 2011 Spring Meeting; Nice, France (May 2011).

4 **M. Hoffmann**, S. Aygun, J. Tweedie, A. Rice, R. Collazo, G. Callsen, T. Kure, R. Kirste and Z. Sitar; *A Photoluminescence Study of Acceptor Activation in GaN:Mg*; International Workshop on Nitride Semiconductors 2010; Tampa, FL, USA (Sep. 2010).

Poster:

1 **M. P. Hoffmann**, R. Kirste, J. Rajan, J. Xie, S. Mita, M. Gerhold, W. Guo, L. Hussey, I. Bryan, R. Collazo and Z. Sitar; *Influence of the supersaturation on the growth rate of Ga- and N-polar GaN in lateral polar structures*; European Materials Research Society 2013 Spring Meeting; Strasbourg, France (May 2013).

2 **M. Hoffmann**, R. Kirste, L. Hussey, J. Rajan, J. Xie, Z. Bryan, R. Collazo and Z. Sitar; *Growth and Characterization of periodic polar domains for frequency doubling*; Poster Pres.; International Workshop on Nitride Semiconductors 2012; Sapporo, Japan (Oct. 2012).

3 **M. Hoffmann**, C.-R. Akouala, R. Collazo, A. Rice, S. Mita, J. Xie, G. Callsen, M. Gerhold, R. Kirste and Z. Sitar; *Influence of Fabrication on the Quality of Lateral Polar GaN Crystals for Second Harmonic Generation*; Poster Pres.; European Materials Research Society 2011 Spring Meeting; Nice, France (May 2011).

References

1   H. Amano, M. Kito, K. Hiramatsu and I. Akasaki; *P-Type Conduction in Mg-Doped Gan Treated with Low-Energy Electron-Beam Irradiation (LEEBI)*; Japanese Journal of Applied Physics Part 2-Letters **28** (12); L2112-L2114 (1989).

2   S. Nakamura, T. Mukai and M. Senoh; *High-Power Gan P-N-Junction Blue-Light-Emitting Diodes*; Japanese Journal of Applied Physics Part 2-Letters **30** (12A); L1998-L2001 (1991).

3   I. Akasaki and H. Amano; *Breakthroughs in improving crystal quality of GaN and invention of the p-n junction blue-light-emitting diode*; Japanese Journal of Applied Physics Part 1-Regular Papers Brief Communications & Review Papers **45** (12); 9001-9010 (2006).

4   J. Tweedie, R. Collazo, A. Rice, S. Mita, J. Q. Xie, R. C. Akouala and Z. Sitar; *Schottky barrier and interface chemistry for Ni contacted to $Al_{0.8}Ga_{0.2}N$ grown on c-oriented AlN single crystal substrates*; Physica Status Solidi (c) **9** (3-4); 584-587 (2012).

5   Y. Taniyasu, M. Kasu and T. Makimoto; *An aluminium nitride light-emitting diode with a wavelength of 210 nanometres*; Nature **441** (7091); 325-328 (2006).

6   J. P. Zhang, X. H. Hu, A. Lunev, J. Y. Deng, Y. Bilenko, T. M. Katona, M. S. Shur, R. Gaska and M. A. Khan; *AlGaN deep-ultraviolet light-emitting diodes*; Japanese Journal of Applied Physics Part 1-Regular Papers Brief Communications & Review Papers **44** (10); 7250-7253 (2005).

7   A. Zunger; *Practical doping principles*; Applied Physics Letters **83** (1); 57-59 (2003).

8   A. Chowdhury, H. M. Ng, M. Bhardwaj and N. G. Weimann; *Second-harmonic generation in periodically poled GaN*; Applied Physics Letters **83** (6); 1077-1079 (2003).

9   J. Hite, M. Twigg, M. Mastro, J. Freitas, J. Meyer, I. Vurgaftman, S. O'Connor, N. Condon, F. Kub, S. Bowman and C. Eddy; *Development of periodically oriented gallium nitride for non-linear optics*; Optical Materials Express **2** (9); 1203-1208 (2012).

10   G. T. Kiehne, G. K. L. Wong and J. B. Ketterson; *Optical second-harmonic generation in sputter-deposited AlN films*; Journal of Applied Physics **84** (11); 5922-5927 (1998).

11   D. T. Reid; *Engineered quasi-phase-matching for second-harmonic generation*; Journal of Optics a-Pure and Applied Optics **5** (4); S97-S102 (2003).

12   M. Stutzmann, O. Ambacher, M. Eickhoff, U. Karrer, A. L. Pimenta, R. Neuberger, J. Schalwig, R. Dimitrov, P. J. Schuck and R. D. Grober; *Playing with polarity*; Physica Status Solidi B-Basic Research **228** (2); 505-512 (2001).

13   J. S. Tweedie; *X-ray Characterization and Defect Control of III-Nitrides*; Dissertation; North Carolina State University; 2012.

14   M. Kneissl, T. Kolbe, C. Chua, V. Kueller, N. Lobo, J. Stellmach, A. Knauer, H. Rodriguez, S. Einfeldt, Z. Yang, N. M. Johnson and M. Weyers; *Advances in group III-nitride-based deep UV light-emitting diode technology*; Semiconductor Science and Technology **26** (1); 014036 (2011).

15   M. A. Khan, A. Bhattarai, J. N. Kuznia and D. T. Olson; *High-Electron-Mobility Transistor Based on a Gan-Alxga1-Xn Heterojunction*; Applied Physics Letters **63** (9); 1214-1215 (1993).

16   J. Burm, W. J. Schaff, L. F. Eastman, H. Amano and I. Akasaki; *75 angstrom GaN channel modulation doped field effect transistors*; Applied Physics Letters **68** (20); 2849-2851 (1996).

17   F. Bernardini, V. Fiorentini and D. Vanderbilt; *Spontaneous polarization and piezoelectric constants of III-V nitrides*; Physical Review B **56** (16); 10024-10027 (1997).

18   O. Ambacher; *Growth and applications of Group III nitrides*; Journal of Physics D: Applied Physics **31** (20); 2653-2710 (1998).

19   G. Martin, A. Botchkarev, A. Rockett and H. Morkoc; *Valence-band discontinuities of wurtzite GaN, AlN, and InN heterojunctions measured by x-ray photoemission spectroscopy*; Applied Physics Letters **68** (18); 2541-2543 (1996).

20   P. Waltereit, O. Brandt, A. Trampert, H. T. Grahn, J. Menniger, M. Ramsteiner, M. Reiche and K. H. Ploog; *Nitride semiconductors free of electrostatic fields for efficient white light-emitting diodes*; Nature **406** (6798); 865-868 (2000).

21   U. T. Schwarz and M. Kneissl; *Nitride emitters go nonpolar*; physica status solidi (RRL) – Rapid Research Letters **1** (3); A44-A46 (2007).

22   R. Collazo, S. Mita, A. Rice, R. Dalmau, P. Wellenius, J. Muth and Z. Sitar; *Fabrication of a GaN p/n lateral polarity junction by polar doping selectivity*; Physica Status Solidi C - Current Topics in Solid State Physics **5** (6); 1977-1979 (2008).

23   O. Ambacher, J. Smart, J. R. Shealy, N. G. Weimann, K. Chu, M. Murphy, W. J. Schaff, L. F. Eastman, R. Dimitrov, L. Wittmer, M. Stutzmann, W. Rieger and J. Hilsenbeck; *Two-dimensional electron gases induced by spontaneous and piezoelectric polarization charges in N- and Ga-face AlGaN/GaN heterostructures*; Journal of Applied Physics **85** (6); 3222-3233 (1999).

24   S. Lautenschlaeger, J. Sann, N. Volbers, B. K. Meyer, A. Hoffmann, U. Haboeck and M. R. Wagner; *Asymmetry in the excitonic recombinations and impurity incorporation of the two polar faces of homoepitaxially grown ZnO films*; Physical Review B **77** (14); 144108 (2008).

25   N. Dietz, M. Alevli, R. Atalay, G. Durkaya, R. Collazo, J. Tweedie, S. Mita and Z. Sitar; *The influence of substrate polarity on the structural quality of InN layers grown by high-pressure chemical vapor deposition*; Applied Physics Letters **92** (4); 041911-041913 (2008).

26   G. Martin, S. Strite, A. Botchkarev, A. Agarwal, A. Rockett, W. R. L. Lambrecht, B. Segall and H. Morkoc; *Valence-Band Discontinuity between Gan and Aln Measured by X-Ray Photoemission Spectroscopy*; Journal of Electronic Materials **24** (4); 225-227 (1995).

27   M. Feneberg, B. Neuschl, K. Thonke, R. Collazo, A. Rice, Z. Sitar, R. Dalmau, J. Q. Xie, S. Mita and R. Goldhahn; *Sharp bound and free exciton lines from homoepitaxial AlN*; Physica Status Solidi A **208** (7); 1520-1522 (2011).

28   T. Onuma, T. Shibata, K. Kosaka, K. Asai, S. Sumiya, M. Tanaka, T. Sota, A. Uedono and S. F. Chichibu; *Free and bound exciton fine structures in AlN epilayers grown by low-pressure metalorganic vapor phase epitaxy*; Journal of Applied Physics **105** (2); 023529 (2009).

29   H. Ikeda, T. Okamura, K. Matsukawa, T. Sota, M. Sugawara, T. Hoshi, P. Cantu, R. Sharma, J. F. Kaeding, S. Keller, U. K. Mishra, K. Kosaka, K. Asai, S. Sumiya, T. Shibata, M. Tanaka, J. S. Speck, S. P. DenBaars, S. Nakamura, T. Koyama, T. Onuma and S. F. Chichibu; *Impact of strain on free-exciton resonance energies in wurtzite AlN*; Journal of Applied Physics **102** (12); 123707 (2007).

30   B. N. Pantha, N. Nepal, T. M. Al Tahtamouni, M. L. Nakarmi, J. Li, J. Y. Lin and H. X. Jiang; *Correlation between biaxial stress and free exciton transition in AlN epilayers*; Applied Physics Letters **91** (12); 121117 (2007).

31   T. Nishida, T. Ban and N. Kobayashi; *340-350 nm GaN-free UV-LEDs*; Physica Status Solidi a-Applied Research **200** (1); 106-109 (2003).

32   T. Nishida, N. Kobayashi and T. Ban; *GaN-free transparent ultraviolet light-emitting diodes*; Applied Physics Letters **82** (1); 1-3 (2003).

33   V. Adivarahan, S. Wu, J. P. Zhang, A. Chitnis, M. Shatalov, V. Mandavilli, R. Gaska and M. A. Khan; *High-efficiency 269 nm emission deep ultraviolet light-emitting diodes*; Applied Physics Letters **84** (23); 4762-4764 (2004).

34   J. Edmond, A. Abare, M. Bergman, J. Bharathan, K. L. Bunker, D. Emerson, K. Haberern, J. Ibbetson, M. Leung, P. Russel and D. Slater; *High efficiency GaN-based LEDs and lasers on SiC*; Journal of Crystal Growth **272** (1-4); 242-250 (2004).

35   A. Fujioka, T. Misaki, T. Murayama, Y. Narukawa and T. Mukai; *Improvement in Output Power of 280-nm Deep Ultraviolet Light-Emitting Diode by Using AlGaN Multi Quantum Wells*; Applied Physics Express **3** (4) (2010).

36   H. Hirayama, S. Fujikawa, N. Noguchi, J. Norimatsu, T. Takano, K. Tsubaki and N. Kamata; *222-282 nm AlGaN and InAlGaN-based deep-UV LEDs fabricated on high-quality AlN on sapphire*; Physica Status Solidi A-Applications and Materials Science **206** (6); 1176-1182 (2009).

37   H. Hirayama, Y. Tsukada, T. Maeda and N. Kamata; *Marked Enhancement in the Efficiency of Deep-Ultraviolet AlGaN Light-Emitting Diodes by Using a Multiquantum-Barrier Electron Blocking Layer*; Applied Physics Express **3** (3) (2010).

38   A. Khan, K. Balakrishnan and T. Katona; *Ultraviolet light-emitting diodes based on group three nitrides*; Nature Photonics **2** (2); 77-84 (2008).

39   M. Kneissl, Z. H. Yang, M. Teepe, C. Knollenberg, N. M. Johnson, A. Usikov and V. Dmitriev; *Ultraviolet InAlGaN light emitting diodes grown on hydride vapor phase epitaxy AlGaN/sapphire templates*; Japanese Journal of Applied Physics Part 1-Regular Papers Brief Communications & Review Papers **45** (5A); 3905-3908 (2006).

40   H. Tsuzuki, F. Mori, K. Takeda, T. Ichikawa, M. Iwaya, S. Kamiyama, H. Amano, I. Akasaki, H. Yoshida, M. Kuwabara, Y. Yamashita and H. Kan; *High-performance UV emitter grown on high-crystalline-quality AlGaN underlying layer*; Physica Status Solidi a-Applications and Materials Science **206** (6); 1199-1204 (2009).

41   J. P. Zhang, A. Chitnis, V. Adivarahan, S. Wu, V. Mandavilli, R. Pachipulusu, M. Shatalov, G. Simin, J. W. Yang and M. A. Khan; *Milliwatt power deep ultraviolet light-emitting diodes over sapphire with emission at 278 nm*; Applied Physics Letters **81** (26); 4910-4912 (2002).

42   H. Yoshida, Y. Yamashita, M. Kuwabara and H. Kan; *Demonstration of an ultraviolet 336 nm AlGaN multiple-quantum-well laser diode*; Applied Physics Letters **93** (24) (2008).

43   S. J. Xu, W. Liu and M. F. Li; *Direct determination of free exciton binding energy from phonon-assisted luminescence spectra in GaN epilayers*; Applied Physics Letters **81** (16); 2959-2961 (2002).

44   A. K. Viswanath, J. I. Lee, D. Kim, C. R. Lee and J. Y. Leem; *Exciton-phonon interactions, exciton binding energy, and their importance in the realization of room-temperature semiconductor lasers based on GaN*; Physical Review B **58** (24); 16333-16339 (1998).

45   P. Ramvall, S. Tanaka, S. Nomura, P. Riblet and Y. Aoyagi; *Observation of confinement-dependent exciton binding energy of GaN quantum dots*; Applied Physics Letters **73** (8); 1104-1106 (1998).

46   J. F. Muth, J. H. Lee, I. K. Shmagin, R. M. Kolbas, H. C. Casey, B. P. Keller, U. K. Mishra and S. P. DenBaars; *Absorption coefficient, energy gap, exciton binding energy, and recombination lifetime of GaN obtained from transmission measurements*; Applied Physics Letters **71** (18); 2572-2574 (1997).

47   Y. Taniyasu, M. Kasu and T. Makimoto; *Radiation and polarization properties of free-exciton emission from AlN (0001) surface*; Applied Physics Letters **90** (26); 261911 (2007).

48   J. Li, K. B. Nam, M. L. Nakarmi, J. Y. Lin, H. X. Jiang, P. Carrier and S. H. Wei; *Band structure and fundamental optical transitions in wurtzite AlN*; Applied Physics Letters **83** (25); 5163-5165 (2003).

49   J. Li, K. B. Nam, M. L. Nakarmi, J. Y. Lin and H. X. Jiang; *Band-edge photoluminescence of AlN epilayers*; Applied Physics Letters **81** (18); 3365-3367 (2002).

50   G. Dhanaraj, B. Kullaiah, V. Prasad and M. Dudley; *Handbook of Crystal Growth*; 1 ed. (Springer-Verlag, Berlin Heidelberg, 2010).

51   W. K. Burton, N. Cabrera and F. C. Frank; *The Growth of Crystals and the Equilibrium Structure of Their Surfaces*; Philosophical Transactions of the Royal Society of London Series a-Mathematical and Physical Sciences **243** (866); 299-358 (1951).

52   Z. Bryan, M. Hoffmann, J. Tweedie, R. Kirste, G. Callsen, I. Bryan, A. Rice, M. Bobea, S. Mita, J. Xie, Z. Sitar and R. Collazo; *Fermi Level Control of Point Defects During Growth of Mg-Doped GaN*; Journal of Electronic Materials **42** (5); 815-819 (2012).

53   H. W. Jang, S. Y. Kim and J. L. Lee; *Mechanism for Ohmic contact formation of oxidized Ni/Au on p-type GaN*; Journal of Applied Physics **94** (3); 1748-1752 (2003).

54   D. Qiao, L. S. Yu, S. S. Lau, J. Y. Lin, H. X. Jiang and T. E. Haynes; *A study of the Au/Ni ohmic contact on p-GaN*; Journal of Applied Physics **88** (7); 4196-4200 (2000).

55   J. K. Sheu, Y. K. Su, G. C. Chi, W. C. Chen, C. Y. Chen, C. N. Huang, J. M. Hong, Y. C. Yu, C. W. Wang and E. K. Lin; *The effect of thermal annealing on the Ni/Au contact of p-type GaN*; Journal of Applied Physics **83** (6); 3172-3175 (1998).

56   S. Nakamura, T. Mukai, M. Senoh and N. Iwasa; *Thermal Annealing Effects on P-Type Mg-Doped Gan Films*; Japanese Journal of Applied Physics Part 2-Letters **31** (2B); L139-L142 (1992).

57   H. Heinke, V. Kirchner, S. Einfeldt and D. Hommel; *X-ray diffraction analysis of the defect structure in epitaxial GaN*; Applied Physics Letters **77** (14); 2145-2147 (2000).

58   M. A. Moram and M. E. Vickers; *X-ray diffraction of III-nitrides*; Reports on Progress in Physics **72** (3); 036502 (2009).

59   S. Mita, R. Collazo, A. Rice, R. F. Dalmau and Z. Sitar; *Influence of gallium supersaturation on the properties of GaN grown by metalorganic chemical vapor deposition*; Journal of Applied Physics **104** (1); 013521 (2008).

60   S. Mita, R. Collazo and Z. Sitar; *Fabrication of a GaN lateral polarity junction by metalorganic chemical vapor deposition*; Journal of Crystal Growth **311** (10); 3044-3048 (2009).

61   M. Tsuda, K. Watanabe, S. Kamiyama, H. Amano and I. Akasaki; *The surface treatment of sapphire substrate and its effects on the initial stage of GaN growth by MOVPE*; Physica Status Solidi (c) **0** (7); 2163-2166 (2003).

62   S. Mita; *Polarity Control in GaN Epilayers Grown by Metalorganic Chemical Vapor Deposition*; Dissertation; North Carolina State University; 2007.

63   M. J. Kappers, M. A. Moram, D. V. S. Rao, C. McAleese and C. J. Humphreys; *Low dislocation density GaN growth on high-temperature AlN buffer layers on (0001) sapphire*; Journal of Crystal Growth **312** (3); 363-367 (2010).

64   H. Jiang, T. Egawa, M. Hao and Y. Liu; *Reduction of threading dislocations in AlGaN layers grown on AlN/sapphire templates using high-temperature GaN interlayer*; Applied Physics Letters **87** (24); 241911 (2005).

65   Y. Ohba and R. Sato; *Growth of AlN on sapphire substrates by using a thin AlN buffer layer grown two-dimensionally at a very low V/III ratio*; Journal of Crystal Growth **221**; 258-261 (2000).

66   G. C. Yi and B. W. Wessels; *Compensation of n-type GaN*; Applied Physics Letters **69** (20); 3028-3030 (1996).

67   I. Akasaki and H. Amano; *Breakthroughs in Improving Crystal Quality of GaN and Invention of the p-n Junction Blue-Light-Emitting Diode*; Japanese Journal of Applied Physics **45** (12); 9001-9010 (2006).

68   H. Obloh, K. H. Bachem, U. Kaufmann, M. Kunzer, M. Maier, A. Ramakrishnan and P. Schlotter; *Self-compensation in Mg doped p-type GaN grown by MOCVD*; Journal of Crystal Growth **195** (1-4); 270-273 (1998).

69   M. Godlewski, H. Przybylinska, R. Bozek, E. M. Goldys, J. P. Bergman, B. Monemar, I. Grzegory and S. Porowski; *Compensation mechanisms in magnesium doped GaN*; Physica Status Solidi A-Applied Research **201** (2); 216-220 (2004).

70   A. Hoffmann, A. Kaschner and C. Thomsen; *Local vibrational modes and compensation effects in Mg-doped GaN*; Physica Status Solidi (c) **0** (6); 1783-1794 (2003).

71   M. A. Reshchikov and H. Morkoc; *Luminescence properties of defects in GaN*; Journal of Applied Physics **97** (6); 061301 (2005).

72   B. Monemar, P. P. Paskov, G. Pozina, C. Hemmingsson, J. P. Bergman, T. Kawashima, H. Amano, I. Akasaki, T. Paskova, S. Figge, D. Hommel and A. Usui; *Evidence for Two Mg Related Acceptors in GaN*; Physical Review Letters **102** (23); 235501 (2009).

73   S. Lany and A. Zunger; *Dual nature of acceptors in GaN and ZnO: The curious case of the shallow Mg-Ga deep state*; Applied Physics Letters **96** (14); 142114 (2010).

74   W. Gotz, N. M. Johnson, D. P. Bour, M. D. McCluskey and E. E. Haller; *Local vibrational modes of the Mg-H acceptor complex in GaN*; Applied Physics Letters **69** (24); 3725-3727 (1996).

75   I. Akasaki, H. Amano, M. Kito and K. Hiramatsu; *Photoluminescence of Mg-Doped P-Type Gan and Electroluminescence of Gan P-N-Junction LED*; Journal of Luminescence **48-9**; 666-670 (1991).

76   W. Gotz, N. M. Johnson, J. Walker, D. P. Bour and R. A. Street; *Activation of acceptors in Mg-doped GaN grown by metalorganic chemical vapor deposition*; Applied Physics Letters **68** (5); 667-669 (1996).

77   K. S. Ahn, D. J. Kim, Y. T. Moon, H. G. Kim and S. J. Park; *Effects of a two-step rapid thermal annealing process on Mg-doped p-type GaN films grown by metalorganic chemical vapor deposition*; Journal of Vacuum Science & Technology B **19** (1); 215-218 (2001).

78   Y. Koide, D. E. Walker, B. D. White, L. J. Brillson, M. Murakami, S. Kamiyama, H. Amano and I. Akasaki; *Simultaneous observation of luminescence and dissociation processes of Mg-H complex for Mg-doped GaN*; Journal of Applied Physics **92** (7); 3657-3661 (2002).

79   O. Gelhausen, M. R. Phillips, E. M. Goldys, T. Paskova, B. Monemar, M. Strassburg and A. Hoffmann; *Dissociation of H-related defect complexes in Mg-doped GaN*; Physical Review B **69** (12); 125210 (2004).

80   H. Alves, F. Leiter, D. Pfisterer, D. M. Hofmann, B. K. Meyer, S. Einfeld, H. Heinke and D. Hommel; *Mg in GaN: the structure of the acceptor and the electrical activity*; physica status solidi (c) **0** (6); 1770-1782 (2003).

81   W. Gotz, N. M. Johnson and D. P. Bour; *Deep level defects in Mg-doped, p-type GaN grown by metalorganic chemical vapor deposition*; Applied Physics Letters **68** (24); 3470-3472 (1996).

82   C. G. Van de Walle and J. Neugebauer; *First-principles calculations for defects and impurities: Applications to III-nitrides*; Journal of Applied Physics **95** (8); 3851-3879 (2004).

83   U. Kaufmann, P. Schlotter, H. Obloh, K. Kohler and M. Maier; *Hole conductivity and compensation in epitaxial GaN : Mg layers*; Physical Review B **62** (16); 10867-10872 (2000).

84   U. Kaufmann, M. Kunzer, M. Maier, H. Obloh, A. Ramakrishnan, B. Santic and P. Schlotter; *Nature of the 2.8 eV photoluminescence band in Mg doped GaN*; Applied Physics Letters **72** (11); 1326-1328 (1998).

85   Z. Liliental-Weber, J. Jasinski, M. Benamara, I. Grzegory, S. Porowski, D. J. H. Lampert, C. J. Eiting and R. D. Dupuis; *Influence of dopants on defect formation in GaN*; Physica Status Solidi B-Basic Research **228** (2); 345-352 (2001).

86   G. Callsen, M. R. Wagner, T. Kure, J. S. Reparaz, M. Bügler, J. Brunnmeier, C. Nenstiel, A. Hoffmann, M. Hoffmann, J. Tweedie, Z. Bryan, S. Aygun, R. Kirste, R. Collazo and Z. Sitar; *Optical signature of Mg-doped GaN: Transfer processes*; Physical Review B **86** (7); 075207 (2012).

87   B. Monemar, P. P. Paskov, J. P. Bergman, A. A. Toropov, T. V. Shubina, S. Figge, T. Paskova, D. Hommel, A. Usui, M. Iwaya, S. Kamiyama, H. Amano and I. Akasaki; *Optical signatures of dopants in GaN*; Materials Science in Semiconductor Processing **9** (1-3); 168-174 (2006).

88   B. Gil, P. Bigenwald, P. P. Paskov and B. Monemar; *Internal structure of acceptor-bound excitons in wide-band-gap wurtzite semiconductors*; Physical Review B **81** (8); 085211 (2010).

89   B. Monemar, P. Paskov, G. Pozina, C. Hemmingsson, P. Bergman, D. Lindgren, L. Samuelson, X. F. Ni, H. Morkoc, T. Paskova, Z. X. Bi and J. Ohlsson; *Photoluminescence of Mg-doped m-plane GaN grown by MOCVD on bulk GaN substrates*; Physica Status Solidi a-Applications and Materials Science **208** (7); 1532-1534 (2011).

90   A. M. Fischer, S. Srinivasan, F. A. Ponce, B. Monemar, F. Bertram and J. Christen; *Time-resolved cathodoluminescence of Mg-doped GaN*; Applied Physics Letters **93** (15); 151901 (2008).

91   H. Teisseyre, T. Suski, P. Perlin, I. Grzegory, M. Leszczynski, M. Bockowski, S. Porowski, J. A. Freitas, R. L. Henry, A. E. Wickenden and D. D. Koleske; *Different character of the donor-acceptor pair-related 3.27 eV band and blue photoluminescence in Mg-doped GaN. Hydrostatic pressure studies*; Physical Review B **62** (15); 10151-10157 (2000).

92   G. Pozina, P. P. Paskov, J. P. Bergman, C. Hemmingsson, L. Hultman, B. Monemar, H. Amano, I. Akasaki and A. Usui; *Metastable behavior of the UV luminescence in Mg-doped GaN layers grown on quasibulk GaN templates*; Applied Physics Letters **91** (22); 221901 (2007).

93   U. Kaufmann, M. Kunzer, H. Obloh, M. Maier, C. Manz, A. Ramakrishnan and B. Santic; *Origin of defect-related photoluminescence bands in doped and nominally undoped GaN*; Physical Review B **59** (8); 5561-5567 (1999).

94   A. R. Goni, H. Siegle, K. Syassen, C. Thomsen and J. M. Wagner; *Effect of pressure on optical phonon modes and transverse effective charges in GaN and AlN*; Physical Review B **64** (3); 035205 (2001).

95   G. Callsen, J. S. Reparaz, M. R. Wagner, R. Kirste, C. Nenstiel, A. Hoffmann and M. R. Phillips; *Phonon deformation potentials in wurtzite GaN and ZnO determined by uniaxial pressure dependent Raman measurements*; Applied Physics Letters **98** (6); 061906 (2011).

96   D. G. Thomas, J. J. Hopfield and Augustyn.Wm; *Kinetics of Radiative Recombination at Randomly Distributed Donors and Acceptors*; Physical Review **140** (1A); A202-A220 (1965).

97   S. Fischer, C. Wetzel, E. E. Haller and B. K. Meyer; *On P-Type Doping in Gan-Acceptor Binding-Energies*; Applied Physics Letters **67** (9); 1298-1300 (1995).

98   B. K. Meyer, D. Volm, A. Graber, H. C. Alt, T. Detchprohm, A. Amano and I. Akasaki; *Shallow Donors in Gan - the Binding-Energy and the Electron Effective-Mass*; Solid State Communications **95** (9); 597-600 (1995).

99   J. R. Haynes; *Experimental Proof of the Existence of a New Electronic Complex in Silicon*; Physical Review Letters **4** (7); 361-363 (1960).

100   B. K. Meyer; *Free and bound excitons in GaN epitaxial films*; Materials Research Society Proceedings **449**; 497-507 (1997).

101   B. Monemar; *Bound excitons in GaN*; Journal of Physics-Condensed Matter **13** (32); 7011-7026 (2001).

102   S. Lany and A. Zunger; *Polaronic hole localization and multiple hole binding of acceptors in oxide wide-gap semiconductors*; Physical Review B **80** (8); 085202 (2009).

103   C. Merz, M. Kunzer, U. Kaufmann, I. Akasaki and H. Amano; *Free and bound excitons in thin wurtzite GaN layers on sapphire*; Semiconductor Science and Technology **11** (5); 712-716 (1996).

104   G. Pozina, C. Hemmingsson, P. P. Paskov, J. P. Bergman, B. Monemar, T. Kawashima, H. Amano, I. Akasaki and A. Usui; *Effect of annealing on metastable shallow acceptors in Mg-doped GaN layers grown on GaN substrates*; Applied Physics Letters **92** (15); 151904 (2008).

105   Y. Kamiura, Y. Yamashita and S. Nakamura; *Photo-enhanced activation of hydrogen-passivated magnesium in p-type GaN films*; Japanese Journal of Applied Physics Part 2-Letters **37** (8B); L970-L971 (1998).

106   Q. Yang, H. Feick and E. R. Weber; *Observation of a hydrogenic donor in the luminescence of electron-irradiated GaN*; Applied Physics Letters **82** (18); 3002-3004 (2003).

107   D. G. Chtchekine, Z. C. Feng, G. D. Gilliland, S. J. Chua and D. Wolford; *Donor-hydrogen bound exciton in epitaxial GaN*; Physical Review B **60** (23); 15980-15984 (1999).

108   A. Castiglia, J. F. Carlin and N. Grandjean; *Role of stable and metastable Mg-H complexes in p-type GaN for cw blue laser diodes*; Applied Physics Letters **98** (21); 213505 (2011).

109   C. Bungaro, K. Rapcewicz and J. Bernholc; *Surface sensitivity of impurity incorporation: Mg at GaN (0001) surfaces*; Physical Review B **59** (15); 9771-9774 (1999).

110   G. F. Neumark; *Are Impurities the Cause of Self-Compensation in Large-Band-Gap Semiconductors*; Journal of Applied Physics **51** (6); 3383-3387 (1980).

111   G. Mandel; *Self-Compensation Limited Conductivity in Binary Semiconductors .1. Theory*; Physical Review a-General Physics **134** (4A); 1073-1079 (1964).

112   D. C. Look, K. D. Leedy, L. Vines, B. G. Svensson, A. Zubiaga, F. Tuomisto, D. R. Doutt and L. J. Brillson; *Self-compensation in semiconductors: The Zn vacancy in Ga-doped ZnO*; Physical Review B **84** (11); 115202 (2011).

113   H. Alves, M. Bohm, A. Hofstaetter, H. Amano, S. Einfeldt, D. Hommel, D. M. Hofmann and B. K. Meyer; *Compensation mechanism in MOCVD and MBE grown GaN : Mg*; Physica B-Condensed Matter **308**; 38-41 (2001).

114   L. T. Romano, M. Kneissl, J. E. Northrup, C. G. Van de Walle and D. W. Treat; *Influence of microstructure on the carrier concentration of Mg-doped GaN films*; Applied Physics Letters **79** (17); 2734-2736 (2001).

115   D. Iida, K. Tamura, M. Iwaya, S. Kamiyama, H. Amano and I. Akasaki; *Compensation effect of Mg-doped a- and c-plane GaN films grown by metalorganic vapor phase epitaxy*; Journal of Crystal Growth **312** (21); 3131-3135 (2010).

116   D. O. Demchenko, I. C. Diallo and M. A. Reshchikov; *Yellow Luminescence of Gallium Nitride Generated by Carbon Defect Complexes*; Physical Review Letters **110** (8); 087404 (2013).

117   M. A. Reshchikov, J. D. McNamara, S. Fernández-Garrido and R. Calarco; *Tunable thermal quenching of photoluminescence in Mg-doped p-type GaN*; Physical Review B **87** (11); 115205 (2013).

118   L. Eckey, U. von Gfug, J. Holst, A. Hoffmann, A. Kaschner, H. Siegle, C. Thomsen, B. Schineller, K. Heime, M. Heuken, O. Schon and R. Beccard; *Photoluminescence and Raman study of compensation effects in Mg-doped GaN epilayers*; Journal of Applied Physics **84** (10); 5828-5830 (1998).

119   B. Z. Qu, Q. S. Zhu, X. H. Sun, S. K. Wan, Z. G. Wang, H. Nagai, Y. Kawaguchi, K. Hiramatsu and N. Sawaki; *Photoluminescence of Mg-doped GaN grown by metalorganic chemical vapor deposition*; Journal of Vacuum Science & Technology A **21** (4); 838-841 (2003).

120   M. A. Reshchikov, G. C. Yi and B. W. Wessels; *Behavior of 2.8-and 3.2-eV photoluminescence bands in Mg-doped GaN at different temperatures and excitation densities*; Physical Review B **59** (20); 13176-13183 (1999).

121   F. Shahedipour and B. W. Wessels; *Investigation of the formation of the 2.8 eV luminescence band in p-type GaN:Mg*; Applied Physics Letters **76** (21); 3011-3013 (2000).

122   M. Kuball; *Raman spectroscopy of GaN, AlGaN and AlN for process and growth monitoring/control*; Surface and Interface Analysis **31** (10); 987-999 (2001).

123   L. Filippidis, H. Siegle, A. Hoffmann, C. Thomsen, K. Karch and F. Bechstedt; *Raman frequencies and angular dispersion of polar modes in aluminum nitride and gallium nitride*; Physica Status Solidi B-Basic Research **198** (2); 621-627 (1996).

124   L. Eckey, U. Von Gfug, J. Holst, A. Hoffmann, B. Schineller, K. Heime, M. Heuken, O. Schon and R. Beccard; *Compensation effects in Mg-doped GaN epilayers*; Journal of Crystal Growth **189**; 523-527 (1998).

125   J. K. Kung and W. G. Spitzer; *Determination of Fermi-Level Effect on Si-site Distribution in GaAs:Si*; Journal of Applied Physics **45** (5); 2254-2257 (1974).

126   S. Yu, U. M. Gosele and T. Y. Tan; *A Model of Si Diffusion in GaAs Based on the Effect of the Fermi Level*; Journal of Applied Physics **66** (7); 2952-2961 (1989).

127   J. Q. Xie, S. Mita, R. Collazo, A. Rice, J. Tweedie and Z. Sitar; *Fermi level effect on strain of Si doped GaN*; Proceedings of SPIE **7939**; 79390B (2011).

128   J. Q. Xie, S. Mita, A. Rice, J. Tweedie, L. Hussey, R. Collazo and Z. Sitar; *Strain in Si doped GaN and the Fermi level effect*; Applied Physics Letters **98** (20); 202101 (2011).

129   H. Gerischer; *The Impact of Semiconductors on the Concepts of Electrochemistry*; Electrochimica Acta **35** (11-12); 1677-1699 (1990).

130   Y. Kamiura, Y. Yamashita and S. Nakamura; *Photo-enhanced dissociation of hydrogen-magnesium complexes in gallium nitride*; Physica B-Condensed Matter **273-4**; 54-57 (1999).

131   Y. Nakagawa, M. Haraguchi, M. Fukui, S. Tanaka, A. Sakaki, K. Kususe, N. Hosokawa, T. Takehara, Y. Morioka, H. Iijima, M. Kubota, M. Abe, T. Mukai, H. Takagi and G. Shinomiya; *Hydrogen dissociation from Mg-doped GaN*; Japanese Journal of Applied Physics Part 1-Regular Papers Brief Communications & Review Papers **43** (1); 23-29 (2004).

132   S. Nakamura, M. Senoh and T. Mukai; *Highly P-Typed Mg-Doped Gan Films Grown with Gan Buffer Layers*; Japanese Journal of Applied Physics Part 2-Letters **30** (10A); L1708-L1711 (1991).

133   R. Katayama, Y. Kuge, T. Kondo and K. Onabe; *Fabrication of lateral lattice-polarity-inverted GaN heterostructure*; Journal of Crystal Growth **301**; 447-451 (2007).

134   Y. Fukuhara, R. Katayama and K. Onabe; *Lateral patterning of GaN polarity using wet etching process*; Physica Status Solidi C: Current Topics in Solid State Physics **7** (7-8); 1922-1924 (2010).

135   R. Katayama, Y. Fukuhara, M. Kakuda, S. Kuboya, K. Onabe, S. Kurokawa, N. Fujii and T. Matsuoka; *Optical properties of the periodic polarity-inverted GaN waveguides*; Proceedings of SPIE **8268**; 826814 (2012).

136   R. Kirste, R. Collazo, G. Callsen, M. R. Wagner, T. Kure, J. S. Reparaz, S. Mita, J. Q. Xie, A. Rice, J. Tweedie, Z. Sitar and A. Hoffmann; *Temperature dependent photoluminescence of lateral polarity junctions of metal organic chemical vapor deposition grown GaN*; Journal of Applied Physics **110** (9); 093503 (2011).

137   A. P. Lima, C. Miskys, O. Ambacher, M. Stutzmann, P. Dimitrov, V. Tilak, M. J. Murphy and L. F. Eastman; *AlGaN/GaN lateral polarity heterostructures*; Proceedings of the 25th International Conference on the Physics of Semiconductors **87**; 303-304 (2001).

138   L. Nevou, M. Tchernycheva, F. Julien, M. Raybaut, A. Godard, E. Rosencher, F. Guillot and E. Monroy; *Intersubband resonant enhancement of second-harmonic generation in GaN/AlN quantum wells*; Applied Physics Letters **89** (15); 151101 (2006).

139   D. N. Hahn, G. T. Kiehne, J. B. Ketterson, G. K. L. Wong, P. Kung, A. Saxler and M. Razeghi; *Phase-matched optical second-harmonic generation in GaN and AlN slab waveguides*; Journal of Applied Physics **85** (5); 2497-2501 (1999).

140   W. P. Risk, T. R. Gosnell and A. V. Nurmikko; *Compact Blue-Green Lasers*. (Cambridge University Press, New York, 2003).

141   Y. R. Shen; *The principles of nonlinear optics*. (Wiley-Interscience, Hoboken, N.J, 2003).

142   J. L. P. Hughes, Y. Wang and J. E. Sipe; *Calculation of linear and second-order optical response in wurtzite GaN and AlN*; Physical Review B **55** (20); 13630-13640 (1997).

143   N. A. Sanford, A. V. Davydov, D. V. Tsvetkov, A. V. Dmitriev, S. Keller, U. K. Mishra, S. P. DenBaars, S. S. Park, J. Y. Han and R. J. Molnar; *Measurement of second order susceptibilities of GaN and AlGaN*; Journal of Applied Physics **97** (5); 053512 (2005).

144   H. Y. Zhang, X. H. He, Y. H. Shih, M. Schurman, Z. C. Feng and R. A. Stall; *Study of nonlinear optical effects in GaN:Mg epitaxial film*; Applied Physics Letters **69** (20); 2953-2955 (1996).

145   Y. Fujii, S. Yoshida, S. Misawa, S. Maekawa and T. Sakudo; *Nonlinear Optical Susceptibilities of AlN Film*; Applied Physics Letters **31** (12); 815-816 (1977).

146   G. Yu, G. Wang, H. Ishikawa, M. Umeno, T. Soga, T. Egawa, J. Watanabe and T. Jimbo; *Optical properties of wurtzite structure GaN on sapphire around fundamental absorption edge (0.78 - 4.77eV) by spectroscopic ellipsometry and the optical transmission method*; Applied Physics Letters **70** (24); 3209-3211 (1997).

147   S. V. Rao, K. Moutzouris and M. Ebrahimzadeh; *Nonlinear frequency conversion in semiconductor optical waveguides using birefringent, modal and quasi-phase-matching techniques*; Journal of Optics a-Pure and Applied Optics **6** (6); 569-584 (2004).

148   S. Somekh and A. Yariv; *Phase matching by periodic modulation of the nonlinear optical properties*; Optics Communications **6** (3); 301-304 (1972).

149   S. Somekh and A. Yariv; *Phase-Matchable Nonlinear Optical Interactions in Periodic Thin-Films*; Applied Physics Letters **21** (4); 140-141 (1972).

150   M. M. Fejer, G. A. Magel, D. H. Jundt and R. L. Byer; *Quasi-Phase-Matched 2nd Harmonic-Generation - Tuning and Tolerances*; IEEE Journal of Quantum Electronics **28** (11); 2631-2654 (1992).

151   S. J. B. Yoo, R. Bhat, C. Caneau and M. A. Koza; *Quasi-Phase-Matched 2nd-Harmonic Generation in Algaas Wave-Guides with Periodic Domain Inversion Achieved by Wafer-Bonding*; Applied Physics Letters **66** (25); 3410-3412 (1995).

152   R. Haidar, P. Kupecek and E. Rosencher; *Nonresonant quasi-phase matching in GaAs plates by Fresnel birefringence*; Applied Physics Letters **83** (8); 1506-1508 (2003).

153   A. S. Helmy, D. C. Hutchings, T. C. Kleckner, J. H. Marsh, A. C. Bryce, J. M. Arnold, C. R. Stanley, J. S. Aitchison, C. T. A. Brown, K. Moutzouris and M. Ebrahimzadeh; *Quasi phase matching in GaAs-AlAs superlattice waveguides through bandgap tuning by use of quantum-well intermixing*; Optics Letters **25** (18); 1370-1372 (2000).

154   S. H. Lee, T. Minegishi, J. S. Park, S. H. Park, J. S. Ha, H. J. Lee, H. J. Lee, S. Ahn, J. Kim, H. Jeon and T. Yao; *Ordered arrays of ZnO nanorods grown on periodically polarity-inverted surfaces*; Nano Letters **8** (8); 2419-2422 (2008).

155   H. Morkoc, S. Strite, G. B. Gao, M. E. Lin, B. Sverdlov and M. Burns; *Large-Band-Gap SiC, III-V Nitride, and II-VI ZnSe-Based Semiconductor-Device Technologies*; Journal of Applied Physics **76** (3); 1363-1398 (1994).

156   A. Yariv; *Optical Electronics in Modern Communications*; 5th ed. (Oxford University Press., New York, 2003).

157   R. W. Boyd; *Nonlinear Optics*; 2th ed. (Academic Press., San Diego, 2003).

158   G. New; *Introduction to Nonlinear Optics*; 1th ed. (Cambridge University Press New York, 2011).

159   L. E. Myers, R. C. Eckardt, M. M. Fejer, R. L. Byer, W. R. Bosenberg and J. W. Pierce; *Quasi-Phase-Matched Optical Parametric Oscillators in Bulk Periodically Poled Linbo3*; Journal of the Optical Society of America B-Optical Physics **12** (11); 2102-2116 (1995).

160   U. Ozgur, G. Webb-Wood, H. O. Everitt, F. Yun and H. Morkoc; *Systematic measurement of AlxGa1-xN refractive indices*; Applied Physics Letters **79** (25); 4103-4105 (2001).

161   G. M. Laws, E. C. Larkins, I. Harrison, C. Molloy and D. Somerford; *Improved refractive index formulas for the AlxGa1-xN and InyGa1-yN alloys*; Journal of Applied Physics **89** (2); 1108-1115 (2001).

162   U. Tisch, B. Meyler, O. Katz, E. Finkman and J. Salzman; *Dependence of the refractive index of AlxGa1-xN on temperature and composition at elevated temperatures*; Journal of Applied Physics **89** (5); 2676-2685 (2001).

163   N. A. Sanford, L. H. Robins, A. V. Davydov, A. Shapiro, D. V. Tsvetkov, A. V. Dmitriev, S. Keller, U. K. Mishra and S. P. DenBaars; *Refractive index study of AlxGa1-xN films grown on sapphire substrates*; Journal of Applied Physics **94** (5); 2980-2991 (2003).

164   M. Rigler, M. Zgonik, M. P. Hoffmann, R. Kirste, M. Bobea, R. Collazo, Z. Sitar, S. Mita and M. Gerhold; *Refractive index of III-metal-polar and N-polar AlGaN waveguides grown by metal organic chemical vapor deposition*; Applied Physics Letters **102** (22); 221106-221105 (2013).

165   S. Helmfrid and G. Arvidsson; *Influence of Randomly Varying Domain Lengths and Nonuniform Effective Index on 2nd-Harmonic Generation in Quasi-Phase-Matching Wave-Guides*; Journal of the Optical Society of America B-Optical Physics **8** (4); 797-804 (1991).

166   H. P. Wagner; *Second Harmonic Generation in Thin Film II–VI Optical Waveguides*; physica status solidi (b) **187** (2); 363-369 (1995).

167   R. Collazo, S. Mita, A. Rice, R. F. Dalmau and Z. Sitar; *Simultaneous growth of a GaN p/n lateral polarity junction by polar selective doping*; Applied Physics Letters **91** (21); 212103 (2007).

168   M. Stutzmann, O. Ambacher, M. Eickhoff, U. Karrer, A. Lima Pimenta, R. Neuberger, J. Schalwig, R. Dimitrov, P. Schuck and R. Grober; *Playing with Polarity*; physica status solidi (b) **228** (2); 505-512 (2001).

169   H. Kim, J.-H. Ryou, R. D. Dupuis, S.-N. Lee, Y. Park, J.-W. Jeon and T.-Y. Seong; *Electrical characteristics of contacts to thin film N-polar n-type GaN*; Applied Physics Letters **93** (19); 192106-192103 (2008).

170   M. P. Hoffmann, M. Gerhold, R. Kirste, A. Rice, C.-R. Akouala, J. Q. Xie, S. Mita, R. Collazo and Z. Sitar; *Fabrication and characterization of lateral polar GaN structures for second harmonic generation*; Proceedings of SPIE **8631**; 86311T (2013).

171   S. F. Li, S. Fuendling, X. Wang, S. Merzsch, M. A. M. Al-Suleiman, J. D. Wei, H. H. Wehmann, A. Waag, W. Bergbauer and M. Strassburg; *Polarity and Its Influence on Growth Mechanism during MOVPE Growth of GaN Sub-micrometer Rods*; Crystal Growth & Design **11** (5); 1573-1577 (2011).

172   S. F. Li, X. Wang, M. S. Mohajerani, S. Fundling, M. Erenburg, J. D. Wei, H. H. Wehmann, A. Waag, M. Mandl, W. Bergbauer and M. Strassburg; *Dependence of N-polar GaN rod morphology on growth parameters during selective area growth by MOVPE*; Journal of Crystal Growth **364**; 149-154 (2013).

173   S. J. Zhou and S. Liu; *Study on sapphire removal for thin-film LEDs fabrication using CMP and dry etching*; Applied Surface Science **255** (23); 9469-9473 (2009).

174   F. Cuccureddu, S. Murphy, I. V. Shvets, M. Porcu, H. W. Zandbergen, N. S. Sidorov and S. I. Bozhko; *Surface morphology of c-plane sapphire (alpha-alumina) produced by high temperature anneal*; Surface Science **604** (15-16); 1294-1299 (2010).

175   P. R. Ribic and G. Bratina; *Behavior of the (0001) surface of sapphire upon high-temperature annealing*; Surface Science **601** (1); 44-49 (2007).

176   Y. Kumagai, T. Igi, M. Ishizuki, R. Togashi, H. Murakami, K. Takada and A. Koukitu; *Formation of AlN on sapphire surfaces by high-temperature heating in a mixed flow of H-2 and N-2*; Journal of Crystal Growth **350** (1); 60-65 (2012).

177   A. Rice, R. Collazo, J. Tweedie, R. Dalmau, S. Mita, J. Xie and Z. Sitar; *Surface preparation and homoepitaxial deposition of AlN on (0001)-oriented AlN substrates by metalorganic chemical vapor deposition*; Journal of Applied Physics **108** (4) (2010).

178   R. Kirste, R. Collazo, G. Callsen, M. R. Wagner, T. Kure, J. S. Reparaz, S. Mita, J. Xie, A. Rice, J. Tweedie, Z. Sitar and A. Hoffmann; *Temperature dependent photoluminescence of lateral polarity junctions of metal organic chemical vapor deposition grown GaN*; Journal of Applied Physics **110** (9); 093503-093509 (2011).

179   A. Koukitu and Y. Kumagai; *Thermodynamic analysis of group III nitrides grown by metal-organic vapour-phase epitaxy (MOVPE), hydride (or halide) vapour-phase epitaxy (HVPE) and molecular beam epitaxy (MBE)*; Journal of Physics-Condensed Matter **13** (32); 6907-6934 (2001).

180   R. Collazo, S. Mita, A. Aleksov, R. Schlesser and Z. Sitar; *Growth of Ga- and N-polar gallium nitride layers by metalorganic vapor phase epitaxy on sapphire wafers*; Journal of Crystal Growth **287** (2); 586-590 (2006).

181   S. Nitta, M. Kariya, T. Kashima, S. Yamaguchi, H. Amano and I. Akasaki; *Mass transport and the reduction of threading dislocation in GaN*; Applied Surface Science **159–160** (0); 421-426 (2000).

182   Y. Wu, A. Hanlon, J. F. Kaeding, R. Sharma, P. T. Fini, S. Nakamura and J. S. Speck; *Effect of nitridation on polarity, microstructure, and morphology of AlN films*; Applied Physics Letters **84** (6); 912-914 (2004).

183   D. Zhuang and J. H. Edgar; *Wet etching of GaN, AlN, and SiC: a review*; Materials Science and Engineering: R: Reports **48** (1); 1-46 (2005).

184   J. Li, Z. Y. Fan, R. Dahal, M. L. Nakarmi, J. Y. Lin and H. X. Jiang; *200 nm deep ultraviolet photodetectors based on AlN*; Applied Physics Letters **89** (21); 213510 (2006).

185   M. Kneissl, Z. H. Yang, M. Teepe, C. Knollenberg, O. Schmidt, P. Kiesel, N. M. Johnson, S. Schujman and L. J. Schowalter; *Ultraviolet semiconductor laser diodes on bulk AlN*; Journal of Applied Physics **101** (12); 123103 (2007).

186   R. Collazo, S. Mita, J. Q. Xie, A. Rice, J. Tweedie, R. Dalmau, B. Moody, R. Schlesser, R. Kirste, A. Hoffmann and Z. Sitar; *265 nm Light Emitting Diodes on AlN Single Crystal Substrates: Growth and Characterization*; 2011 Conference on Lasers and Electro-Optics (Cleo) (2011).

187   S. Rajan, A. Chini, M. H. Wong, J. S. Speck and U. K. Mishra; *N-polar GaN/AlGaN/GaN high electron mobility transistors*; Journal of Applied Physics **102** (4) (2007).

188   J. Bai, M. Dudley, W. H. Sun, H. M. Wang and M. A. Khan; *Reduction of threading dislocation densities in AlN/sapphire epilayers driven by growth mode modification*; Applied Physics Letters **88** (5); 051903-051903 (2006).

189   M. Takeuchi, H. Shimizu, R. Kajitani, K. Kawasaki, T. Kinoshita, K. Takada, H. Murakami, Y. Kumagai, A. Koukitu, T. Koyama, S. F. Chichibu and Y. Aoyagi; *Al- and N-polar AlN layers grown on c-plane sapphire substrates by modified flow-modulation MOCVD*; Journal of Crystal Growth **305** (2); 360-365 (2007).

190   J. Jasinski, Z. Liliental-Weber, Q. S. Paduano and D. W. Weyburne; *Inversion domains in AlN grown on (0001) sapphire*; Applied Physics Letters **83** (14); 2811-2813 (2003).

191   L. T. Romano, J. E. Northrup and M. A. O'Keefe; *Inversion domains in GaN grown on sapphire*; Applied Physics Letters **69** (16); 2394-2396 (1996).

192   Y. Kumagai, J. Tajima, M. Ishizuki, T. Nagashima, H. Murakami, K. Takada and A. Koukitu; *Self-separation of a thick AlN layer from a sapphire substrate via interfacial voids formed by the decomposition of sapphire*; Applied Physics Express **1** (4) (2008).

193   S. Dasgupta, F. Wu, J. S. Speck and U. K. Mishra; *Growth of high quality N-polar AlN(0001) on Si(111) by plasma assisted molecular beam epitaxy*; Applied Physics Letters **94** (15); 151906-151903 (2009).

194   M. Takeuchi, H. Shimizu, R. Kajitani, K. Kawasaki, Y. Kumagai, A. Koukitu and Y. Aoyagi; *Improvement of crystalline quality of N-polar AlN layers on c-plane sapphire by low-pressure flow-modulated MOCVD*; Journal of Crystal Growth **298**; 336-340 (2007).

195   A. Sedhain, N. Nepal, M. L. Nakarmi, T. M. A. tahtamouni, J. Y. Lin, H. X. Jiang, Z. Gu and J. H. Edgar; *Photoluminescence properties of AlN homoepilayers with different orientations*; Applied Physics Letters **93** (4); 041905-041903 (2008).

196   R. Collazo, J. Xie, B. E. Gaddy, Z. Bryan, R. Kirste, M. Hoffmann, R. Dalmau, B. Moody, Y. Kumagai, T. Nagashima, Y. Kubota, T. Kinoshita, A. Koukitu, D. L. Irving and Z. Sitar; *On the origin of the 265 nm absorption band in AlN bulk crystals*; Applied Physics Letters **100** (19); 191914-191915 (2012).

197   R. Kirste, M. R. Wagner, J. H. Schulze, A. Strittmatter, R. Collazo, Z. Sitar, M. Alevli, N. Dietz and A. Hoffmann; *Optical properties of InN grown on templates with controlled surface polarities*; physica status solidi (a) **207** (10); 2351-2354 (2010).

198   K. B. Nam, J. Li, M. L. Nakarmi, J. Y. Lin and H. X. Jiang; *Deep ultraviolet picosecond time-resolved photoluminescence studies of AlN epilayers*; Applied Physics Letters **82** (11); 1694-1696 (2003).

199   M. Feneberg, B. Neuschl, K. Thonke, R. Collazo, A. Rice, Z. Sitar, R. Dalmau, J. Xie, S. Mita and R. Goldhahn; *Sharp bound and free exciton lines from homoepitaxial AlN*; physica status solidi (a) **208** (7); 1520-1522 (2011).

200   J. Li, K. B. Nam, M. L. Nakarmi, J. Y. Lin, H. X. Jiang, P. Carrier and S.-H. Wei; *Band structure and fundamental optical transitions in wurtzite AlN*; Applied Physics Letters **83** (25); 5163-5165 (2003).

201   B. N. Pantha, N. Nepal, T. M. A. Tahtamouni, M. L. Nakarmi, J. Li, J. Y. Lin and H. X. Jiang; *Correlation between biaxial stress and free exciton transition in AlN epilayers*; Applied Physics Letters **91** (12); 121117-121113 (2007).

202   P. J. Schuck, M. D. Mason, R. D. Grober, O. Ambacher, A. P. Lima, C. Miskys, R. Dimitrov and M. Stutzmann; *Spatially resolved photoluminescence of inversion domain boundaries in GaN-based lateral polarity heterostructures*; Applied Physics Letters **79** (7); 952-954 (2001).

203   M. K. Kelly, O. Ambacher, B. Dahlheimer, G. Groos, R. Dimitrov, H. Angerer and M. Stutzmann; *Optical patterning of GaN films*; Applied Physics Letters **69** (12); 1749-1751 (1996).

204   A. Aleksov, R. Collazo, S. Mita, R. Schlesser and Z. Sitar; *Current-voltage characteristics of n/n lateral polarity junctions in GaN*; Applied Physics Letters **89** (5); 052117 (2006).

Acknowledgements

I would like to thank everybody who supported and guided me before and while I was writing this dissertation and all who brought me here including my family and friends. Some people I owe special gratitude:

- I would like to sincerely thank my research advisor Prof. Zlatko Sitar for his guidance and his infinite support, and the opportunity to conduct my research at NC State. I developed myself a lot professionally and personally in his group. It was an impressive and interesting time for me.
- I am also very grateful to my thesis advisor Prof. Michael Kneissl for offering valuable advice and giving me the chance to graduate in his group. I would also like to thank him for the assistance with the Post-Doctoral fellowship application.
- I would like to sincerely thank Prof. Ramón Collazo for his assistance, guidance, patience, and for his open-door for a discussion at any time. It was always a pleasure and fun to work with him.
- I am also grateful to my committee member Prof. Michael Lehmann for chairing my defense.
- Special thanks also to Dr. Mike Gerhold from ARO for his assistance and trust, as well for the chance of doing a Post.-Doc. with him.
- I am also very grateful to Dr. Ronny Kirste for his support, collaboration and friendship, which made this dissertation possible.
- Special thanks also to Seiji Mita for the guidance at the MOCVD system in the beginning, Anthony Rice for all the discussions, to Joseph Rajan for his help in the LPS work, Zachary Bryan for the help at PL measurements, Isaac Bryan for his help with AFM measurements, Wei Guo for the help at the LPS template fabrication, James Tweedie for his collaboration on the point defect management work, and Jinqiao Xie for his collaboration and help in everything.
- Special thanks also to the entire WideBandgaps Group at NCSU who supported me in so many ways, and to all my collaborators, like Gordon Callsen, Christian Nenstiel, and all the people I worked with at TU-Berlin.

Special gratitude to my family and to my girlfriend Katharina.

To my father and my mother, this dissertation is dedicated to you.